UNIVERSITÀ DEGLI STUDI DI NAPOLI FEDERICO II

PH.D. THESIS

IN

INFORMATION TECHNOLOGY AND ELECTRICAL ENGINEERING

Advanced Diagnosis Techniques for Radio Telescopes in Astronomical Applications

SALVATORE SAVARESE

TUTORS: AMEDEO CAPOZZOLI
ANGELO LISENO
CLAUDIO CURCIO

COORDINATOR: DANIELE RICCIO

XXX CICLO

SCUOLA POLITECNICA E DELLE SCIENZE DI BASE

DIPARTIMENTO DI INGEGNERIA ELETTRICA E TECNOLOGIE DELL'INFORMAZIONE

Contents

List of Acronyms 7

1 Overview on Radio Telescopes **6**

1.1 The role of Radio astronomy 6

1.2 Antennas Parameters 8

1.2.1 Effective Area and Radio Brightness 8

1.2.2 Radiation Pattern 10

1.2.3 Antenna Gain 11

1.2.4 Antenna Temperature and Noise Temperature . . . 13

1.2.5 Antenna Efficiency 15

1.3 Radio telescope systems 16

1.3.1 Single reflector antennas 16

1.3.2 Dual reflector systems 21

1.3.3 Beamforming Arrays 24

1.3.4 Interferometers 26
1.4 Influence of Imperfections on Performance 35
1.4.1 Small scale surface errors 36
1.4.2 Large scale deformations 38
1.4.3 Effects of misalignments 42

2 Radio Telescope Diagnosis Methods **50**
2.1 Direct Methods for Reflector Diagnosis 52
2.1.1 Theodolite and Tape 52
2.1.2 Photogrammetry 53
2.2 Antenna Radiation Analysis 53
2.2.1 Aperture Field Method 53
2.2.2 Induced Currents Method 57
2.3 Coherent Microwave Holography 58
2.3.1 Paraboloid Surface Best Fitting 64
2.3.2 Reflector Shape Retrieval 67

3 Optimized approach to the reflector diagnosis **70**
3.1 Introduction 71
3.2 Selection of basis functions for the Aperture Field expansion 76
3.2.1 Karhunen–Loève theorem 76
3.2.2 Principal Component Analysis of the Aperture Field 78
3.3 Optimized sampling distribution 81

4 Fast Marching Method **85**

4.1 Geometrical Optics fundamental Equations 87

4.1.1 Transport Equations 89

4.2 Solution to the eikonal equation 90

4.2.1 Numerical discretization 91

4.2.2 The Fast Marching Method algorithm 93

4.2.3 Discretization of Σ for the initialization of the Fast Marching Method (FMM) 96

4.2.4 Parallel Fast Marching Algorithms 101

4.3 Implementation of the Fast Marching Method 106

4.3.1 Parallel Fast Iterative Method for GPU 106

4.3.2 Inverse Ray Tracing 111

4.3.3 Managing multiple interactions 113

5 Numerical and Experimental Results **118**

5.1 Numerical test cases for the Fast Marching Method 119

5.1.1 Benchmark Results 120

5.1.2 Scattering from a conducting sphere 121

5.1.3 Scattering from a coated sphere 126

5.1.4 Simulation of a Luneburg lens 129

5.1.5 Evaluation of the Aperture Field phase of a parabolic reflector 133

5.2 Optimized Diagnosis of a Reflector Antenna 139

5.2.1 Measurement Setup 139
5.2.2 Operating Conditions 146
5.2.3 Numerical Results 148
5.2.4 Experimental Results 158

List of Acronyms

The following acronyms are used throughout this text.

AF Aperture Field

AFM Aperture Field Method

AP Aperture Plane

ASKAP Australian SKA Pathfinder

AUT Antenna Under Test

AWGN Additive White Gaussian Noise

CUDA Compute Unified Device Architecture

FEA Finite Element Analysis

FF Far-Field

FFP Far-field Pattern

FFT Fast Fourier Transform

FIM Fast Iterative Method

FMM Fast Marching Method

FSM Fast Sweeping Method

G-PSWF generalized Prolate Spheroidal Wave Function

GO Geometrical Optics

GPU Graphics Processing Unit

HPBW Half Power Beam Width

LOFAR LOw-Frequency ARray

LWA1 Long Wavelength Array Station 1

MoM Method of Moments

NB Narrow Band

NF Near-Field

NFFF Near-Field Far-Field

PAF Phased Array Feed

PCA Principal Component Analysis

PDE Partial Differential Equation

PO Physical Optics

R-PSWF rectangular Prolate Spheroidal Wave Function

PSWF Prolate Spheroidal Wave Function

PWS Plane Wave Spectrum

RMS Root Mean Square

SBR Shooting and Bouncing Rays

SIMD Single Instruction Multiple Data

SKA Square Kilometer Array

SNR Signal to Noise Ratio

SVD Singular Value Decomposition

SVO Singular Value Optimization

TSVD Truncated Singular Value Decomposition

VLA Very Large Array

VLBA Very Long Baseline Array

VLBI Very Long Baseline Interferometry

VNA Vector Network Analyzer

Introduction

The performance of radio telescopes in astronomical applications can be affected by structural variations due to:

- Misalignment of the feeding structure, resulting in a lateral or axial displacement of the receiver;
- Wind stress;
- Gravitational distortion as the antenna is tilted;
- Thermal distortion with ambient temperature or sunlight.

Diagnosis methods are necessary to estimate any deviation of the antenna system from its nominal behavior in order to guarantee the maximum performance. Several approaches have been developed during the years, and among them the electromagnetic diagnosis appears today as the most appealing, because it allows a relatively simple measurement setup and

a reduced human intervention. Electromagnetic diagnosis is based on the acquisition of the antenna Far Field Pattern (FFP), with the Antenna Under Test (AUT) working in receiving mode. A natural radio star or a satellite beacon provides the signal source. The acquisition of the FFP typically requires a very large number of field samples to get the complete information about the AUT, and the subsequent measurement process may span over several hours. A prolonged acquisition has significant drawbacks related to the continuous tracking of the source and the inconstancy of the environmental conditions. The purpose of the PhD activity has been focused on an optimized formulation of the diagnosis of radio telescopes aimed at reducing the number of field samples to acquire, and so at minimizing the measurement time. A diagnosis approach has been developed, based on the Aperture Field method for the description of the AUT radiation mechanism. A Principal Component Analysis (PCA) has been employed to restore a linear relationship between the unknowns describing the AUT status and the far field data. An optimal far field sampling grid is selected by optimizing the singular values behavior of the relevant linearized operator. During the activity, a computational tool based on Geometrical Optics (GO) has been developed to improve the diagnosis approach. Indeed, once the Aperture Field is recovered from the inversion of the measured FFP, an additional step is required to assess the AUT status from the phase distribution. Obviously, the computation of the phase distribution should be based on efficient algorithms in order to properly manage electrically

large reflectors. The developed GO technique relies on the Fast Marching Method (FMM) for the direct solution of the eikonal equation. A GO approach based on the FMM is appealing because it shows a favorable computational trend. Furthermore, the explicit solution of the eikonal equation opens the possibility to set up an inverse ray tracing scheme, which proves particularly convenient compared to direct ray tracing because it allows to easily select the minimum number of rays to be traced. The FMM is also amenable for parallel execution. In particular, in the present work, the Fast Iterative Method has been implemented on Graphics Processing Units (GPUs). Moreover, the FMM has been accelerated by introducing a tree data structure. The tree allows to manage the mutual interactions between multiple scattering surfaces and the parallelization of the ray tracing step. The method has been numerically tested on simple canonical cases to show its performance in terms of accuracy and speed. Then, it has been applied to the evaluation of the Aperture Field phase required by the reflector diagnosis. During the research activity, the problem of validating the diagnosis algorithms has been also faced. Obviously, a numerical analysis can been carried out to test the model employed to describe the system and to evaluate the performance of the algorithm. To this end, a reliable commercial software exploited to simulate reflector antennas has been exploited. However, to complete the analysis, the experimental validation becomes mandatory, and an experimental outdoor far field test range is required. Accordingly, a test range has been set up thanks to the

collaboration with Istituto Nazionale di Astrofisica (INAF) of Naples, Italy, under the supervision of Dr. Pietro Schipani. Its realization has involved the full development of the software to drive an Alt-Azimuth positioner and to remotely control the instrumentation. In addition, an upgrade of the internal connections of a Vector Network Analyzer has been performed in order to allow the interferometric acquisition.

The Thesis is organized as follows.

The First Chapter focuses on an overview on the general features of radio telescope systems and on the factors affecting their performance.

The Second Chapter presents an overview on already available electromagnetic diagnosis approaches. In particular, microwave holography is described, which is based on the acquisition of a complete set of Far Field Pattern (FFP) data, wherein the acquisition of both amplitude and phase is made possible thanks to the use of a second antenna employed as reference. Alternative approaches are possible, requiring the measurement of the amplitude only of the FFP, simplifying the measurement set up.

The Third Chapter is dedicated to the proposed optimized diagnosis method. In particular, it introduces the model to link the FFP to the parameters describing the status of the AUT, the representation obtained thanks to the PCA, and the selection of the optimal sampling grid.

The Fourth Chapter deals with the description of the GO tool for the direct numerical solution of the eikonal equation. In particular, the properties and the implementation of the FMM algorithm are presented. The Fast

Iterative Method, a parallel version of the FMM amenable of parallel execution on GPUs, is also introduced.

The Fifth Chapter shows the results of numerical tests to evaluate the performance of the approach. Furthermore, it presents the measurement setup realized at the Observatory of Capodimonte in Naples and the tests therein performed.

Chapter 1

Overview on Radio Telescopes

1.1 The role of Radio astronomy

The vast majority of our knowledge about distant souce, that is, the spatial distribution, kinematics and composition of stars and interstellar medium, has been obtained from electromagnetic radiation. Only a very small part stems from material carriers, such as meteorites that impact the Earth or samples of material collected by manned or unmanned space probes. The first astronomical measurements were restricted to visible light, and later slightly expanded into the near infrared. In 1930, they ranged from the near ultraviolet to the near infrared: $0.35\,\mu\text{m} \leq \lambda \leq 1\,\mu\text{m}$. At other wavelengths, investigations were limited either by the terrestrial atmosphere absorption or because no detectors were available. In 1931, this situation changed when Jansky showed that radiation at a wavelength of

14.6 m received with a direction-sensitive antenna array followed sidereal time instead of solar time, implying that it was emitted by an extraterrestrial source different from the sun[1]. After the end of World War II, radio physics had made great progress thanks to the development of sensitive radar equipment and some researchers could turn their attention towards the radio "noise" from extraterrestrial sources. The technological development toward higher sensitivity receivers and higher angular resolution telescopes allowed the radio astronomy window to be extended from $\lambda \simeq 30\,\mathrm{m}$ to $\lambda \leq 0.2\,\mathrm{m}$. While radiation in optical wavelengths usually stems from the celestial object temperature, the radiation studied in radio astronomy has a non thermal origin but requires emission mechanisms that differ considerably from those studied previously. For instance, much of modern radio astronomy is devoted to the study of neutral hydrogen, the most common substance in the universe, detectable as a narrow spectral line at about 1.420 MHz ($\lambda \simeq 21\,\mathrm{cm}$). As mentioned, the wavelengths feasible for radio astronomy are limited by the atmosphere, which is transparent to radio waves in the range from about $\lambda \simeq 0.2\,\mathrm{mm}$ to $\lambda \simeq 30\,\mathrm{m}$, commonly referred to as the ground based radio window (Fig. 1.1). There is a great interest to extend the upper frequency limits of the measurements as higher as possible, since astronomical sources produce more intense signals in this range. The high frequency cut-off is due to the absorption from molecules in the troposphere, mainly water vapor (H_2O) and oxygen (O_2). Since water is one of the determining factors, it is possible to extend the accessible

frequency range by carrying out observations from high altitude locations with dry climates. At the lowest frequencies, the terrestrial atmosphere ceases to be transparent because of free electrons in the ionosphere. The low frequency limit of the radio window will be near 4.5 MHz at night and near 11 MHz at daytime. Radio astronomy below this range must be performed from satellites above Earth's ionosphere. Since the signals of interest in radio astronomy are typically extremely weak, high sensitivity instruments are needed, resulting in some of the most advanced antenna systems available. The progress in the development of radio telescopes was driven towards the construction of ever larger antennas and the arrangement of different antennas in arrays and interferometers able to further increase the angular resolution. This chapter introduces the basic notions to describe these antenna systems and provides a brief overview of the main features of modern radio telescopes.

1.2 Antennas Parameters

1.2.1 Effective Area and Radio Brightness

A radio telescope may consist of a single antenna of an array of antennas connected together to form a single system. The power p per unit frequency available at the antenna output will be proportional to the energy flux per unit frequency impinging the antenna, referred to as the flux density S $\left[\mathrm{W\,m^{-2}\,Hz^{-1}}\right]$ of the source being observed, and can be expressed as:

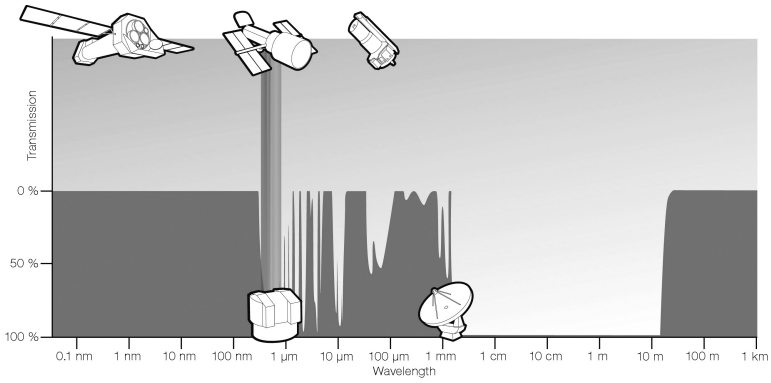

Figure 1.1. The transmissivity of the Earth's atmosphere as function of wavelength. Good transmission is only possible around 1 µm wavelength (visible and infrared) and in the radio window.

$$p = A_{\text{eff}} S \tag{1.1}$$

where the proportionality constant A_{eff} is the *effective area* of the radio telescope. It has the dimension of an area and expresses how effective the telescope is at absorbing the radiation at a specific frequency and from a specific direction. The signals received from cosmic sources on the celestial sphere may be considered as spatially incoherent wideband random noise. Some radiation phenomena may show a specific polarization and spectral absorption or emission lines. Given the nature of the radio astronomical signals, astronomers are interested in recovering the brightness of the source, rather than the emitted electric field. The radio brightness can be defined as the emitted flux density per unit solid angle as a function of

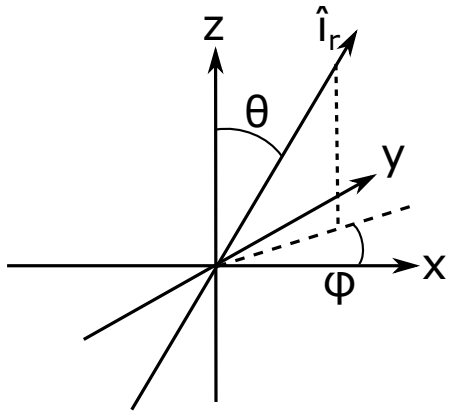

Figure 1.2. Spherical reference system.

the observing direction:

$$B(\theta, \phi) = \frac{S}{\Omega} \tag{1.2}$$

where Ω is the solid angle, and (θ, ϕ) are the coordinates of a spherical reference system (Fig. 1.2).

1.2.2 Radiation Pattern

The radiation pattern, or Far-field Pattern (FFP), represents the directional dependence of the field radiated by a transmitting antenna or the angular response of a receiving antenna to a far away source. The FFP is analogous to the point spread function used to describe optical systems. A typical FFP is shown in Fig. 1.3. Various parts of the FFP are referred to as lobes or beams. The lobe corresponding to the maximum response

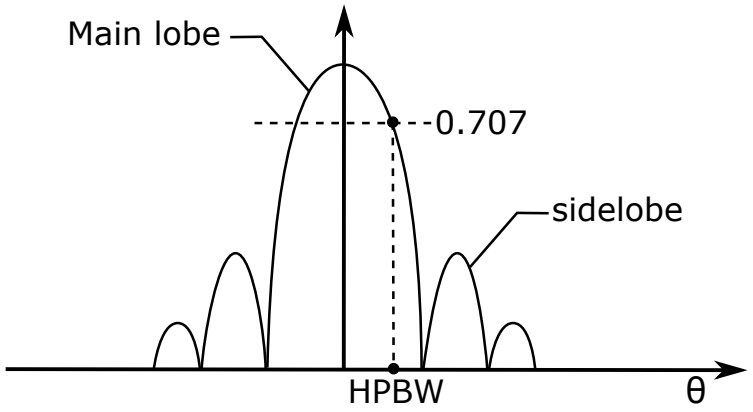

Figure 1.3. Sketch of a generic antenna FFP.

is the main lobe. The ratio between the main lobe and the first sidelobe is the sidelobe level. The sidelobes contribute to the radiation picked up from sources outside the primary direction of observation. The FFP is usually normalized with respect to its maximum and expressed in either polar or Cartesian coordinates. An important parameter in describing the directivity of the antenna is the Half Power Beam Width (HPBW), which is the angle where the level of the pattern declines to a level equal to 0.707 times that of the maximum. When the FFP is expressed in decibel, the HPBW corresponds to the level equal to $-3\,\mathrm{dB}$ below the main lobe maximum.

1.2.3 Antenna Gain

The antenna gain is defined as the ratio of the radiation intensity in a given direction in the far field to the total intensity that would be produced

by an isotropic lossless antenna. This ideal isotropic antenna transmits or receives radiation in all directions equally, whereas a high gain antenna will preferentially radiate or receive in a particular direction. If we define the effective collecting area of an antenna in one direction as $A_{\text{eff}}(\theta, \phi)$, then the power received when the antenna is pointed in the direction (θ_0, ϕ_0) from a source with intensity $I(\theta, \phi)$ is:

$$p(\theta_0, \phi_0) = \int A_{\text{eff}}(\theta - \theta_0, \phi - \phi_0) I(\theta, \phi) \, \mathrm{d}\Omega \tag{1.3}$$

The beam solid angle of the antenna is defined as:

$$\Omega_{A_{\text{eff}}} = \iint P(\theta, \phi) \, \mathrm{d}\Omega \tag{1.4}$$

where $P(\theta, \phi)$ is the normalized power pattern defined as $P(\theta, \phi) = A_{\text{eff}}(\theta, \phi)/A_{\text{eff0}}$, A_{eff0} being the maximum response of the antenna. The beam solid angle represents the angle through which all the power would flow if the power per unit solid angle were constant and equal to the maximum value. For a uniform pattern equal to unity in every direction, the beam solid angle is the maximum possible and equal to 4π. Therefore, the antenna directive gain is also approximated as[2]:

$$G = \frac{4\pi}{\Omega_A} \tag{1.5}$$

An important relationship in antenna theory is that the product of

the effective area and beam solid angle is equal to λ^2[3]. In other words, the gain of the antenna is inversely proportional to the field of view for a given wavelength. Thus, an isotropic antenna would sense the whole sky with equally, but with a very small effective collecting area. As the collecting area increases, the field of view decreases. This relationship plays an important role in the design of modern aperture synthesis telescopes. Thanks to the quadratic relationship with λ, even wire antennas show enough gain for wavelengths longer than 1 m. Indeed, wire antennas are common in astronomy and they include dipoles, Yagis, spirals and helices. The effective collecting area can be enhanced by arranging the antennas in arrays. For shorter wavelengths, reflector antennas are more common.

1.2.4 Antenna Temperature and Noise Temperature

The power received by an antenna from an unpolarized radio source located in the direction (θ_0, ϕ_0) can be expressed as:

$$P_r = \frac{1}{2} \iint A_{\text{eff}}(\theta - \theta_0, \phi - \phi_0) B(\theta, \phi) \, \mathrm{d}\theta \mathrm{d}\phi \tag{1.6}$$

where the factor 1/2 takes into account the assumption that the antenna receives a single polarization component. The power received can be equated to the thermal noise power available from a fictitious resistor at a temperature T_a, with the resistor replacing the antenna at the input of the receiver:

$$T_a = \frac{1}{2k} \iint A_{\text{eff}}(\theta - \theta_0, \phi - \phi_0) B(\theta, \phi)\, \mathrm{d}\theta \mathrm{d}\phi = \frac{P_r}{k} \tag{1.7}$$

where $k = 1.38 \times 10^{-23} \mathrm{W\,Hz^{-1}\,K^{-1}}$ is the Boltzmann constant. T_a is known as the *antenna temperature* and is an alternative expression of the power received, not the actual temperature of the antenna. In an analogous way, the brightness of a radio source can be expressed in terms of the temperature of an equivalent black-body, even when the emission is not related to thermal radiation. The equivalent temperature is the brightness temperature of the source T_B, and is related to the radio brightness by the Rayleigh-Jeans law. The relationship can be approximated as:

$$B \approx \frac{2kT_B}{\lambda^2} \tag{1.8}$$

which is valid for $hf \ll kT_B$, h being the Planck constant. Using the brightness temperature to express the signal received from the source, Eq. (1.7) becomes:

$$T_a = \frac{1}{\lambda^2} \iint A_{\text{eff}}(\theta - \theta_0, \phi - \phi_0) T_B(\theta, \phi)\, \mathrm{d}\theta\phi \tag{1.9}$$

Since signals received by radio telescopes are extremely weak and "noise-like", e.g. white noise, containing all frequencies in the band, it can be convenient to consider an equivalent noise temperature corresponding to the received power level. The total output power P_{tot} received by an antenna

includes two components, that is, the antenna temperature (the signal), and the added noise of the system, referred to as the system temperature T_{sys}:

$$P_{tot} = P_a + P_{sys} \Rightarrow T_{tot} = T_a + T_{sys} \tag{1.10}$$

The system noise temperature can in turn be broken down in several contributions:

$$T_{sys} = T_{bg} + T_{sky} + T_{spill} + T_{rx} \tag{1.11}$$

where T_{bg} is the noise from the microwave background, T_{sky} is the noise from the atmospheric emission, T_{spill} is the noise due to spillover and ground scattering, T_{rx} is the receiver noise temperature. The first two terms are related to the environment, while the others depend on the characteristics of the antenna. A detailed calculation of the antenna temperature from its FFP and the noise contributions from Eq. (1.11) is presented in [4].

1.2.5 Antenna Efficiency

Another important parameter in antenna design is the efficiency, expressed as[2]:

$$\eta_A = \eta_1 \eta_2 \dots \eta_n \tag{1.12}$$

where the terms $\eta_1, \eta_2, \ldots, \eta_n$ represents different contribution to the efficiency, such as the aperture field efficiency, the blockage efficiency, surface error efficiency etc. An alternative expression of the efficiency for reflector antenna is a ratio between the effective and geometric areas:

$$\eta = \frac{A_{\text{eff}}}{A_g} \tag{1.13}$$

where A_g is the geometric area. The aperture efficiency depends on the illumination by the feed. The highest aperture efficiency corresponds to a uniform aperture illumination. However, radio telescopes have always a tapered (non uniform) illumination. Firstly, because the FFP of the feed cannot have a sharp cutoff at the aperture edge, so a uniform illumination would result in field radiated outside the reflector, contributing to the spillover. Second, solid angles from the feed to the same infinitesimal aperture sub area δA are not all equal[2]. In other words, the reflector itself introduces an aperture grading. The antenna surface error is discussed in more detail in Section 1.4.

1.3 Radio telescope systems

1.3.1 Single reflector antennas

In single reflector antenna, also known as prime focus system, the reflector has a parabolic shape and the feed is located at its focus. The main parameters describing the geometry of the system are the diameter of the

reflector D and it focal length F(Fig. 1.4). The ratio F/D, known as the focal ratio, determines the angular extension of the reflector surface as seen by the feed, denoted by the feed angle θ_F. For radio telescopes, the focal ratio is usually between 0.3 and 0.8. For a focal ratio of 0.43, the corresponding feed angle is $\theta_F = 120°$. Such values of focal ratio involve a space attenuation of the field proportional to $(r/\rho)^2$, r being the reflector radius and ρ the radial coordinate of the aperture. The attenuation introduces a tapering on the aperture field which, together with the feed pattern, contributes to the illumination efficiency. The first antenna purposely designed to be employed as a radio telescope was built by Grote Reber in 1937. This was a paraboloid of revolution, a direct radio analogue of an optical reflecting telescope. Radio astronomy, however, dealing with much larger wavelengths, cannot benefit from Geometrical Optics for a complete description of the properties of the system, and diffraction effects should be taken into account. The signal received from a star located along the axis of a linear paraboloid is concentrated on a small yet finite area rather than a single point, even neglecting the effects of the Earth's atmosphere. The distribution of the intensity is known in optics as the Airy disk.

The resolving power of the antenna depends on the ratio λ/D, and can be improved by using either a short wavelength or a larger diameter D for the telescope aperture. The first possibility is limited due to the absorption in the Earth's atmosphere, as already mentioned in Section 1.1. It is restricted also because astronomers are interested in specific wavelengths

corresponding to spectral characteristics of the source. In addition, the minimum feasible wavelength is proportional to the surface irregularities that are dependent on D as it will be shown in Section 1.4.

A spherical reflecting surface can be also be employed rather than a paraboloid. Unlike the latter, a spherical surface has no main optical axis and can receive radio waves from a wide angular range without being moved. The locus of the "focus" is a concentric spherical surface of half the radius of the reflector and the feed may be moved over this surface to observe different parts of the sky. Alternatively, many fixed feeds with individual receivers may be placed on this surface and used simultaneously so as to allow an 'image' of the sky to be constructed. In this case, though, only a small portion of the reflector is used by each feed to reduce the spherical aberration. A radial line feed or a specially shaped secondary mirror makes it possible to collect radiation from a larger part of the reflector.

Arecibo

The world's largest filled aperture radio telescope is at the Arecibo Observatory[5], located near Arecibo, Puerto Rico (USA), and is shown in Fig. 1.5. The main reflector of the telescope has a spherical profile with a diameter of 305 m and a radius of curvature of 265 m. The surface accuracy of about 2 mm Root Mean Square (RMS) limits the operating frequency to about 10 GHz. Since the huge main reflector is fixed, the beam is steered by moving the feeding system, which is suspended on a platform

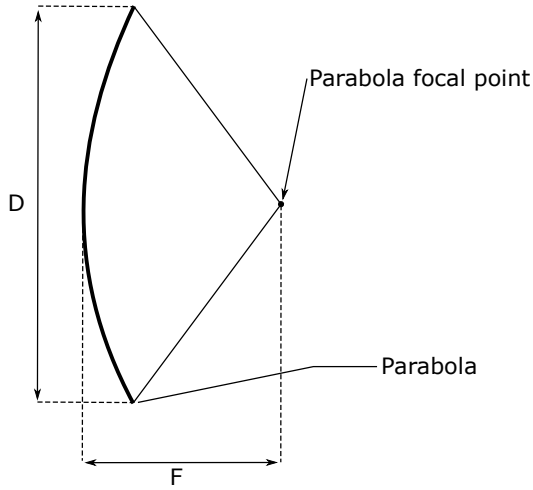

Figure 1.4. Geometry of a parabolic reflector.

above the dish. The platform has a rotating, bow-shaped track carrying the receiving antennas and secondary and tertiary reflectors. This allows the telescope to observe any region of the sky in a 40° cone of visibility about the zenith. The spherical reflector creates a caustic along a line focus at half the radius of curvature, independent of the direction of incidence, and the corresponding aberrations can be better taken into account by the feed design. The feed system is made up by a Gregorian secondary and tertiary reflectors, allowing standard feed horns to be used[6]. This results in a uniform illumination of an ellipse on the main reflector about 213 m × 237 m wide, with a beamwidth of 1 arcminute at 5 GHz.

Figure 1.5. The spherical Arecibo reflector in Puerto Rico.

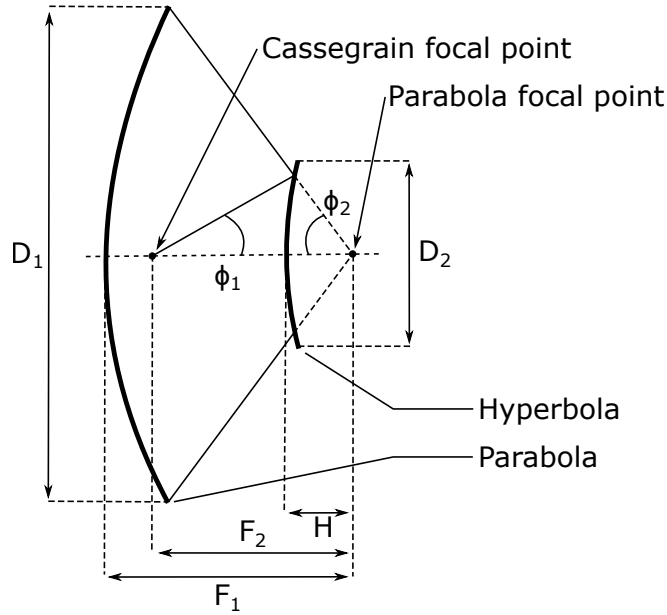

Figure 1.6. Geometry of the Cassegrain system.

1.3.2 Dual reflector systems

In this Section, the relevant parameters of dual reflector systems are presented. The attention will be focused on the geometry of the Cassegrain system, depicted in Fig. 1.6, which employs a parabolic main reflector and a hyperbolic secondary reflector. The results, however, are also valid for Gregorian systems, which on the other hand employ an elliptical secondary reflector. In the geometry shown in Fig. 1.6, one of the foci of the hyperboloid is the real focal point of the system, and is located at the center of the feed; the other is a virtual focal point and is located at the focus of the paraboloid. To completely describe the system, four parameters are required, two for each reflector. Of the seven parameters shown in Fig. 1.6, the four independent parameters usually chosen are the primary diameter D_1, its focal length F_1, the secondary half angle ϕ_2 and the distance between the hyperbola foci F_2. The other three are related to the these by the following equations:

$$\tan\frac{\phi}{2} = \pm\frac{1}{4}\frac{D_1}{F_1} \tag{1.14}$$

$$\frac{1}{\tan\phi_1} + \frac{1}{\tan\phi_2} = 2\frac{F_2}{D_2} \tag{1.15}$$

$$1 - \frac{\sin\frac{1}{2}(\phi_1 - \phi_2)}{\sin\frac{1}{2}(\phi_1 + \phi_2)} = 2\frac{H}{F_2} \tag{1.16}$$

where ϕ_1 is the primary half angle, D_2 is the secondary diameter, and H is the distance between the secondary vertex and the virtual focal point. The sign in Eq. (1.3.2) is positive for a Cassegrain geometry and negative for a Gregorian one. An important property of the Cassegrain system consists in being able to specify ϕ_2, which is directly related to the beamwidth required to the feed, independently of the focal ratio F_1/D_1, which in turn determines the shape of the main reflector. A useful tool for a quantitative analysis of the Cassegrain antenna is provided by the concept of *equivalent parabola*. As shown in Fig. 1.7, the combination of main and sub reflectors is considered as being replaced by a single focusing surface at a certain distance from the real focal point. The resulting surface is a paraboloid which would focus an incoming plane wave toward the real focal point in exactly the same manner as the Cassegrain system. The relationship between the equivalent parabola and the Cassegrain parameters are the following:

$$\frac{1}{4}\frac{D_1}{F_e} = \tan\frac{\phi_2}{2} \tag{1.17}$$

$$m = \pm\frac{F_e}{F_1} = \frac{\tan\frac{\phi_1}{2}}{\tan\frac{\phi_2}{2}} = \frac{e+1}{e-1} \tag{1.18}$$

where e is the eccentricity of the sub reflector and m is referred to as the magnification. Again, in Eq. (1.18), the positive sign applies to the Cassegrain geometry while the negative for the Gregorian one. As long as the off-axis beam is small, the equivalent parabola yields the same results regarding the description of important properties of the system, such as the coma aberration (defined in Section 1.4.2). When this angle becomes large, the approximation is no longer valid and thus the wide angle coma may differ considerably. The equivalent parabola may also be employed in the determination of the amplitude taper across the aperture of the antenna. For a single reflector antenna, the illumination is determined by the radiation pattern of the feed, modified by the "space-attenuation" characteristic, which depends on the focal ratio F/D. For a dual reflector system, the exact same process is valid, provided the equivalent focal length is used for the focal ratio, F_e/D_1. In other words, the illumination is exactly the same as the one of a single reflector having the equivalent focal length and illuminated by the same feed. One of the most important benefit of a dual reflector system is the possibility to place the feed in a convenient position, behind the main reflector. The rear location and forward pointing direction of the feed involves several advantages, especially for low noise applications such as radio astronomy. Low noise electronics often needs to be cooled to cryogenic temperatures, resulting in a bulky receiver. Therefore, having the receiver behind the main reflector reduces the mechanical load. A second advantage is related to the spillover noise

behavior of the radio telescope. A single reflector antenna suffers from a considerable amount of wide angle sidelobe response due to the spillover radiation from the small feed. This may introduce a substantial amount of noise into the antenna, by coupling to the radiation from the warm ground. In the case of a Cassegrain antenna, the main contribution comes from the spillover from the feed past the edge of the sub reflector. Although the total amount of spillover power may be comparable with that of a single reflector geometry, it is likely to be confined to directions relatively close to the antenna axis, and thus pointing towards the cold sky which produces significantly less noise. There is also the contribution due to the aperture blockage by the sub reflector. Again, this is typically significant only in forward directions. As a result of these directional properties, the spillover and aperture blocking couple to the ground only when the antenna is pointed at a low elevation angle.

1.3.3 Beamforming Arrays

The performance of single dish radio telescopes is limited by the receiver noise temperature and by the physical size of the reflector, which in turn is limited by mechanical considerations. An approach to circumvent these limitations is to employ arrays of smaller dishes distributed over a a greater area to improve the spatial selectivity of the instrument. The signal from each dish may be combined to form one or more beams which are useful for astronomical surveys. For wavelengths longer than about 1 m

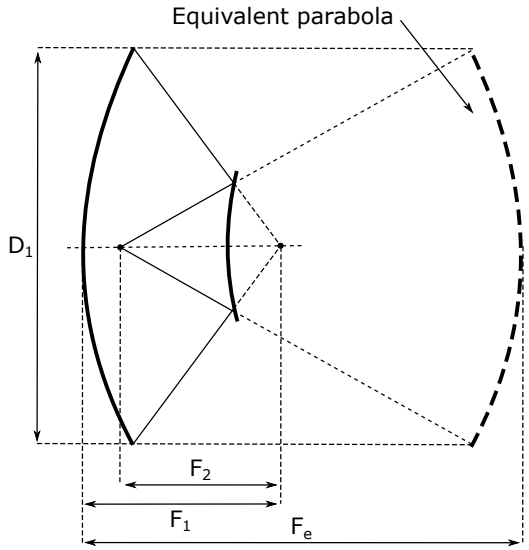

Figure 1.7. Geometry of the equivalent parabola for a Cassegrain system.

(300 MHz), it becomes cost effective to employ a larger number of lower gain antennas, such as dipoles, instead of reflector. Indeed, small reflector antennas show poor directivity at these wavelengths and an increased noise temperature[7]. Beamforming arrays consisting of large numbers of low gain elements have some unique issues, including variation of beam shape and sidelobes as a function of pointing, degradation of sensitivity with increasing zenith angle, and a higher overall system complexity. Beamforming arrays allow to combine the signals from individual antennas to generate multiple beams simultaneously. Each beam can be pointed independently, greatly increasing the observing capabilities over a single dish system.

Long Wavelength Array Station 1 (LWA1)

An example of a such systems is given by the LWA1[8], a radio telescope operating in 10-88 MHz located in New Mexico (USA). The LWA1 began regular operations in 2015 and its key science drivers are the study of relativistic particles, cosmic evolution, astrophysical plasma and transient phenomena like giant flares from magnetars. LWA1 consists of one station with 256 dual polarized dipole antennas, with the end goal to realize 53 stations, for a total of 13000 antennas. Each antenna element is a wire grid bow-tie dipole, having dipole arms angle downward to provide a uniform gain over the sky. The output signal from each antenna is sampled, and the beam forming is carried out using digital techniques. The dipoles are distributed within an elliptical aperture, resulting in a beamwidth that ranges from 2° at the highest frequencies to tens of degree at the lowest. The distribution of the antennas is pseudorandom and optimized to improve the grating lobes.

1.3.4 Interferometers

A distinct category of radio telescopes is aperture synthesis imaging instruments, often referred to as interferometer arrays or simply as interferometers. Instruments in this category are designed primarily for imaging, in contrast to the single pixel per feed mode of operation associated with single dish instruments and beamforming arrays. These instruments are also routinely used for imaging, by sweeping the beam across the desired

field of view. Interferometers, on the other hand, are explicitly designed for aperture synthesis imaging. In this section, the Radio Interferometry theory is briefly introduced to discuss its advantages in increasing the observation resolution of radio telescopes. As an example, let us consider an interferometer made up by two antennas, as shown in Fig. 1.8, where $\underline{B}$ is the baseline vector and $\underline{s}$ is the unit vector pointing towards the radio source. Due to the displacement, the received signal from one of the antennas will have a time delay relative to the other equal to:

$$\tau = -\frac{\underline{B} \cdot \underline{s}}{c} \tag{1.19}$$

where c is the speed of light in vacuum. The corresponding phase delay of the wavefront can be written as:

$$\Delta\varphi = \omega\tau \tag{1.20}$$

where ω is the angular frequency. Radio interferometers can be divided in two broad categories based on how the signals from the different antennas are combined: adding interferometers and correlation interferometers. An adding interferometer is simply a phased array, which allows to point the beam by compensating the phase delay electronically instead of physically moving the antenna elements. In a correlation interferometer, the signals are multiplied and accumulated (cross-correlated) instead of being added. The correlation between two real signals V_1 and V_2 is defined as:

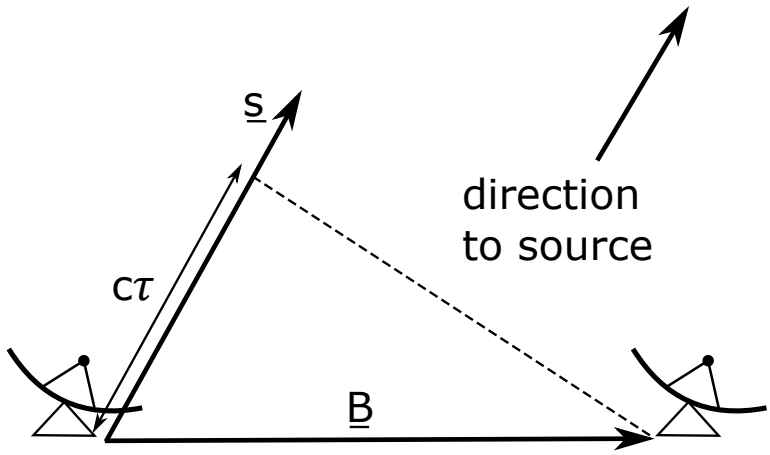

Figure 1.8. Geometry of the interferometer baseline between two radio telescopes.

$$\langle V_1, V_2 \rangle = \int V_1(t) V_2(t+\tau)\, \mathrm{d}\tau \tag{1.21}$$

An appealing property of this category of interferometer is that random noise terms present in the signal received by each antenna are suppressed, as there is no correlation between them. Denoting as V_{ks} the signal received by the kth antenna and V_{kn} the corresponding noise term, assumed to be Additive White Gaussian Noise (AWGN), the outputs from an adding interferometer and a correlation interferometer can be expressed respectively

as:

$$\begin{aligned}\langle (V_{1s}+V_{2s}+V_{1n}+V_{2n}),(V_{1s}+V_{2s}+V_{1n}+V_{2n})\rangle = \\ = V_{1s}^2+V_{2s}^2+V_{1n}^2+V_{2n}^2+2V_{1s}V_{2s}\end{aligned} \tag{1.22a}$$

$$\langle (V_{1s}+V_{1n}),(V_{2s}+V_{2n})\rangle = V_{1s}V_{2s} \tag{1.22b}$$

Where the cross correlations in Eq. (1.22b) cancel out because the noise terms received by the two antennas are uncorrelated. Thus, the correlation interferometer has superior performance since it is ideally free from noise terms if the statistics of the signal are negligible. The cross correlation term is the visibility function, which is related to the Fourier transform of the source intensity distribution[9]. The visibility is a function of the baseline vector and is conveniently expressed in a rectilinear coordinate system (u,v,w), where the w-direction is chosen along $\underline{s}$ and u and v are chosen aligned with the projected local eastward and northward directions, respectively (Fig. 1.9). The $w=0$ plane is perpendicular to the source direction and is commonly referred to as the uv-plane. If the visibility is known across the uv-plane, the source distribution can be derived through an inverse Fourier transform. This is a fundamental result known as the Van Cittert-Zernike theorem[10], which requires two basic assumptions. The first is that the source distance can be considered infinite and the brightness is measured in two dimensions, without the depth. The second

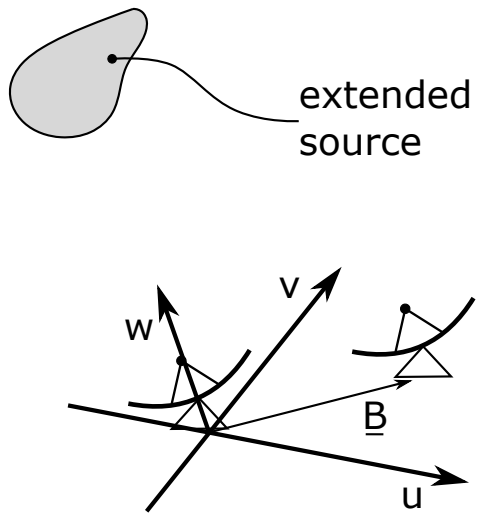

Figure 1.9. Baseline and interferometry reference system.

assumption is that the signal is received from a small portion of the celestial sphere centered on a particular direction, called the phase tracking center.

An aperture synthesis telescope consists of an array of antennas that acts as a correlation interferometer to measure the visibility function. The sampling in the uv-plane is also enhanced by exploiting the Earth's rotation. Another advantage of using a cross correlation operation is that not only the amplitude but also the phase is measured. As is discussed in Chapter 2, the response of the antenna in both amplitude and phase can be also used in the holographic measurement of the antenna surface by correlating it to the response of another reference antenna. The reference antenna is usually fixed or has a wide, flat main beam so that the phase difference measured

represents the phase distribution of the main antenna pattern. Through the Fourier transform of the complex pattern, the surface deviation from the ideal shape can be derived with high accuracy.

Very Large Array (VLA)

An example of radio interferometer is given by the VLA[11] located in New Mexico (USA). The radio telescope comprises 27 independent reflector antennas, each of which has a main dish diameter of 25 m. The antennas are arranged on three arms forming a y shape, shown in Fig. 1.10. The antennas can also be moved along the arms to change the interferometer baseline, up to 36 km, and can be arranged in four different configurations depending on the desired resolution and field of view. The individual reflectors adopt a symmetric Cassegrain geometry. The vertex of the main reflector accommodates eight different horn feeds designed to cover eight corresponding contiguous bands from 1 GHz to 50 GHz. The 2.3 m secondary reflector is slightly tilted relative to the axis of revolution of the primary, to ease the feed selection by rotating the secondary around this axis. Two additional dipole feeds are available to cover lower frequency bands, namely the "P-band" (230-470 MHz) and the "4-band" (54-83 MHz).

Figure 1.10. Reflector antennas of the VLA.

LOw-Frequency ARray (LOFAR)

Another example of radio interferometer is given by the LOFAR, an array currently consisting of ten stations, distributed in Northern Europe[12] (Fig. 1.11). Each station consists of a low band array (LBA) operating at 10-90 MHz, and a high band array (HBA) operating at 110-240 MHz. The LBA array consists of of 48 or 96 dual polarized thin dipole antennas over a ground screen. The antennas are distributed in a pseudorandom geometry within a circular area about 80 m in diameter. HBA array consist of 24, 48 or 96 sub-arrays, each one in turn made up by 16 (4×4) wire grid dipoles arranged in a rectilinear geometry. The stations themselves are arranged in a pseudorandom geometry with baselines ranging from 68 m to 1158 km,

Figure 1.11. Part of the core of the extended telescope located near Exloo, The Netherlands, on which six LOFAR stations are housed.

allowing an imaging resolution ranging from 0.5° to sub-arcsecond scales.

The Square Kilometer Array

The Square Kilometer Array (SKA) is a future radio telescope which will scan and map the sky with a sensitivity of two orders of magnitude higher than present-day radio telescopes[13]. The SKA is planned to be operational in 2020; it will ultimately operate over a large frequency bandwidth, ranging from approximately 70 MHz to more than 25 GHz, with an equivalent collecting area of approximately $1\,\mathrm{km}^2$, which is unprecedentedly large. The technological challenge is its realization is to minimize the system-noise temperature, which is a non trivial task for non-cooled antenna systems.

The SKA project is a long-term international endeavor during which a number of different antenna technologies are considered to operate in each frequency band. Today, SKA comprises different projects coordinating multiple national and international instrument development programs, referring to different antenna technologies are considered to operate in each frequency band.
The first iteration, referred to as “SKA Phase 1”, consists of three instruments:

1. SKA Low, a meter-wavelength array consisting of 900 stations in Western Australia, each of which equipped with 300 dual polarized log-periodic Yagi antenna.

2. SKA Mid, an array of several thousand reflector antennas (around 200 to be built in Phase 1) to cover the frequency range 350 MHz-14 GHz. The antenna design will adopt an offset Gregorian geometry having a height of 15 m and a width of 12 m. SKA Mid is an expansion to the current MeerKAT radio telescope, consisting of 64 antennas.

3. SKA Survey array, which will be an expansion of the existing Australian SKA Pathfinder (ASKAP), a compact array of single reflector antennas of 15 m diameter each, each equipped with a multi beam Phased Array Feed (PAF), covering the frequencies from 350 MHz to 4 GHz.

1.4 Influence of Imperfections on Performance

In this section the factors that determine the beam characteristics and efficiency of the antenna are discussed. These are of high interest both during the design of the antenna and during its use. The major parameter *aperture efficiency* can be broken down into several components, each representing a basic characteristic or a deviation from the perfect situation. This enables us to set conditions on these imperfections for a given loss of efficiency, and these can be directly introduced into the design of the structural, mechanical, thermal and electromagnetic realization of the antenna. The imperfections in the antenna structure determine the "quality" of the beam, which in turn influences the reliability of the received signal. The *aperture efficiency* can be written as the product of a number of individual efficiency contributions:

$$\eta_a = \eta_i \cdot \eta_s \cdot \eta_p \cdot \eta_b \cdot \eta_r \cdot \eta_\sigma \cdot \eta_\Sigma \cdot \eta_F \tag{1.23}$$

where

η_i is the illumination efficiency of the aperture by the feed function (taper);

η_s is the spillover efficiency of the feed and subreflector, if present;

η_p is the polarization efficiency of the feed/reflector system;

η_b is the blocking efficiency due to aperture blocking by quadripod,

subreflector, etc;

η_r is the radiation efficiency of the reflector surface due to ohmic loss;

η_σ is the small-scale surface error efficiency;

η_Σ is the large-scale surface error efficiency;

η_F is the focus error efficiency due to misalignments.

The first three terms are fully determined by the electromagnetic design of the reflector and feed combination. The remaining terms depend on the structural deviations from a perfect situation due to material and environmental restrictions such as finite stiffness of structural members and the influence of gravity, wind and temperature variations. In the following we will focus on the last three terms pertaining the effects of the reflector deviations from its nominal shape and misalignments of the structure.

1.4.1 Small scale surface errors

In (1.23), the effects of small-scale and large-scale deviations of the reflector from the prescribed geometrical shape are separated. The deviations cause phase errors over the aperture that result in less than perfect interference of the reflected wavefronts in the focus and hence to a loss in the aperture efficiency. The power that is removed from the forward beam direction is spread over the sidelobes of the antenna pattern. Depending

on the spatial distribution of the surface deviations, different effects may occur such as main beam broadening, asymmetrical sidelobe structure, and sidelobe enhancement. The distortions are caused by fabrication errors in the reflector panels, imperfect localization of the panels on the backup structure and deformation of the panels and backup structure under influence of gravity, wind and temperature differences. The separation between small-scale and large-scale deviations is based on their different nature. Small-scale errors are correlated over areas of the order of the surface panels or less. They are caused by manifacturing error and local deformation of the individual panels due to gravity or temperature as well as errors in the adjustment of the panels of the prescribed reflector contour. As far as these errors can be considered randomly distributed over the aperture with an RMS value ϵ_σ and with a correlation length c_σ, i.e. the distance over which the errors are spatially correlated, that is much larger than the wavelength and much smaller than the reflector diameter, their effect can be described by the *tolerance theory* of Ruze[14], [15]. The gain loss depends on the ratio of the error ϵ_σ to the wavelength λ. The relation, known as *Ruze formula*, is given by

$$\eta_\sigma = \exp\left[-(\frac{4\pi\epsilon_\sigma}{\lambda})^2\right] + (\frac{c_\sigma}{D})^2 \cdot \left\{1 - \exp\left[-(\frac{4\pi\epsilon_\sigma}{\lambda})^2\right]\right\} \tag{1.24}$$

where c_σ is the correlation length and D the reflector diameter. The radiation, scattered by the errors and removed from the main beam, can be seen

as a level error pattern, whose width depends on the correlation length c_σ. The first term in Eq. (1.24) represents the loss in gain, while the second term represents the maximum level of the *error pattern*. Generally, the contribution of the second term is negligible, less than 1% for $c_\sigma/d < 0.1$. The ratio of power in the error pattern to that in the main beam is only dependent on the magnitude of the RMS error . For an error of $\lambda/20$, the power in the error beam is about half of that in the main beam, which is equivalent to a loss in main beam gain of 1/3. As shown by Eq. (1.24), the peak level of error pattern relative to the main beam level is proportional to the square of the ratio c_σ/D. A small value of c_σ, that is, many small independent error patches, produces a very weak but also very wide error pattern. Few large correlated areas cause a narrow error beam with an increase of its peak level.

1.4.2 Large scale deformations

Large-scale deformations of the reflector surface originate from the supporting structure and its mount, which are related to the manufacturing and alignment accuracy, and from deformation behavior under environmental influences including gravity. Thus, the analysis and mathematical description of these deformations provide a direct connection between structural design methods, such as Finite Element Analysis (FEA), and the resulting distortion of the antenna beam pattern known as *aberrations*. The description of the antenna aberrations draws from the theory of op-

tical systems, which is detailed in[10]. There are five primary aberrations first introduced by Seidel in 1856[16] and known as astigmatism, coma, spherical aberration, field curvature and distortion. The names used for primary aberrations come from the ray optics theory, which can useful for describing their properties.

Astigmatism originates when the focus of rays within the plane containing the axis of the system and an off axis source (tangential plane) is different from the focus if rays within the perpendicular plane (sagittal plane). Astigmatism is inversely proportional to the focal ratio of the system.

Coma is due to off-axis rays do not converge at the same point of the focal plane, creating a blur which resembles a comet. It is the dominant aberration in a classical Cassegrain system in off-axis configuration. In this case, the coma increases linearly with the offset angle. It can be reduced by increasing the focal ratio of the system. Coma can also appear due to a misalignment between the primary and secondary reflector.

Spherical aberration is due to the fact that rays do not converge at the same point. In other words there is no single focus and the effect is independent of the angle. The term comes from the property of spherical mirrors to exhibit this aberration. Spherical aberration can also arise in a dual reflector system due to mismatching conic constants between the primary and secondary.

Field curvature occurs when the “image” forms on a curved surface

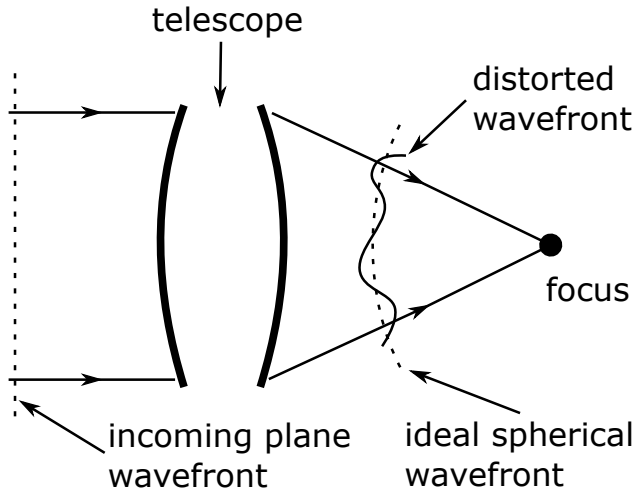

Figure 1.12. A wavefront propagating through the telescope. The wavefront error is the deviation of the outcoming wavefront from a sphere.

rather than a plane.

A rigorous way to describe the aberrations can be achieved introducing the notion of *wavefront error*. The incoming field from a celestial source can be represented by a plane wave propagating towards the radio telescope. The wave reflected by a perfect system would be spherical wave with its center located at the focus. However, in a real telescope the reflected wavefront is not exactly spherical. The deviation of the wavefront from a plane or sphere is referred to as the wavefront error (Fig. 1.12). The magnitude of the error is generally measured as the RMS of the deviation over the entire surface of the wavefront and expressed in µm or as a fraction of the wavelength. It is important to note that the aberrations represent deviations of the imaging element, in the case at hand represented by the

reflector, sub-reflector if present, and the feed. If the distorted wavefront, and thus the relative phase function, can be determined by calculation or measurement, it is possible to incorporate it into the radiation integral and evaluate the beam of the antenna showing deviations in shape and intensity. A useful analytic representation of the wavefront can be achieved by projecting it into components represented by the primary aberrations. Frits Zernike (1888-1966) achieved such decomposition in 1934 during his work on phase-contrast microscopy for which he received the Nobel Prize in Physics in 1953. He introduced a set of orthogonal polynomials which are known as the Zernike polynomials. Using polar coordinates over the aperture where ρ is the normalized radius and ϕ is the polar angle, the wavefront $W(\rho, \phi)$ can be expressed as a linear combination of these polynomials:

$$W(\rho, \phi) = \sum_n a_n Z_n(\rho, \phi) \tag{1.25}$$

where $Z_n(\rho, \phi)$ is the Zernike polynomial of order n and a_n is the corresponding coefficient. The Zernike polynomials depend on the shape of the aperture and on its possible obstruction. In Table 1.1, the Zernike polynomials up to the fifth order are shown for a circular aperture. The shape of the four major aberrations is sketched in Fig. 1.13. These are plots of the Zernike polynomials pertaining to the specific aberration. They correspond to the shape of the reflected wavefront produced by a distorted reflector.

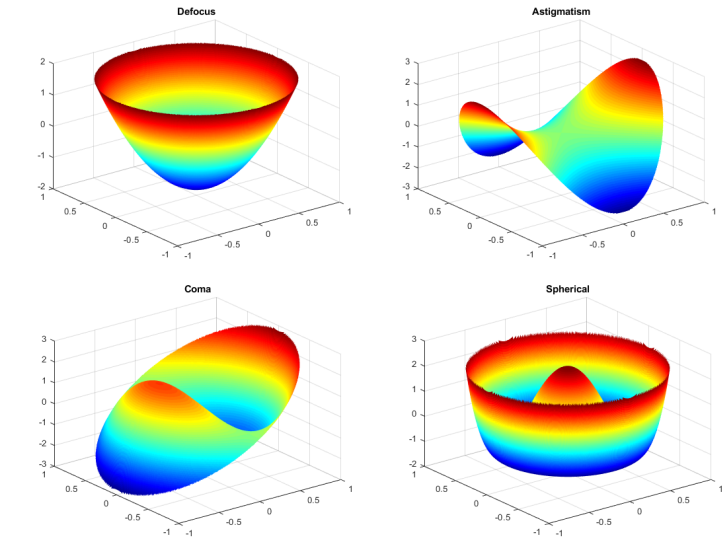

Figure 1.13. Sketch of the major optical aberrations defocus, astigmatism, coma and spherical aberration.

1.4.3 Effects of misalignments

For an optimal performance of the antenna, it is important that the system is properly focused. For a single reflector antenna this means positioning the phase center of the feed in the focus of the primary paraboloid. In addition, in a dual reflector system, it is important that the focus of the hyperboloidal secondary reflector coincides with the focus of the paraboloid. The general case of an arbitrary shift of the feed from the true position, denoted by the defocus δ, can be separated in two components: an axial defocus δ_a along the reflector axis and a lateral defocus δ_l perpendicular to the reflector axis. Let us denote as ψ the angle between the

reflector axis and a ray from the focus to a point on the surface at radius ρ. It is then possible to calculate the path-length difference between such a ray and the central, on axis, ray for both axial and lateral defocus. The resulting radiation pattern and parameters of the defocused system can be calculated by incorporating the phase error function in the basic radiation integral. It is assumed that the defocus is small with respect to the focal length of the reflector, i.e. $\delta/F \ll 1$, in order to neglect terms of order $(\delta/F)^2$.

Lateral defocus

The first case of a lateral defocus where the feed is moved from the focal point O to the point O$'$, as illustrated in Fig. 1.14. Applying the cosine rule to the triangle POO$'$, where P is a point on the reflector surface at radius ρ, we have

$$r_{PO'}^2 = r_{PO}^2 + \delta^2 - 2\delta r_{PO} \sin\psi \cos\phi \tag{1.26}$$

and using the Taylor series expansion for the square root

$$r_{PO'} = r_{PO}(1 - \frac{\delta}{r_{PO}} \sin\psi \cos\phi + \frac{\delta^2}{2r_{PO}^2} - \frac{\delta^2}{2r_{PO}^2} \sin^2\psi \cos^2\phi) \tag{1.27}$$

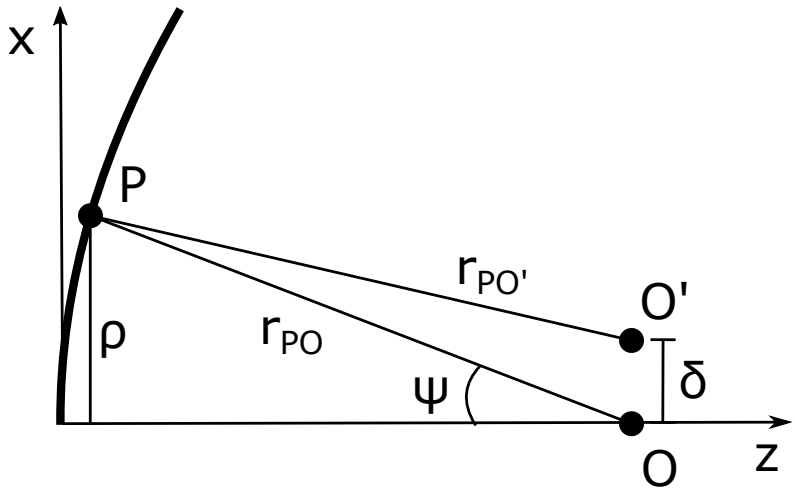

Figure 1.14. The geometry of the lateral defocus in the plane of feed translation.

where the terms of order higher than $(\delta/r_{PO})^2$ have been neglected. Thus the path length difference Δ_l is

$$\Delta_l = r_{PO'} - r_{PO} = -\delta \sin\psi \cos\phi + \frac{\delta^2}{2r_{PO}} - \frac{\delta^2}{2r_{PO}} \sin^2\psi \cos^2\phi \quad (1.28)$$

Using the parabola equations, Δ_l can be expressed as a function of ρ eliminating both r_{PO} and ψ

$$\Delta_l = -\frac{\delta}{F}\rho\cos\phi + \frac{\delta}{4F^3}\rho^3\cos\phi - \frac{\delta^2}{8F^3}\rho^2 - \frac{\delta^2}{2F^3}\rho^2\cos^2\phi + \frac{\delta^2}{2F} \quad (1.29)$$

The terms in this equation represent some of the well known aberrations in optical instrument theory[10] introduced in Section 1.4.2. The first term corresponds to the *distortion*, also known as as *tilt* or *squint*. It causes

a shift of the beam maximum to an off-axis angle without changing its shape. The second term is the *coma* effect, linear in δ but proportional to ρ^3. It causes a beam shift in the opposite direction by a smaller amount than the first term and introduces an asymmetric beam distortion with a strong sidelobe on one side, known as the *coma lobe*. The third term is the *field curvature*, quadratic in r and independent of ϕ. It is reminiscent of an axial defocus, but the influence of the term is not identical to that, because it is of second order in δ and inversely proportional to F^3 instead of F^2. The fourth term is called *astigmatism*, characterized by features in the beam which are four-fold over the aperture. The pathlength error for the central ray ($\rho = 0$) is $r_{PO'} - r_{PO} = \delta^2/(r_{PO'} + r_{PO}) \approx \delta^2/2r_{PO}$, which is equal to the second term in Eq. (1.28). It is useful to note that the field curvature term reflects the fact that there is a curved surface in the focal region on which the image is most sharp, known as the *Petzval surface*[17]. Thus the optimum location of a laterally displaced feed will involve also a correction to its axial position. In [17], a corrective formula is given for the axial displacement needed to place a laterally displaced feed on the Petzval surface:

$$\delta_a = \frac{\delta_l^2}{2F} \tag{1.30}$$

Thus the optimum locus of an off-axis feed lies on a paraboloid with a focal length equal to half of that of the main reflector and the off-axis feed should be moved slightly away from the vertex of the paraboloid.

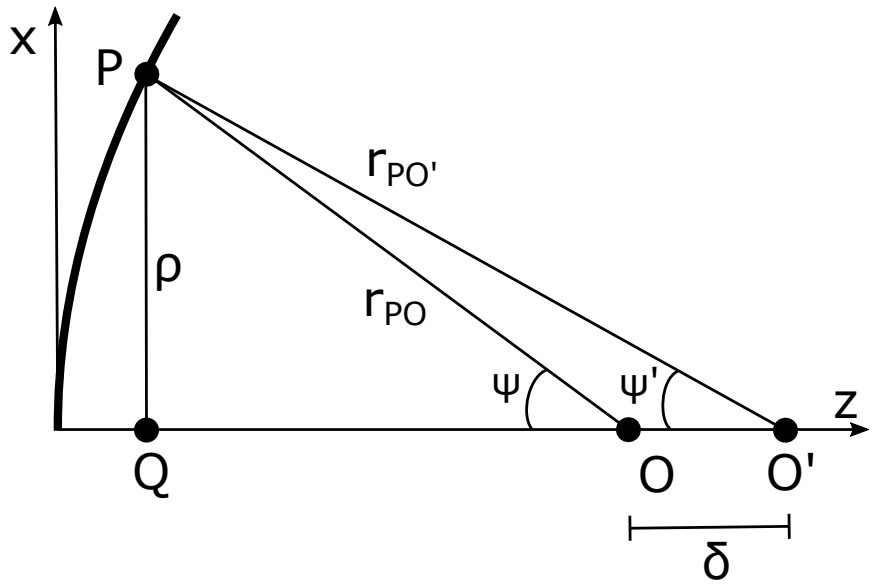

Figure 1.15. The geometry of the axial defocus.

Axial defocus

Let us consider the case of an axial defocus where the feed is moved away from the focal point along the reflector axis, as illustrated in Fig. 1.15. The defocus is assumed to be small with respect to the focal length, and we calculate the path-length difference from the defocused feed to the aperture plane between the on axis ray and the ray leaving the feed at an angle ψ with respect to the reflector axis. The path length change of the central ray in the defocused case is δ. Using the geometrical relations for the parabola, the path length from O to the vertex and from there to the

aperture plane at a radius ρ is

$$r_{PO} = F + z(\rho) = F + \frac{\rho^2}{4F} = F(1 + \tan^2(\frac{\psi}{2})) \tag{1.31}$$

The distance r_{PO} from O to a point P on the reflector can be expressed as

$$r_{PO} = \frac{2F}{1+\cos\psi} = F\left[\frac{1+\cos\psi}{1+\cos\psi} + \frac{1-\cos\psi}{1+\cos\psi}\right] = F(1 + \tan^2(\frac{\psi}{2})) \tag{1.32}$$

which is identical to the value for the central ray, as the geometry of the parabola requires. Applying the cosine rule to the triangle $\mathrm{POO'}$ we have

$$r_{PO'}^2 = r_{PO}^2 + \delta^2 - 2r_{PO}\delta\cos(\pi - \psi) = r_{PO}^2 + \delta^2 + 2r_{PO}\delta\cos\psi \tag{1.33}$$

from which we obtain the path length change of the ray to P

$$r_{PO'} - r_{PO} = \frac{2r_{PO}\delta\cos\psi + \delta^2}{r_{PO'} + r_{PO}} \approx \delta\cos\psi + \frac{\delta^2}{2r_{PO}} \approx \delta\cos\psi \tag{1.34}$$

and thus the path error over the aperture is given by

$$\Delta_a(\rho) = \delta(\cos\psi - 1) = -\delta\frac{2\tan^2\frac{\psi}{2}}{1+\tan^2\frac{\psi}{2}} = -2\delta\frac{\left(\frac{\rho}{2F}\right)^2}{1+\left(\frac{\rho}{2F}\right)^2} \tag{1.35}$$

This result is obtained by ignoring the term δ^2 and assuming $r_{PO'} + r_{PO} = 2r_{PO}$. The same result can be obtained also by applying Pythagoras' law

to the triangles OPQ and O′PQ, which leads to

$$\Delta_a(\rho) = \sqrt{\left\{\rho^2 + \left(F - \frac{\rho^2}{4F} + \delta\right)^2\right\}} - \left(F + \frac{\rho^2}{4F} + \delta\right) \tag{1.36}$$

which can be rearranged as

$$\Delta_a(\rho) = \sqrt{\left(F + \frac{\rho^2}{4F} + \delta\right)^2 - \frac{\delta\rho^2}{F}} - F + \frac{\rho^2}{4F} + \delta = \sqrt{a^2 - \frac{\delta\rho^2}{F}} - a \tag{1.37}$$

where $a = \left(F + \frac{\rho^2}{4F} + \delta\right)$.

The series expansion of the root square leads to

$$\Delta_a(\rho) \approx a\left(1 - \frac{\delta\rho^2}{2Fa^2}\right) - a = -\frac{\delta\rho^2}{2Fa} = -\frac{\delta\rho^2}{2F}\frac{1}{F + \frac{\rho^2}{4F} + \delta} \tag{1.38}$$

Enforcing the assumption that $\delta \ll F$ we obtain

$$\Delta_a(\rho) = -\frac{\delta\rho^2}{2F}\frac{1}{F\left(1 + \frac{\rho^2}{4F^2} + \frac{\delta}{F}\right)} \approx -2\delta\frac{\left(\frac{\rho}{2F}\right)^2}{1 + \left(\frac{F}{2F}\right)^2} \tag{1.39}$$

which is equal to Eq. (1.35). So far we have dealt with the movement of the feed near the primary focus of a paraboloidal reflector. The results are valid without any change for the axial defocus of the feed in the secondary focus of a Cassegrain reflector configuration. In this case, however, we have to consider the equivalent paraboloid introduced in Section 1.3.2 with focal length m times that of the real primary, where m is the magnification factor of the Cassegrain system.

Aberration	Term	Value
Piston	Z_1	1
Horizontal Tilt	Z_2	$2\rho\cos\phi$
Vertical Tilt	Z_3	$2\rho\sin\phi$
Defocus	Z_4	$\sqrt{3}(2\rho^2-1)$
Vertical Astigmatism	Z_5	$\sqrt{6}\rho^2\cos 2\phi$
Oblique Astigmatism	Z_6	$\sqrt{6}\rho^2\sin 2\phi$
Horizontal Coma	Z_7	$\sqrt{8}(3\rho^3-2\rho)\cos\phi$
Vertical Coma	Z_8	$\sqrt{8}(3\rho^3-2\rho)\sin\phi$
Horizontal Trefoil	Z_9	$\sqrt{8}\rho^3\cos 3\phi$
Vertical Trefoil	Z_{10}	$\sqrt{8}\rho^3\sin 3\phi$
Spherical	Z_{11}	$\sqrt{5}(6\rho^4-6\rho^2+1)$
Secondary vertical Astigmatism	Z_{12}	$\sqrt{10}(4\rho^4-3\rho^2)\cos 2\phi$
Secondary oblique Astigmatism	Z_{13}	$\sqrt{10}(4\rho^4-3\rho^2)\sin 2\phi$
Horizontal Quatrefoil	Z_{14}	$\sqrt{10}\rho^4\cos 4\phi$
Vertical Quatrefoil	Z_{15}	$\sqrt{10}\rho^4\sin 4\phi$
	Z_{16}	$\sqrt{12}(10\rho^5-12\rho^3+3\rho)\cos\phi$
	Z_{17}	$\sqrt{12}(10\rho^5-12\rho^3+3\rho)\sin\phi$
	Z_{18}	$\sqrt{12}(5\rho^5-4\rho^3)\cos 3\phi$
	Z_{19}	$\sqrt{12}(5\rho^5-4\rho^3)\sin 3\phi$
	Z_{20}	$\sqrt{12}\rho^5\cos 5\phi$
	Z_{21}	$\sqrt{12}\rho^5\sin 5\phi$
Fifth order spherical	Z_{22}	$\sqrt{7}(20\rho^5-30\rho^4+12\rho^2-1)$

Table 1.1. First Zernike polynomials for a clear circular aperture.

Chapter 2

Radio Telescope Diagnosis Methods

As mentioned in Chapter 1, the performance of radio telescopes is heavily influenced by structural variations due for instance to:

- Misalignment of the feeding structure, resulting in a lateral or axial displacement of the receiver;
- Wind stress;
- Gravitational distortion as the antenna is tilted;
- Thermal distortion with ambient temperature or sunlight.

To guarantee the best performance for such systems, a continuous monitoring, the diagnosis and the subsequent reassessment of the Antenna

Under Test (AUT) is mandatory. Large reflector antennas, as those used in deep-space communications and radio astronomical telescopes, are often composed of a set of panels, supported on three or more adjustable points by a backup structure. After the assembly of the antenna, the panels must be accurately located onto the desired surface, and usually require periodic re-adjustment of their position during the radio telescope's lifetime. In this Chapter, an overview on radio telescopes diagnosis approaches are presented. Early diagnosis method were based on direct measurements using mechanical or optical instruments, such as the "theodolite-tape"[18], or photogrammetry. These techniques are presented in Section 2.1.

Direct diagnosis methods, even if valid during the installation stage, have been superseded by indirect methods, based on the elaboration of the electromagnetic signal received by the AUT. The electromagnetic diagnosis allows not only a greater accuracy, but also a simpler measurement set-up requiring little direct human intervention, which helps to reduce the idle time forced by the maintenance activity. Among the indirect diagnosis solutions, microwave holography, presented in Section 2.3, is the most widespread. Introduced by Scott and Ryle[19], microwave holography requires the measurement of the FFP of the AUT in both amplitude and phase and it is based on the well known relationship between the induced surface currents and the radiated field.

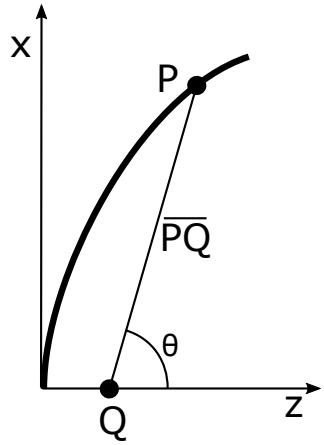

Figure 2.1. Geometry of the theodolite and tape measurement. A theodolite is positioned in Q, allowing the measurement of the angle θ. The radial distance is then measured by exteding a tape to the targets present on the reflector surface.

2.1 Direct Methods for Reflector Diagnosis

2.1.1 Theodolite and Tape

The first and simplest approach to the reflector surface measurment was the geodetic "theodolite and tape" method[20]. During the measurements, the reflector is positioned upwards, pointing towards the zenith. Deformations due to gravity at different elevations are not taken into account. To allow this technique, proper measurement targets are applied to the reflector, close to the positions of the panels adjustment screws. The targets are used for radial and angular measurements from a fixed position Q, as shown in Fig. 2.1. The radial measurements are made with calibrated tape suspended under controlled tension between Q and the targets, taking

into account its gravity deformation and thermal dilation.

Measurement accuracy of 0.1 mm can be obtained[21].

Improvements to the equipment over the years have led to the use of laser based theodolites, able to combine angle and distance measurement into a single instrument. Such instruments were used for the setting of a prototype antenna for ALMA[22], achieving an accuracy of about 30 µm.

2.1.2 Photogrammetry

Photogrammetry is based on the principle of triangulation. By taking photographs from at least two different locations, the so called "lines of sight" (or rays) can be traced from each camera to reflective targets points distributed on the surface. The lines of sight are then intersected to produce the accurate position of the points. Photographs can also be shot with a single camera by exploiting an azimuth movement of the antenna. This technique allow for the diagnosis with the radio telescope pointing at different elevations. The achieved accuracy is of the order of 40-70 µm[23].

2.2 Antenna Radiation Analysis

2.2.1 Aperture Field Method

The Aperture Field Method (AFM)[2] allows the evaluation of the radiated FFP from the knowledge of the electric field $\underline{E}$ on the plane $z = 0$, referred to as the Aperture Plane (AP) and depicted in Fig. 2.2. Let

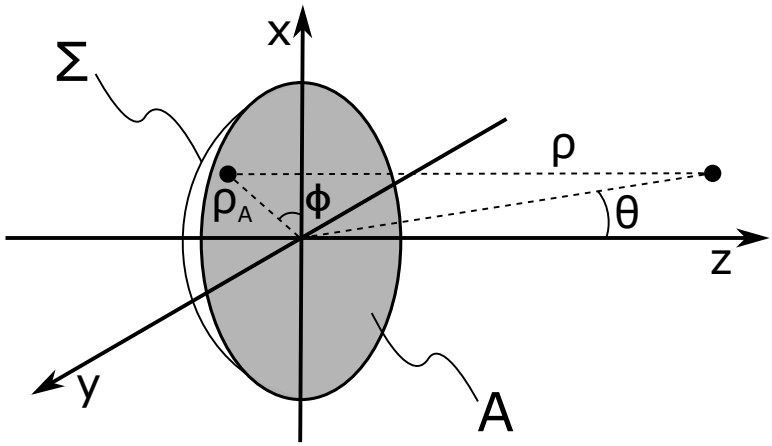

Figure 2.2. Geometry of the reflector antenna aperture.

us define the Aperture Field (AF) $\underline{E}_a$ as the vector of the components of the electric field tangent to the AP. The sources of the scattered field, i.e. the current induced on the reflector by the feed, are located in the region $z < 0$. Thus, for $z > 0$, $\underline{E}$ satisfies the homogeneous Helmholtz equation:

$$\nabla^2 \underline{E} + \beta^2 \underline{E} = 0 \tag{2.1}$$

where $\beta = 2\pi/\lambda$. Let us consider the Fourier Transform of a generic function z of two variables, defined as

$$\mathcal{Z}(k_x, k_y) = \mathfrak{F}\left[z(x,y)\right] = \iint_{\mathbb{R}^2} z(x,y) e^{jxk_x + jyk_y} \, \mathrm{d}x\mathrm{d}y \tag{2.2}$$

with the inverse Transform being

$$z(x,y) = \mathfrak{F}^{-1}\left[\mathcal{Z}(k_x,k_y)\right] = \frac{1}{4\pi^2}\iint\limits_{\mathbb{R}^2} \mathcal{Z}(k_x,k_y)e^{-jxk_x - jyk_y}\,\mathrm{d}k_x\mathrm{d}k_y \quad (2.3)$$

Applying the Fourier Transform with respect to x and y, Eq. (2.1) can be written as

$$\frac{\partial^2 \underline{\tilde{E}}(k_x,k_y,z)}{\partial z^2} + k_z^2 \underline{\tilde{E}}(k_x,k_y,z) = 0 \quad (2.4)$$

where $\underline{\tilde{E}}$ is the Fourier Transform of $\underline{E}$ with respect to x and y, and

$$k_z^2 = \beta^2 - k_x^2 - k_y^2 \quad (2.5)$$

The general solution of Eq. (2.4) is a plane wave propagating in the z-axis direction of the form

$$\underline{\tilde{E}}(k_x,k_y,z) = \underline{\hat{E}}(k_x,k_y)e^{-jk_z} \quad (2.6)$$

Resorting to Eq. (2.3), the electric field can be written as

$$\underline{E}(x,y,z) = \frac{1}{4\pi^2}\iint\limits_{\mathbb{R}^2} \underline{\hat{E}}(k_x,k_y)e^{-j\underline{k}\cdot\underline{r}}\,\mathrm{d}k_x\mathrm{d}k_y \quad (2.7)$$

where $\underline{k}\cdot\underline{r} = k_x x + k_y y + k_z z$, and $\underline{\hat{E}}$ is referred to as the Plane Wave Spectrum (PWS) of $\underline{E}$. Eq. (2.7) lets us express $\underline{E}$ for $z > 0$ as a superimposition of plane waves[2].

On the AP, Eq. (2.7) becomes

$$\underline{E}_a(x,y) = \frac{1}{4\pi^2} \iint\limits_{\mathbb{R}^2} \underline{\hat{E}}_t(k_x,k_y) e^{-j\left(k_x x + k_y y\right)} \, \mathrm{d}k_x \mathrm{d}k_y \tag{2.8}$$

where $\underline{\hat{E}}_t = \hat{E}_x \hat{i}_x + \hat{E}_y \hat{i}_y$. Eq. (2.8) relates the AF to the inverse Fourier Transform of $\underline{\hat{E}}_t$, thus obtaining:

$$\underline{\hat{E}}_t(k_x,k_y) = \iint\limits_{\mathbb{R}^2} \underline{E}_a(x,y) e^{j\left(k_x x + k_y y\right)} \, \mathrm{d}x \mathrm{d}y \tag{2.9}$$

The third component of $\underline{\hat{E}}$ can be written as:

$$\hat{E}_z = -\frac{k_x \hat{E}_x + k_y \hat{E}_y}{\sqrt{\beta^2 - k_x^2 - k_y^2}} \tag{2.10}$$

Eq. (2.9) and Eq. (2.10) allow us to obtain $\underline{\hat{E}}$ from the AF, and from Eq. (2.7), the unknown electric field. In the far field region ($r \to \infty$) the solution of Eq. (2.6), in spherical coordinates, is given by:

$$\underline{E}(\underline{r}) = \frac{j\beta e^{-j\beta r}}{2\pi r} \cos\theta \underline{\hat{E}}(\beta u, \beta v) \tag{2.11}$$

where $u = \sin\theta\cos\phi$ and $v = \sin\theta\sin\phi$ are the direction cosines. According to Eq. (2.11), the FFP can be defined as

$$\underline{\mathcal{F}}(u,v) = \cos\theta \underline{\hat{E}}(\beta u, \beta v) \tag{2.12}$$

Except for the $\cos\theta$ term, the FFP in Eq. (2.12) is defined as the PWS of $\underline{E}$, which is related to the AF by a Fourier Transform relationship.

2.2.2 Induced Currents Method

Referring to Fig. 2.2, the radiated electric field can be expressed as a function of the current $\underline{J}$ induced on the reflector surface Σ[24]:

$$\begin{cases} \underline{E}(\theta,\phi) = -\frac{j\beta\zeta}{4\pi\rho} e^{-j\beta\rho}\left[\underline{\underline{I}} - \hat{i}_r\hat{i}_r\right]\cdot\underline{\mathcal{F}}(\theta,\phi) \\ \underline{\mathcal{F}}(\theta,\phi) = \iint\limits_{\Sigma} \underline{J}(\underline{r}')e^{j\beta\hat{i}_r\cdot\underline{r}'}\,\mathrm{d}\Sigma' \end{cases} \tag{2.13}$$

where $\underline{\underline{I}}$ is the identity matrix. Employing a Physical Optics (PO) approximation[2], $\underline{J}$ can be obtained from the magnetic field $\underline{H}^i$ impinging from the feed:

$$\underline{J}(\underline{r}') = 2\,\hat{i}_n \times \underline{H}^i \tag{2.14}$$

$\hat{i}_n$ being the normal to Σ, and $\underline{H}^i$ the incident magnetic field. Alternatively, the integration in Eq. (2.13) can be expressed in terms of the reflector aperture A projected onto the plane $z = 0$:

$$\underline{\mathcal{F}}(\theta,\phi) = \iint\limits_{A} \underline{J}_A(\underline{r}')e^{j\beta z'\cos\theta}e^{j\beta\,\hat{i}_r\cdot\underline{r}'_A}\,\mathrm{d}A' \tag{2.15}$$

where $\underline{r}'_A = x'\,\hat{i}_x + y'\,\hat{i}_y$ and

$$\underline{J}_A(\underline{r}') = \sqrt{1 + (\frac{\partial g}{\partial x'})^2 + (\frac{\partial g}{\partial y'})^2}\,\underline{J}(\underline{r}') \tag{2.16}$$

In Eq. (2.16), $z = g(x, y)$ describes the reflector surface. In Cartesian coordinates, the unit vector $\hat{i}_r$ can be expressed as a function of the direction cosines u and v, so that Eq. (2.15) can be rewritten as:

$$\underline{\mathcal{F}}(\theta, \phi) = \iint_A \underline{J}_A(\underline{r}') e^{j\beta z' \cos\theta} e^{j\beta\left(ux' + vy'\right)}\, \mathrm{d}x' \mathrm{d}y' \tag{2.17}$$

Due to the $\cos\theta$ term, which is a function of (x, y), appearing in Eq. (2.17), $\underline{\mathcal{F}}$ is not a Fourier Transform of $\underline{J}_A$. In general, Eq. (2.17) can be represented as a series of Fourier Transforms[25]. However, it is possible to adopt a paraxial approximation, typically valid for reflectors sufficiently large in terms of wavelength and when the extent of the angular region wherein the data is required is small, and assuming $\cos\theta \simeq 1$:

$$\underline{\mathcal{F}}(\theta, \phi) = \iint_A \underline{J}_A(\underline{r}') e^{j\beta z'} e^{j\beta\left(ux' + vy'\right)}\, \mathrm{d}x' \mathrm{d}y' \tag{2.18}$$

2.3 Coherent Microwave Holography

The large dimensions of radio telescopes makes it difficult to measure the far field characteristics using ground based test ranges. Indeed, the conditions defining the far field region for an antenna with diameter D are the following

$$\begin{cases} r \gg D \\ r \gg \lambda \\ r \geq \frac{2D^2}{\lambda} \end{cases} \tag{2.19}$$

where λ is the wavelength. From Eq. (2.19) it can be easily seen that even for an antenna larger than a few hundreds of wavelengths the minimum distance could easily reach several Kms, a distance which is hardly covered by ground based transmitters. For this reason, radio astronomers have turned to natural extraterrestrial radio sources or artificial satellites radiating a beacon signal at a fixed frequency. In addition to the adequate distance, a cosmic source presents the additional advantage of a fixed celestial position, which means that it describes a well determined path across the sky as seen from the radio telescope. This provides a range of elevation angles over which the data can be collected, allowing for the study of elevation dependent deformations of the antenna, caused by gravity. However, only few strong radio sources can provide a sufficient signal to noise ratio. The measurement is more favorable when several large antennas are available, as in interferometric arrays, where the extra antennas can be used to provide a strong reference signal. An example is given by the IRAM 30 m millimeter telescope on Pico Veleta[26] which employed a holographic system at 22 GHz, using the very strong water vapour maser source in the Orion Nebula. The reference signal was provided by a 1.5 m diameter reflector located in the back of the prime-focus cage of the telescope. The

intensity of the radio source was sufficiently strong to enable a measurement of the surface with an accuracy of about 30 mm RMS and a setting of the surface to better than 100 mm RMS[27]. Artificial satellites, radiating a beacon signal at a fixed frequency can also be used as farfield signal sources. Extensive use has been made of synchronous communication satellites in the 11 GHz band[28]. Some satellites, notably the LES (Lincoln Experimental Satellite) 8 and 9, have been used for radio holography of millimeter telescopes[29], though both satellites are no longer available.

Coherent Microwave holography is based on the Induced currents Method introduced in Section 2.2.2, which relates the FFP to the reflector currents, allowing to obtain the phase error, and therefore the reflector distortions, from the measurement of the complex (i.e. in amplitude and phase) FFP. To measure the FFP in both amplitude and phase, usually a second antenna pointed at the same source is adopted to provide a stable phase reference. As an alternative, only the amplitude of the FFP can be used as input data[30]–[32]. More recently, microwave holography has been extended to allow data measured in the Fresnel region of the antenna[33]. Moreover, in [34] a regularized approach to the solution is presented, based on a Truncated Singular Value Decomposition (TSVD) to cope with the inherent ill-conditioning of the problem and increase the robustness of the diagnosis. Following the results presented in Section 2.2.2, the mathematical relationship between the antenna FFP $\underline{\mathcal{F}}$ and the surface induced current distribution $\underline{J}$ is given by Eq. (2.17).

A scalar problem can be set up by considering the co-polar component $\mathcal{F}_{co}$ of the FFP:

$$\mathcal{F}_{co}(u,v) = \hat{i}_c \cdot \iint_{\Sigma} \underline{J}(x,y) e^{j\beta z} e^{-j\beta z\left(1-\cos\theta\right)} e^{j\beta\left(ux+vy\right)} \,\mathrm{d}x\mathrm{d}y \tag{2.20}$$

where $\hat{i}_c$ identifies the co-polar direction according to Ludwig's third definition[35]:

$$\begin{aligned} &\hat{i}_c = \hat{i}_\theta \cos\phi - \hat{i}_\phi \sin\phi = \\ &= \left[1 - \cos^2\phi(1-\cos\theta)\right] \hat{i}_x - (1-\cos\theta)\sin\phi\,\cos\phi\,\hat{i}_y - \sin\theta\,\cos\phi\,\hat{i}_z \end{aligned} \tag{2.21}$$

In principle, both components of the FFP should be employed, however the co-polar component is preferable as it provides a better Signal to Noise Ratio (SNR) in actual measurements.

For large reflectors with respect to the wavelength and when the angular region of the required pattern data is small, it is possible to assume $\cos\theta \simeq 1$, obtaining[24]

$$\mathcal{F}_{co}(u,v) = \hat{i}_c \cdot \iint_{\Sigma} \underline{J}(x,y) e^{j\beta z} e^{j\beta\left(ux+vy\right)} \,\mathrm{d}x\mathrm{d}y \tag{2.22}$$

Eq. (2.22) represents a Fourier Transform of the induce surface current. Thanks to a Geometrical Optics (GO) approximation, the normal error ϵ

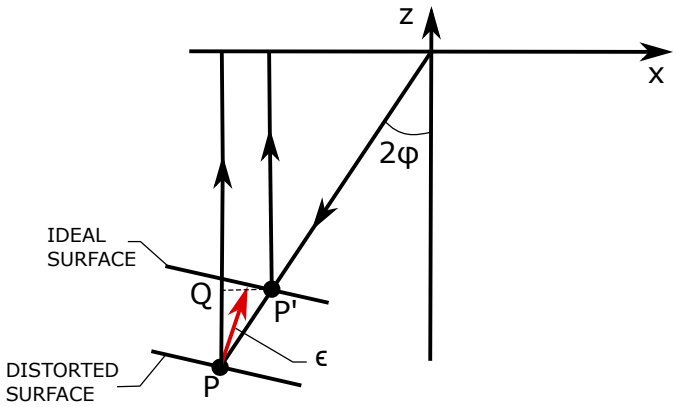

Figure 2.3. Surface distortion geometry.

can be related to the phase error. In particular, referring to Fig. 2.3, the path length variation Δ is given by:

$$\Delta = \overline{P'P} + \overline{PQ}\frac{\epsilon}{\cos\phi} + \frac{\epsilon\,\cos 2\phi}{\cos\phi} = 2\epsilon\,\cos\phi \tag{2.23}$$

corresponding to a phase variation $\Delta\varphi$

$$\Delta\varphi = 2\beta\,\epsilon\,\cos\phi \tag{2.24}$$

and

$$\cos\phi = \frac{1}{\sqrt{1+\frac{x^2+y^2}{4F^2}}} \tag{2.25}$$

Allowing for the removal of a constant phase term and substituting Eq.

(2.24) into Eq. (2.22) yields:

$$\mathcal{F}_{co}(u,v) = e^{-j2\beta F}\,\hat{i}_c \cdot \iint_{\Sigma} \underline{J}(x,y) e^{j4\pi\frac{\epsilon}{\lambda}\cos\phi} e^{j\beta\left(ux+vy\right)}\,\mathrm{d}x\mathrm{d}y \tag{2.26}$$

Solving for the normal surface error and substituting Eq. (2.25)

$$\epsilon(x,y) = \frac{\lambda}{4\pi}\sqrt{1+\frac{x^2+y^2}{4F^2}}\,Phase\left[e^{j2\beta F}\mathfrak{F}^{-1}\left\{\mathcal{F}_{co}(u,v)\right\}\right] \tag{2.27}$$

The numerical evaluation of Eq. (2.27) depends on the nature of the measured data. For instance, depending on the antenna drive mechanism, the FFP can be collected in a raster scan. In [36] a procedure is illustrated to properly control the motion of the antenna to allow the FFP to be sampled directly on a regular grid in the $u-v$ space. A Fast Fourier Transform (FFT) may be then employed to evaluate Eq. (2.27). Obviously, to correctly use the FFT, the sampling grid should be chosen according to the Nyquist sampling rate given by

$$\Delta u = \Delta v = \kappa\frac{\lambda}{D} \tag{2.28}$$

where κ is a factor to ensure the required sampling criterion. The corresponding spatial resolution can be derived from the properties of the FFT and are given by:

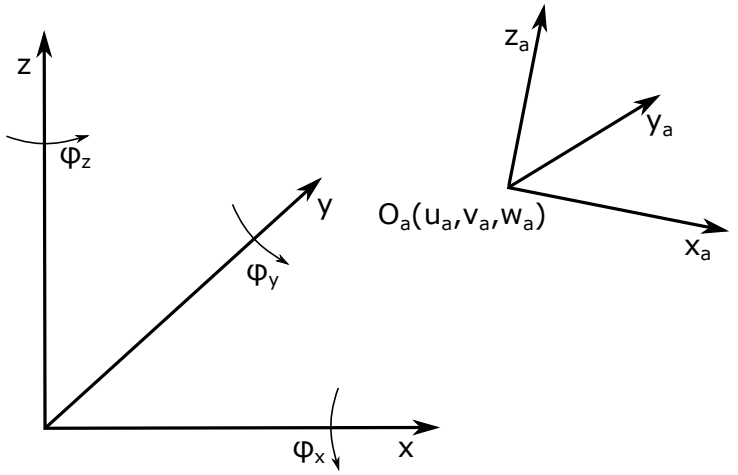

Figure 2.4. Initial and new coordinate system in parabolic best fitting.

$$\begin{cases} \Delta x = \frac{D}{\kappa(K-1)} = \frac{\lambda}{(K-1)\Delta u} \\ \Delta y = \frac{D}{\kappa(K-1)} = \frac{\lambda}{(K-1)\Delta v} \end{cases} \tag{2.29}$$

The approach illustrated so far represents the fundamental procedure to diagnose surface distortions from far-field measurements. A higher spatial resolution can be achieved by exploiting an iterative method based on alternating projections[37].

2.3.1 Paraboloid Surface Best Fitting

Before projecting the aperture phase function on the aberration modes to obtain the reflector surface error, a global least squares fit is performed to obtain the "best fit" paraboloid. The process allows to mitigate the

measurement errors and a correction of the antenna pointing. Considering the Cartesian reference system in Fig. 2.4, a paraboloidal surface satisfies the following equation:

$$z = z_0 + \frac{x^2 + y^2}{4F} \tag{2.30}$$

Accounting for three translations, three rotations φ_x, φ_y, φ_z about the x, y and z axis respectively and a change of the focal length ΔF, the best fit paraboloid will satisfy Eq. (2.30) in a new reference system $O_a(x_a, y_a, z_a)$ centered in (u_a, v_a, w_a) (Fig. 2.4):

$$z_a = z_0 + \frac{{x_a}^2 + {y_a}^2}{4F_a} \tag{2.31}$$

where $F_a = F + \Delta F$. The relationship between the initial and the new coordinate systems are:

$$\begin{cases} x_a = (x - u_a) - (z - z_0)\varphi_y \\ y_a = (y - v_a) - (z - z_0)\varphi_x \\ z_a = (z - w_a) + x\varphi_y - y\varphi_x \end{cases} \tag{2.32}$$

The best fit paraboloid surface in the initial coordinate system can be written, ignoring the higher order terms, as:

$$\begin{aligned} x^2 + y^2 + 2(z - z_0)y\varphi_x - 2(z - z_0)x\varphi_y + \\ -2x(u_a + 2F\varphi_y) - 2y(v_a + 2F\varphi_x) + \\ -4(z - z_0)\Delta F + 4Fw_a = 0 \end{aligned} \tag{2.33}$$

If the displacement of a generic point (x_i, y_i, z_i) is (u_i, v_i, w_i), the following equations hold for its distance Δ_i from the best fit surface:

$$\begin{cases} x_i(u_i - u_a) + y_i(v_i - v_a) + 2F(w_i - w_a) - 2(z_i - z_0)\Delta F + \\ \qquad + y_i(2F + z_i - z_0)\varphi_x - x_i(2F + z_i - z_0)\varphi_y = \\ \qquad = \pm \dfrac{\Delta_i}{2\sqrt{F(F + z_i - z_0)}}(x_i^2 + y_i^2 + 4F^2) \\ \Delta_i = \pm \dfrac{1}{2\sqrt{F(F + z_i - z_0)}} \left[x_i(u_i - u_a) + y_i(v_i - v_a) + 2F(w_i - w_a) + \right. \\ \qquad \left. -2(z_i - z_0)\Delta F + y_i(2F + z_i - z_0)\varphi_x - x_i(2F + z_i - z_0)\varphi_y \right] \end{cases} \tag{2.34}$$

The sum of all the N_a distances squared to the best fit paraboloid is:

$$G = \sum_{i=1}^{N_a} \Delta_i^2 \tag{2.35}$$

The best fit paraboloid is found by minimizing G with respect to the 6 degrees of freedom of the reflector motion, leading to 6 partial differential equations of the form:

$$\frac{\partial G}{\partial u_a} = \frac{\partial G}{\partial v_a} = \frac{\partial G}{\partial w_a} = \frac{\partial G}{\partial \varphi_x} = \frac{\partial G}{\partial \varphi_y} = \frac{\partial G}{\partial \Delta F} = 0 \tag{2.36}$$

The paraboloid best fit can be applied also to dual reflector or even shaped reflector systems since either design can be seen as a plane wave to point source transformer, differing only in the field aperture distribution[38]. It can also be used to fit the position of individual panels of a segmented reflector[39].

2.3.2 Reflector Shape Retrieval

Once the aperture phase distribution is known and fitted to the best paraboloid, the final step is the determination of the reflector shape. This can be achieved by applying a standard GO technique. Referring to Fig. 2.5, P represents a point on the reflector surface described by the position vector $\underline{\rho}$, and $\hat{q}$ is the direction of the reflected ray in P. If Q is the intersection of the reflected ray with the aperture plane, described by the position vector $\underline{p}$, by applying simple GO considerations we have

$$\begin{cases} \underline{\rho} = \underline{p} + \alpha \hat{q} \\ \left|\underline{p} - \underline{\rho}\right| + \left|\underline{\rho}\right| = L(Q) - L_0 \end{cases} \tag{2.37}$$

where L is the known optical path on the aperture and L_0 is an arbitrary chosen reference optical path. The first equation states that Q lies on the reflected ray described by the direction $\hat{q}$ while the second relates the

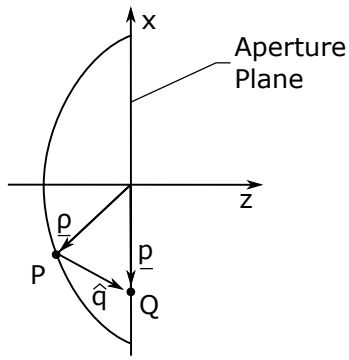

Figure 2.5. Geometry for the reflector surface retrieval. The ray reflected from a point P on the surface, described by the vector $\underline{\rho}$, intersects the aperture plane in the point Q, described by the vector $\underline{p}$. The versor $\hat{q}$ describes the direction of the reflected ray.

distance between the two points to the optical path. The only unknown in Eq. (2.37) is represented by α, which can be readily found by combining the two expressions, resulting in:

$$\alpha = \frac{1}{2} \frac{(L - L_0)^2 - \left\| \underline{p} \right\|^2}{L - L_0 + \underline{p} \cdot \hat{q}} \tag{2.38}$$

Summary of the State of the Art

For convenience, the main features of the diagnosis methods presented in this Chapter are briefly summarized in Table 2.1.

Method	**Advantages**	**Disadvantages**
Direct Methods (Theodolite and Tape, Photogrammetry)	Straightforward because based on well assessed technologies	• Poor surface accuracy (∼0.1 mm) • High maintenance time
Coherent Microwave Holography	• High Accuracy (<50 µm) • Reduced maintenance time	Requires a complex setup for the measurement in amplitude and phase
Amplitude only methods	• High Accuracy (<50 µm) • Reduced maintenance time • Simpler setup typically already available	Requires a higher SNR to achieve the same accuracy of the Coherent Holography

Table 2.1. Summary of the features of the State of the Art for Radio Telescopes diagnosis.

Chapter 3

Optimized approach to the reflector diagnosis

The electromagnetic diagnosis method presented in Chapter 2 require the acquisition of the complete FFP of the AUT, which can result a very large number of field samples, increasing the measurement time. A prolonged acquisition has significant drawbacks related to the continuous tracking of the source and the inconstancy of the environmental conditions. In the present Chapter, an optimized formulation of the diagnosis of radio telescopes is presented, aimed at reducing the number of field samples to acquire, and so at minimizing the measurement time. The developed diagnosis approach is based on the Aperture Field method for the description of the AUT radiation mechanism. In Section 3.2.2, a Principal Component

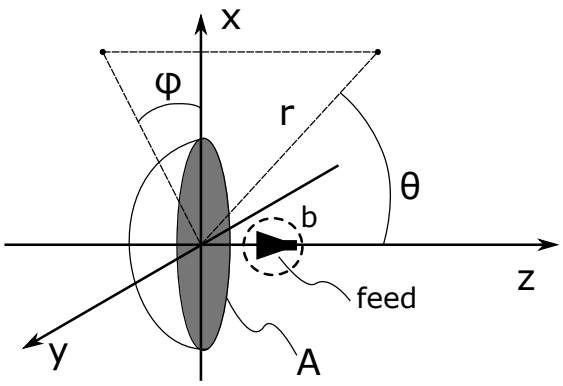

Figure 3.1. Geometry of the reflector antenna aperture.

Analysis (PCA) is adopted to restore a linear relationship between the unknowns describing the AUT status and the far field data. In Section 3.3, an optimal far field sampling grid is selected by optimizing the singular values behavior of the relevant linearized operator.

3.1 Introduction

In this Section, the mathematical model of the optimized diagnosis is presented. A slightly different model is adopted, based on the AF method instead of the induced current method, as done in Section 2.3 for the Microwave Holography. Let us consider a reflector antenna whose aperture A lies in the $z = 0$ plane of an $Oxyz$ reference system (Fig. 3.1). According to the AFM presented in Section 2.2.1 and here briefly reported for convenience, the electric field radiated in the far-field region can be written as:

$$\underline{E}(r,\theta,\phi) = \frac{j\beta e^{j\beta r}}{2\pi r}\underline{\mathcal{F}}(\beta\,\sin\theta\,\cos\phi, \beta\,\sin\theta\,\cos\phi) \tag{3.1}$$

where the FFP $\underline{\mathcal{F}}$ is defined as:

$$\underline{\mathcal{F}}(\beta u, \beta v) = \cos\theta \iint_A \underline{E}_a(x,y) e^{j\beta\left(ux+vy\right)}\,\mathrm{d}x\mathrm{d}y \tag{3.2}$$

where $u = \sin\theta\cos\phi$ e $v = \sin\theta\sin\phi$ are the direction cosines while $\underline{E}_a$ represents the AF.

As with the approach developed in Section 2.3, we may refer to a scalar problem by considering the co-polar component $\mathcal{F}_{co}$ of the FFP:

$$\mathcal{F}_{co}(\beta u, \beta v) = \hat{i}_c \cdot \cos\theta \iint_A \underline{E}_a(x,y) e^{j\beta\left(ux+vy\right)}\,\mathrm{d}x\mathrm{d}y \tag{3.3}$$

where $\hat{i}_c$ was defined in Eq. (2.21).

Eq. (3.3) shows that the FFP relates to the AF again through a Fourier Transform linear relationship and can be formally written as:

$$\mathcal{F}_{co} = \mathcal{T}\left[E_a\right] \tag{3.4}$$

where E_a represent the AF component corresponding to the co-polar component of the FFP. Let us now consider the influence of misalignments and of the reflector shape on E_a. Since we are interested in dealing with an AUT whose dimensions are large with respect to the wavelength, a key relationship can be obtained by applying the GO approximation for

the evaluation of the aperture field[40], [41]. In particular, the AF can be factorized as

$$E_a(x,y) = E_{a0}(x,y)e^{j\Phi\left(x,y;p_1,p_2,\ldots,p_N\right)} \tag{3.5}$$

where $E_{a0}(x,y)$ represent a nominal AF, while $\Phi(x,y;p_1,p_2,\ldots,p_N)$ represents a real aberration function describing the phase perturbation as a function of N parameters $\{p_n\}_{n=1}^{N}$ defining the status of the AUT. Obviously, both E_{a0} and Φ depends on the AUT configuration. However, while the phase perturbation $e^{j\Phi}$ is very sensitive to any distortion, the relative variations of E_{a0} are of the order of $\frac{\gamma\left(1+\beta b\right)}{d}$, γ being the RMS of the distortion and b the primary source radius (Fig. 3.1). Therefore, E_{a0} turns out to be essentially independent of the AUT status, as long as the deviation of the AUT from its nominal configuration is small compared to the reflector size. This observation allows to assume that E_{a0} is known *a priori* and corresponds to the AF of the AUT in its undistorted condition. Therefore, the AUT status affects only the phase distribution of E_a. Accordingly, the FFP can be expressed as

$$\mathcal{F}_{co} = \mathcal{T}\left[E_{a0}(x,y)e^{j\Phi\left(x,y;p_1,p_2,\ldots,p_N\right)}\right] \tag{3.6}$$

With these assumptions, the diagnosis problem has been recast as a linear inverse problem, and it amounts first at finding the aberration function Φ from the knowledge of the FFP $\mathcal{F}$, and then the parameters $\{p_n\}_{n=1}^{N}$ describing its status.

Let us consider the antenna as a system whose input is the (unknown) aberration function Φ and whose output is the FFP $\mathcal{F}_{co}$. Φ and $\mathcal{F}_{co}$ can be assumed to belong to two Hilbert spaces of square-integrable functions **S** and **H**, respectively. The elements of **S** have support A, while the elements of **H** are band-limited function whose support is the visible region of the u-v plane, denoted as Ω.

The relationship between the AF and the FFP, after an appropriate change of variables, can be examined in terms of the eigenfunctions χ of Eq. (3.4) by considering the following equation:

$$\mathcal{T}\left[\chi_n\right] = \lambda_n \chi_n \tag{3.7}$$

where the coefficients λ_n are the eigenvalues of $\mathcal{T}$. Since the kernel of the equation is positive definite[42], Eq. (3.7) has a complete set of orthogonal eigenfunctions corresponding to a countable infinite set of real positive eigenvalues. Due to the completeness of the set, the field can be expanded as:

$$E_a = \sum_{n=0}^{\infty} a_n \chi_n \tag{3.8}$$

where

$$a_n = \iint_A E_a \chi_n^* \, \mathrm{d}x\mathrm{d}y \tag{3.9}$$

By substituting Eq. (3.8) in Eq. (3.4) and resorting to the Mercer theorem[43] to expand the Fourier Transform kernel, we obtain:

$$\mathcal{T}\left[E_a\right] = \sum_{n=0}^{\infty} \lambda_n a_n \chi_n \tag{3.10}$$

Eq. (3.10) shows that all the degrees of freedom of the field are retained, and the effect of the operator $\mathcal{T}$is to multiply the each coefficient a_n by the corresponding eigenvalue λ_n. As a general property of the eigenvalues of integral equations of the same kind of Eq. (3.7), λ_n tend to zero with increasing n[44]. Thus, in presence of noise, very small eigenvalues involve the loss of information associated with the corresponding eigenfunction. In [45]–[47] is shown that the eigenvalues sequence has a step like behavior, i.e. it assumes relatively high values until a critical value $n = n_{crit}$ is reached, after which, for $n > n_{crit}$, the eigenvalues decay very rapidly. In [46], it is shown that the sum of the eigenvalues is equal to the Shannon number, and can be then assumed as a measure of the number of significant degrees of freedom of the system[48].

3.2 Selection of basis functions for the Aperture Field expansion

3.2.1 Karhunen–Loève theorem

Let us consider a square-integrable function f defined over a compact interval X, with a continuous covariance function K_f:

$$K_f : X \times X \to \mathbb{R} \tag{3.11}$$

K_f is symmetric, i.e. $K_f(\mathbf{s},\mathbf{t}) = K_f(\mathbf{t},\mathbf{s})$, $\mathbf{s},\mathbf{t} \in X$. K_f is also non-negative definite[49]:

$$\sum_{i=1}^{N}\sum_{j=1}^{N} c_i c_j K_f(\mathbf{s}_i,\mathbf{s}_j) \geq 0, \quad \forall \{c_i\}_{i=1}^{N} \in \mathbb{R}, \forall \{\mathbf{s}_i\}_{i=1}^{N} \in X \tag{3.12}$$

A linear operator $\mathfrak{T}$ can be associated to K_f, defined as:

$$\mathfrak{T} : f \in L^2(X) \mapsto \mathfrak{T}[f] = \int_X K_f(\mathbf{s},\cdot) f(\mathbf{s})\, \mathrm{d}\mathbf{s} \in L^2(X) \tag{3.13}$$

Mercer's theorem[43] guarantees that there is an orthonormal basis $\{\psi_i\}_{i=1}^{N_\psi}$ of $L^2(X)$ consisting of eigenfunctions of $\mathfrak{T}$, such that the corresponding sequence of eigenvalues $\{\lambda_i\}_{i=1}^{N_\psi}$ is non-negative. The eigenfunctions corresponding to non-zero eigenvalues are continuous on X, and K_f can

be represented as:

$$K_f(\mathbf{s},\mathbf{t}) = \sum_{j=1}^{\infty} \lambda_j \psi_j(\mathbf{s}) \psi_j(\mathbf{t}) \tag{3.14}$$

Following this result, f admits the following representation:

$$f(\mathbf{s}) = \sum_{k=1}^{\infty} a_k \psi(\mathbf{s}) \tag{3.15}$$

which converges uniformly in L^2, and

$$a_k = \int_X f(\mathbf{s}) \psi(\mathbf{s}) \, \mathrm{d}\mathbf{s} \tag{3.16}$$

The convergence can be proven by considering the partial sum S_N defined as

$$S_N = \sum_{k=1}^{N} a_k \psi(\mathbf{s}) \tag{3.17}$$

Then

$$
\begin{aligned}
&\|f - S_N\|^2 = \\
&= K_f(\mathbf{s},\mathbf{s}) + \int_X \sum_{k=1}^{N}\sum_{l=1}^{N} a_k a_l \psi_k(\mathbf{s})\psi_l(\mathbf{s})\,\mathrm{d}\mathbf{s} - 2\int_X f(\mathbf{s})\sum_{k=1}^{N} a_k\psi(\mathbf{s})\,\mathrm{d}\mathbf{s} = \\
&= K_f(\mathbf{s},\mathbf{s}) + \sum_{k=1}^{N}\lambda_k\psi_k(\mathbf{s})^2 - 2\int_X \sum_{k=1}^{N}\int_X f(\mathbf{s})f(\mathbf{t})\psi_k(\mathbf{s})\psi_k(\mathbf{t})\,\mathrm{d}\mathbf{s}\,\mathrm{d}\mathbf{t} = \\
&= K_f(\mathbf{s},\mathbf{s}) - \sum_{k=1}^{N}\lambda_k\psi_k(\mathbf{s})^2
\end{aligned}
\tag{3.18}
$$

which goes to 0 for $N \to \infty$ by Mercer's theorem. The Karhunen–Loève's theorem allows us to represent a function f as an infinite linear combination of orthogonal functions ψ. The basis functions set provided depends on the function itself, as is determined by the covariance function of f. Such representation is optimal in the sense that it minimizes the total mean squared error.

3.2.2 Principal Component Analysis of the Aperture Field

In order to restore a linear relationship between the unknowns and the FFP in Eq. (3.4), it is useful to consider the mathematical operator mapping a set of parameters $\{p_n\}_{n=1}^{N}$ to the complex valued perturbed AF. Let us consider all the possible parameters necessary to describe the AUT status. In practice, $\underline{p} = (p_1, p_2, \ldots, p_N)$ may be varied in a limited

interval defining the acceptable indeterminacy and thus belongs to a set $\mathcal{P} \subset \mathbb{R}^N$. Therefore, all the allowed perturbed E_a belong to a manifold $\mathcal{M}$ in the space of the functions of two variables (x, y). For each $\underline{p} \in \mathcal{P}$, the corresponding E_a is obtained through the mapping:

$$\mathcal{A} : \mathcal{P} \rightarrow \mathcal{M} \tag{3.19}$$

Since the degrees of freedom of the AUT distortions is physically limited and assumed to be small, we suppose that $\mathcal{M}$ may be approximated by a suitable K-dimensional vector subspace $\mathcal{K}$. E_a may be then approximated though the expansion

$$E_a(x, y; \underline{p}) = E_{a0}(x, y) e^{j\Phi\left(x,y;\underline{p}\right)} = \sum_{k=1}^{K} c_k(\underline{p}) \psi_k(x, y) \tag{3.20}$$

where $\{\psi_k\}_{k=1}^K$ represents a set of basis functions for $\mathcal{K}$ and $\{c_k\}_{k=1}^K$ contains the unknown expansion coefficients. Since $\mathcal{A}$ is non linear, a higher dimension space $\mathcal{K}$ is needed in principle to guarantee an accurate approximation, i.e. K > N. In order to reduce as much as possible the number of unknowns, the smallest subspace containing $\mathcal{M}$ should be selected. To this end, a relevant set of perturbation parameters $\underline{p}$ and their corresponding perturbations are considered according to the knowledge of expected configurations of the AUT and to the desired monitoring resolution. For instance, the diagnosis could be aimed at the description of a

feed misalignment. N_r of different realizations of E_a may be then obtained by considering different feed positions to provide a discretization for $\mathcal{M}$. Obviously, given a maximum displacement, a sufficient number of intermediate positions are required. To select the smallest $\mathcal{K}$ containing $\mathcal{M}$, a Principal Component Analysis (PCA)[50] is exploited. Let us define the matrix $\underline{\underline{E}}_a$ as

$$\underline{\underline{E}}_a = \begin{bmatrix} \underline{E}_{a1} & \underline{E}_{a2} & \dots & \underline{E}_{aN_r} \end{bmatrix} \tag{3.21}$$

where $\underline{E}_{ak}$ are M_r sized column vectors each representing a different realization corresponding to a different feed position. To choose the optimal set of basis functions, we may consider the Singular Value Decomposition (SVD) of $\underline{\underline{E}}_a$[51]:

$$\underline{\underline{E}}_a = \underline{\underline{U}}\,\underline{\underline{\Sigma}}\,\underline{\underline{V}} \tag{3.22}$$

where $\underline{\underline{U}} \in \mathbb{C}^{M_r \times M_r}$ and $\underline{\underline{V}} \in \mathbb{C}^{N_r \times N_r}$ are unitary matrices representing the left singular vectors and the right singular vectors, respectively, while $\underline{\underline{\Sigma}}$ is the diagonal matrix of the singular values of $\underline{\underline{E}}_a$.

According to the properties of the SVD, the columns of the matrix $\underline{\underline{U}}$ form an orthonormal basis for the column space of $\underline{\underline{E}}_a$, that is the vector space $\mathcal{K}$. Moreover, by noting that each singular value σ_k provides a measure of the information content of the corresponding ψ_k, it is possible, for a desired tolerance τ dependent on the desired degree of accuracy of the approximation, to retain only the first $\overline{K}$ basis functions such that

$\frac{\sigma_k}{\sigma_1} > \tau$, σ_1 being the first singular value.

3.3 Optimized sampling distribution

Having restored a linear relationship between the unknowns and the data, we can discretize Eq. (3.4). In particular, it is assumed that the FFP is sampled at S points (u_s, v_s). Eq. (3.4) can be then written in matrix form as:

$$\underline{F} = \underline{\underline{T}}\,\underline{C} \tag{3.23}$$

where $\underline{F}$ and $\underline{C}$ are the S-dimensional samples vector and the $\overline{K}$-dimensional vector of the expansion coefficients, respectively. The matrix $\underline{\underline{T}}$ represents the discretized version of the operator $\mathcal{T}$ and its entries are given by:

$$T_{sk} = \langle \mathcal{T}[\psi_k], \delta(u - u_s)\delta(v - v_s) \rangle \tag{3.24}$$

δ being the Dirac distribution.

To retrieve the coefficients c_k describing the AUT status, the inversion of the linear system Eq. (3.23) is required. Obviously the system can be affected by the ill-conditioning of $\underline{\underline{T}}$ with detrimental effects on the accuracy of the diagnosis and of its robustness against noise. Therefore a proper strategy is required to select the most convenient matrix before inverting. A plane-polar distribution of the samples is considered (Fig.

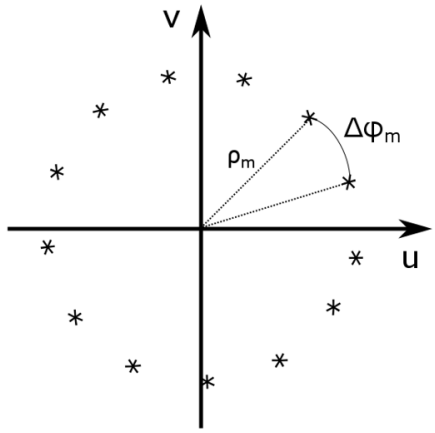

Figure 3.2. Geometry of the plane polar grid.

3.2), in which the samples are arranged on M rings with radii ρ_m, and therein uniformly spaced with step $\Delta\varphi_m$[52]. By means of a Singular Value Optimization (SVO), the most convenient M, ρ_m and $\Delta\varphi_m$, associated to the best conditioned $\underline{\underline{T}}$, can be selected. To this end, we observe that the matrix $\underline{\underline{T}}$ is not univocally defined, because it depends on the choice of M and the sample distribution over the grid. Accordingly, a set of different $\underline{\underline{T}}$ is available, with different singular values behaviour. This degree of freedom can be exploited to select the most convenient matrix corresponding to the best conditioning of the problem. Hence, for a fixed M, it is convenient to choose the samples distribution providing the "flattest" singular value behavior. This is achieved by the optimization of the functional[53]:

$$\begin{cases} \max & \Psi(\underline{\rho}, \underline{\Delta\varphi}) = \sum_{r=1}^{R} \dfrac{\sigma_r(\underline{\rho}, \underline{\Delta\varphi})}{\sigma_1(\underline{\rho}, \underline{\Delta\varphi})} \\ \text{subject to} & \sigma_1 > \sigma_{min} \end{cases} \tag{3.25}$$

where $\{\sigma_r\}_{r=1}^{R}$ are the singular values of $\underline{\underline{T}}$ in a decreasing order, and $R = min\left\{S, \overline{K}\right\}$. Ψ can be interpreted as the generalized Shannon number[48], [54], which is associated to the amount of information that can be gained from the field samples.

Concerning the choice of the optimal M, an iterative procedure is employed. Let us indicate as $\Psi_{opt}(M)$ the optimal value for the functional in Eq. (3.23) for a fixed M. By increasing M, a corresponding increase in $\Psi_{opt}(M)$ is expected, as more information is gathered from the measurement, until all the available information has been gathered. Therefore, beyond a certain threshold, an increase in M will introduce very small singular values, corresponding to a saturation of $\Psi_{opt}(M)$ (Fig. 3.3). Based on this observation, the optimal number M is chosen as the one corresponding to the saturation, which represents the minimum number of samples needed to recover all the information available.

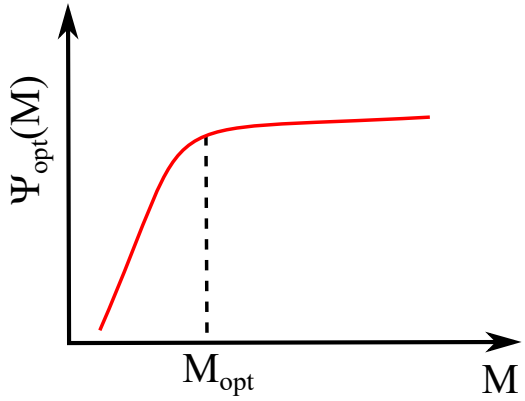

Figure 3.3. The optimal value of Ψ as a function of M.

Chapter 4

Fast Marching Method

In applications that involve the numerical solution of Maxwell's equation for electrically large scatterers, such as radio telescopes, asymptotic approaches based on GO would prove more feasible, compared to full-wave solutions provided, for example, by the Method of Moments (MoM). One common approach to construct the GO solution is ray tracing, allowing well assessed and fast algorithms such as Shooting and Bouncing Rays (SBR)[55]. Ray tracing consists of two main steps, namely the search for the intersection between a ray and the primitives describing the scatterer's geometry (i.e. triangles), and the electromagnetic field transport. While ray tracing can be convenient when dealing with homogeneous objects, it can be non-trivial for complex scenarios with electromagnetically penetrable scatterers having cumbersome spatially varying refraction index distributions. A GO tool able to accurately manage the propagation in in-

homogeneous media could help in predicting the effects of the atmosphere on the AP phase distribution[56], [57], in conjunction with a statistical model of the atmospheric turbulence[58]. In these cases, eulerian optics methods[59] based on the direct numerical solution to the eikonal equation are particularly appealing.
In this Chapter, an approach of this kind is presented, consisting of the following steps[60]:

1. quick and stable solution of the eikonal equation associated to the GO field;

2. inverse tracing of the rays;

3. solution of the electromagnetic field transport equations.

In the first step, detailed in Section 4.2, the eikonal equation in general inhomogeneous media is accurately, stably and quickly solved by the FMM[61]. The FMM is particularly appealing because it enables the use of inverse ray tracing and allows to reduce the N^4 computational complexity of "brute-force" approaches[62] to $O(N^3 \log N)$, $N \times N \times N$ being the discretization of the computational domain for a 3D problem. Moreover, the means to manage non homogeneous refractive index distributions would allow in principle to adopt more general models to describe the AUT, to include for instance effects related to the atmospheric refraction. In the second stage, presented in Section 4.3.2, the inverse ray tracing is performed

by using a technique introduced in computer graphics for the accurate and fast generation of textured images from vector fields[63]. In the third stage, presented in Section 4.1.1, the transport equation is solved by resorting only to its integral form. In Section 4.3 the parallel implementation of the method on Graphics Processing Unit (GPU) platforms is presented. In both standard ray tracing and eulerian approaches, the computation of ray intersecions between multiple scatterers to properly take into account mutual interactions is the most time consuming one, if not properly managed. For standard ray tracing, the issue can be successfully faced by resorting to space partitioning tree data structure such as the kD-tree[64] and BVH[65], [66]. In Section 4.3.3, a similar solution is introduced for the approach based on the FMM.

4.1 Geometrical Optics fundamental Equations

In this section, the fundamental equations to model the electromagnetic field under GO approximation are derived.
Let us consider Maxwell's equations in a linear, isotropic, non-dispersive medium:

$$\begin{aligned} \nabla \times \underline{E} &= -j\omega\mu\underline{H} \\ \nabla \times \underline{H} &= j\omega\epsilon\underline{E} \end{aligned} \tag{4.1}$$

where ϵ and μ are the permittivity and the permeability of the medium, respectively.

The GO approximation is based on plane wave like solutions[10]:

$$\begin{aligned} \underline{E}(x,y,z) &= \underline{E}_0(x,y,z)e^{-j\beta_0 L\left(x,y,z\right)} \\ \underline{H}(x,y,z) &= \underline{H}_0(x,y,z)e^{-j\beta_0 L\left(x,y,z\right)} \end{aligned} \tag{4.2}$$

where β_0 is the propagation constant of vacuum, $\underline{E}_0$ and $\underline{H}_0$ represent the plane waves *amplitudes*, while the function L in Eq. (4.2) is known as the *eikonal equation* and represents the phase distribution of the field. Maxwell's equations 4.1, as the frequency ω approaches ∞, reduce to:

$$\begin{aligned} \nabla L \times \underline{E}_0 - c\mu\underline{H}_0 = 0 \\ \nabla L \times \underline{H}_0 + c\epsilon\underline{E}_0 = 0 \end{aligned} \tag{4.3}$$

Eqs. (4.3) represent a homogeneous linear system. To ensure the existence of non trivial solutions, it is necessary to enforce that the determinant of the corresponding coefficient matrix is equal to zero:

$$|\nabla L|^2 = \left(\frac{\partial L}{\partial x}\right)^2 + \left(\frac{\partial L}{\partial y}\right)^2 + \left(\frac{\partial L}{\partial z}\right)^2 = n^2 \tag{4.4}$$

where $n = \sqrt{\frac{\mu\epsilon}{\mu_0\epsilon_0}}$ is the medium refractive index.

Eq. (4.10) can be solved with the method of characteristics[67], resulting in the well-known light ray equation:

$$\frac{d}{ds}\left(n\frac{d}{ds}(\underline{r})\right) = \nabla n \tag{4.5}$$

s being the path length of the ray.

4.1.1 Transport Equations

Having traced the rays, the last step to a complete solution of the electric field is finding the complex amplitude E_0. To this end, the transport equations for the field intensity and polarization must be solved[10]. The transport equation for the intensity I is:

$$\underline{\nabla} L(x,y,z) \cdot \underline{\nabla}\left[\frac{I(x,y,z)}{n(x,y,z)}\right] + \frac{I(x,y,z)}{n(x,y,z)}\nabla^2 L(x,y,z) \tag{4.6}$$

where $I = \frac{|\underline{E}_0(x,y,z)|^2}{2\zeta(x,y,z)}$, ζ begin the characteristic impedance of the medium and I_0 the initial condition given to I.

Eq. (4.6) is more easily solved by resorting to its integral form:

$$I(s) = n(s)e^{-\int \nabla^2 L(s')\,\mathrm{d}s'} \tag{4.7}$$

where the integral is to be performed along a ray.

Eq. (4.7) allows to obtain the intensity I_1 in a point P_1 from the knowledge of the intensity I_0 in another point P_0 on the same ray, namely

$$I_1 = I_0 \frac{n_1}{n_0} e^{-\int_{s_0}^{s_1} \frac{\nabla^2 L}{n}\, ds} \tag{4.8}$$

with $n_1 = n|_{P_1}$ e $n_0 = n|_{P_0}$.

The field polarization is described by the complex unit vector $\underline{e} = \frac{\underline{E}_0(x,y,z)}{|\underline{E}_0(x,y,z)|}$.

The corresponding transport equation is:

$$n(s)\frac{d}{ds}(\underline{e}(s)) + (\underline{e}(s) \cdot \underline{\nabla} n(s))\underline{\nabla} L(s) = 0 \tag{4.9}$$

Eq. (4.6), in its integral form, and Eq. (4.9) can be integrated after the rays have been determined.

4.2 Solution to the eikonal equation

The FMM represent a technique for the numerical solution to the eikonal equation introduced in Section 4.1:

$$\begin{cases} |\nabla L(x,y,z)| = n(x,y,z) & \text{in } \Omega \\ L(x,y,z) = L_0(x,y,z) & \text{on } \Sigma \end{cases} \tag{4.10}$$

where Ω is a closed volume in $\mathbb{R}^3$ wherein determining the solution, Σ is a surface on which the initial condition L_0 is given to L, and $n(x,y,z) > 0$ represents the refractive index.

Eq. (4.10) is a non-linear first order Partial Differential Equation (PDE). The information provided with the initial conditions propagates along cur-

ves, which are the light rays. The contour lines of the solution represent the wavefronts. Solving Eq. (4.10) is non trivial, because the solution can be non differentiable, even with continuous initial conditions[61]. This is the case, for instance, of self intersecting wavefronts where the solution becomes multi-valued, which can occur around caustics, where the GO approximation is known to fail. The ambiguity given by the multivaluedness of the eikonal is resolved by solving Eq. (4.10) for the *viscosity solution*[68]. This kind of solution is also referred to as the *first arrival* solution, because it resolves the ambiguity among different possible values by choosing the smallest one. The FMM manages the non differentiability by adopting an *upwind* discretization scheme. The upwind schemes have the fundamental property of being monotone, which guarantee a stable convergence of the numerical solution[68]. Furthermore, it achieves a favorable computational complexity by exploiting the causality property of the solution, combined with fast sorting algorithms.

4.2.1 Numerical discretization

Concerning the discretization of the computational domain, let us introduce a Cartesian numerical grid $(x_i, y_j, z_k) = (i, j, k)h$ on Ω, h being the discretization step. Let us define L_{ijk} as the value of L at the computational point (x_i, y_j, z_k), and $n_{ijk} = n(x_i, y_j, z_k)$ as the discrete values of the refractive index. As mentioned, to ensure the stability of the solution, Eq. (4.10) is discretized by a Godunov's upwind finite difference scheme

as:

$$\begin{aligned} &\left[(L_{ijk} - L_{xmin})^{+}\right]^2 + \\ &+ \left[(L_{ijk} - L_{ymin})^{+}\right]^2 + \\ &+ \left[(L_{ijk} - L_{zmin})^{+}\right]^2 = {n_{ijk}}^2 h^2 \end{aligned} \tag{4.11}$$

where

$$\begin{aligned} L_{xmin} &= min\left\{L_{i\text{-}1,j,k}, L_{i+1,j,k}\right\} \\ L_{ymin} &= min\left\{L_{i,j\text{-}1,k}, L_{i,j+1,k}\right\} \\ L_{zmin} &= min\left\{L_{i,j,k\text{-}1}, L_{i,j,k+1}\right\} \\ (x)^{+} &= \begin{cases} 0 & \text{per } x < 0 \\ x & \text{per } x \geq 0 \end{cases} \end{aligned} \tag{4.12}$$

Eq. (4.11) represents a quadratic equation in the unknown L_{ijk} given its six neighbours arranged in a three dimensional stencil, as shown in Fig. 4.1. By applying Eq. (4.11) to each node of the computational domain, a system of N^3 non linear equations is obtained, where N is the number of nodes along each spatial direction. A first approach to the solution of this system was proposed in [62] and summarized in Algorithm 1. Accordingly, the computational domain is traversed sequentially and the solution L updated at each node. The update is then repeated in an iterative procedure until convergence is reached in every node. Assuming that N steps are necessary for the iteration to converge, the computational complexity of

the algorithm is proportional to N^4. A more efficient solution is given by the FMM.

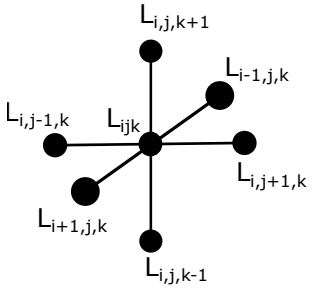

Figure 4.1. Three-dimensional stencil.

Algorithm 1: Rouy-Tourin "brute-force" algorithm

for $iter = 1 \rightarrow N$ **do**
  for $k = 1 \rightarrow N$ **do**
    for $j = 1 \rightarrow N$ **do**
      for $i = 1 \rightarrow N$ **do**
        $L_{ijk} \leftarrow$ solution to Eq. (4.11);

4.2.2 The Fast Marching Method algorithm

The FMM exploits the "causality" relation suggested by the analytic properties of the eikonal equation[61]. In particular, the solution is constructed starting from the region where the initial conditions are assigned and moving throughout the computational domain. Indeed, the information appears to propagate in a well defined direction, i.e. from lower values

to higher values of L. This observation allows us to define, at the first step of the algorithm, a set of nodes surrounding Σ, where the solution can be properly updated. The starting set of nodes form a discretized representation of the propagating wavefront, denotes as the *narrowband*. The nodes within the narrowband are the only ones considered by the update formula. Every other node in the domain is said to be *downwind* and is ignored until included in the narrowband. Since the solution can only be constructed through increasing values of L, the node within the narrowband corresponding to the minimum value of L cannot be influenced by any other node. This node is denoted as *trial* and removed from the narrowband, which is advanced by including the close neighbors of trial. A new trial node is then selected from the updated narrowband and the algorithm continues until all the nodes of the computational domain have been traversed. To obtain an efficient algorithm, it is essential to readily select the trial node. To this end, the narrowband is arranged as a min-heap data structure. The ordering property of the heap guarantees that the node corresponding to the smallest value of L is always at its root. The computational cost to insert a new element into a heap is $O(logM)$, where M is the number of element in the list[69]. Since each node must be updated only once, the overall computational cost of the FMM is $O(N^3 logN)$, instead of the $O(N^4)$ of the approach of [62]. The steps of the FMM are summarized in Algorithm 2.

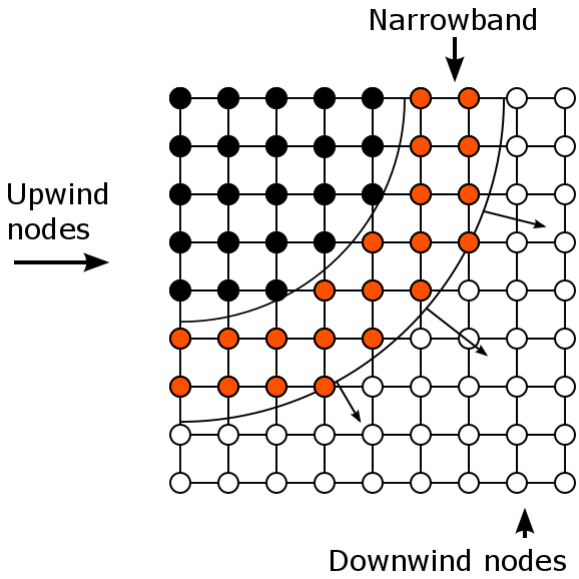

Figure 4.2. Illustrating the narrowband and the upwind and downwind nodes for the FMM.

Algorithm 2: Fast Marching Algorithm

```
"NB" narrowband;
"Set" updated nodes;
while NB ≠ ∅ do
    Trial ← heap root;
    Remove Trial from NB;
    Add Trial to Set;
    foreach node neighboring Trial do
        if node ∉ Set then
            node ← solution to Eq. (4.11);
            Add node to NB;
```

4.2.3 Discretization of Σ for the initialization of the FMM

Since Σ in general does not match the computational Cartesian grid, its discretization is necessary to connect the initial conditions given to L and to initialize the FMM. This issue is critical since any error in the initialization would impair the solution in the whole domain due to the error propagation effects related to the downstream expansion of the wavefronts[70]. A possible solution for a 2D geometry is shown in [71]. Accordingly, a triangular mesh is constructed as a backing grid considering only the nodes surrounding Σ and then employing a FMM for triangulated domains[61]. Unfortunately, extending this approach to a 3D geometry is a non-trivial

task, especially if a higher order discretization of the eikonal is needed. It should be further noted that the approach can be unfavorable also from a computational point of view due to the lower performance of the FMM for triangulated domains and to the additional burden of generating a triangular mesh. Moreover, the irregular nature of the triangulation hinders the possibility of a parallel implementation of the FMM.

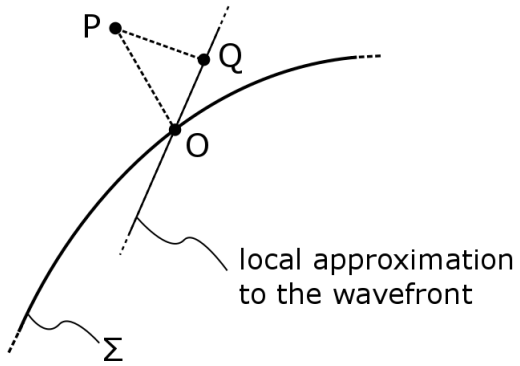

Figure 4.3. Matching Σ to the Cartesian computational grid by a local linear approximation to the wavefront.

The alternative hereby developed does not require neither a backing grid nor the FMM for triangular meshes. Conversely, the matching is performed by a local approximation of the reflected wavefront, dealing with each node independently. In particular, referring to Fig. 4.3, let us consider a node P of the Cartesian domain located in the neighborhood of Σ and let us consider the problem of obtaining the reflected eikonal L_s, given the incident one L_i. Due to the phase match condition, we can write:

$$L_s = L_i \qquad \text{on } \Sigma \tag{4.13}$$

Furthermore, Snell's law allows us to evaluate also ∇L_s on Σ. From the knowledge of both L_s and ∇L_s, a first order approximation to the reflected wavefront can be constructed. If the medium can be locally assumed as homogeneous, the reflected wavefront is planar and L_s can be written as:

$$L_s(P) = L_s(O) + n(Q)\overline{PQ} \tag{4.14}$$

where O is the normal projection of P on Σ, and Q is the projection of P onto the wavefront through O. For Eq. (4.14) to be valid, it is crucial to verify that the approximations employed are indeed valid. To this end, the wavefront curvature must be estimated by considering the norm of its hessian matrix:

$$H_s = \begin{bmatrix} \frac{\partial L_s}{\partial x^2} & \frac{\partial L_s}{\partial x \partial y} & \frac{\partial L_s}{\partial x \partial z} \\ \frac{\partial L_s}{\partial y \partial x} & \frac{\partial L_s}{\partial y^2} & \frac{\partial L_s}{\partial y \partial z} \\ \frac{\partial L_s}{\partial z \partial x} & \frac{\partial L_s}{\partial z \partial y} & \frac{\partial L_s}{\partial z^2} \end{bmatrix} = \begin{bmatrix} L_{xx} & L_{xy} & L_{xz} \\ L_{yx} & L_{yy} & L_{yz} \\ L_{zx} & L_{zy} & L_{zz} \end{bmatrix} \tag{4.15}$$

Thanks to the symmetry of H_s, the problem consists of six unknowns, namely L_{xx}, L_{yy}, L_{zz} and the mixed derivatives L_{xy}, L_{xz}, L_{yz}. Since L_s is known only on Σ, its derivatives must be deduced from its directional derivatives along the surface. Introducing the following parametrization

(ξ, η) for Σ:

$$\begin{cases} x = x(\xi, \eta) \\ y = y(\xi, \eta) \\ z = z(\xi, \eta) \\ L_s = L_s(x(\xi, \eta), y(\xi, \eta), z(\xi, \eta)) \end{cases} \tag{4.16}$$

The first order derivative with respect to ξ can be written as:

$$L_\xi = L_x x_\xi + L_y y_\xi + L_z z_\xi \tag{4.17}$$

Eq. (4.17) can be then used to obtain the second order derivative:

$$\begin{aligned} L_{\xi\xi} &= \frac{\partial}{\partial \xi} \left[L_\xi \right] = \frac{\partial}{\partial \xi} \left[L_x x_\xi + L_y y_\xi + L_z z_\xi \right] = \\ &= L_{x\xi} x_\xi + L_x x_{\xi\xi} + L_{y\xi} y_\xi + L_y y_{\xi\xi} + L_{z\xi} z_\xi + L_z z_{\xi\xi} \end{aligned} \tag{4.18}$$

The other second order derivatives, $L_{\eta\eta}$ and $L_{\xi\eta}$ can be found similarly, obtaining the following equations:

$$\begin{cases} x_\xi^2 L_{xx} + 2x_\xi y_\xi L_{xy} + 2x_\xi z_\xi L_{xz} + y_\xi^2 L_{yy} + 2y_\xi z_\xi L_{yz} + z_\xi^2 L_{zz} = \\ \qquad = L_{\xi\xi} - x_{\xi\xi} L_x - y_{\xi\xi} L_y - z_{\xi\xi} L_z \\ x_\eta^2 L_{xx} + 2x_\eta y_\eta L_{xy} + 2x_\eta z_\eta L_{xz} + y_\eta^2 L_{yy} + 2y_\eta z_\eta L_{yz} + z_\eta^2 L_{zz} = \\ \qquad = L_{\eta\eta} - x_{\eta\eta} L_x - y_{\eta\eta} L_y - z_{\eta\eta} L_z \\ x_\xi x_\eta L_{xx} + (x_\xi y_\eta + x_\eta y_\xi) L_{xy} + (x_\xi z_\eta + x_\eta z_\xi) L_{xz} + y_\xi y_\eta L_{yy} + \\ \qquad + (y_\xi z_\eta + y_\eta z_\xi) L_{yz} + z_\xi z_\eta L_{zz} = L_{\xi\eta} - x_{\xi\eta} L_x - y_{\xi\eta} L_y - z_{\xi\eta} L_z \end{cases} \tag{4.19}$$

The directional derivatives along ξ and η in Eq. (4.19) can be computed numerically.

In addition, by considering the derivative of Eq. (4.10) with respect to x,y and z, we can write:

$$\begin{cases} L_x L_{xx} + L_y L_{xy} + L_z L_{xz} = n n_x \\ L_x L_{xy} + L_y L_{yy} + L_z L_{yz} = n n_y \\ L_x L_{xz} + L_y L_{yz} + L_z L_{zz} = n n_z \end{cases} \tag{4.20}$$

Eqs. (4.19) and (4.20) form a system of six equations for the six unknowns from which H_s can be estimated. Particular care must be taken before inverting the system to check for pathological situations such as a grazing incidence, in which case the matrix can be severely ill-conditioned.

4.2.4 Parallel Fast Marching Algorithms

The standard FMM presented in Section 4.2.2 enforces the causality relation through the heap data structure representing the narrowband. Since the trial node must be selected at every step of the algorithm, the update is intrinsically sequential. A more efficient procedure aimed at increasing the performance should enforce the causality relation without relying on the burdensome ordered list to manage the narrowband. Furthermore it should allow the concurrent update of several nodes, in order to be amenable to a parallel execution. In this Section, two algorithms are presented to accelerate the numerical computation of the eikonal equation, the Fast Sweeping Method and the Fast Iterative Method. Both approaches employ the same Godunov upwind finite difference scheme introduced for the FMM, but they differ in terms of the criterion adopted to traverse the computational domain.

Fast Sweeping Method

According to the Fast Sweeping Method (FSM)[72], the narrowband is completely dismissed. Conversely, the node are traversed (*swept*) along prefixed directions. Typically, the coordinate directions of a Cartesian computational grid are used. This means that, for a 3D problem, six sweeps are performed, two in the positive and negative directions of the x axis, two in the positive and negative directions of the y axis, and two in the positive and negative directions of the z axis. Each sweep enforces the causality re-

lation simultaneously for each wavefront propagating in the same direction. While the algorithm does not require an ordered data structure, it requires several iterations before converging. The actual number of iteration strongly depends on the refractive index distribution of the medium[73]. If we denote as κ the number of iterations required, the computational complexity of the FSM is $O(\kappa N)$.

Fast Iterative Method

The second approach presented has been explicitly devised for the execution on Single Instruction Multiple Data (SIMD) platforms, such as GPUs. It is based on three main points:

- The algorithm should not use any particular order to scan the nodes;
- it should enable the simultaneous update of nodes;
- it should not rely on a heterogeneous ordered data structure to store the active nodes.

The first point guarantees proper coalesced accesses to the global memory. On the other hand, the update scheme employed by the FMM would lead to an highly irregular data access pattern. The second point is needed to keep the GPU cores busy, thus matching the SIMD programming model and increasing the algorithm efficiency. Concerning the third point, maintaining an ordered list of the active points requires the execution of

instructions on a very limited amount of data, which does not match the SIMD programming model.

While the Fast Iterative Method (FIM) does exploits a narrowband, it does not require an ordered list of points. Rather, it allows to update all the node simultaneously by solving Eq. (4.11). The FIM is summarized in Algorithm 3. When the eikonal value associated to a node does not change significantly, the node is considered converged and removed from the narrowband. Its close neighbors in turn are checked for convergence. If the eikonal associated to those node changes, i.e. is affected by the newly converged one, they are added to the narrowband. It should be noted that, according to this algorithm, each node can re-enter the narrowband multiple times if it is found to be affected by one of its neighbors. The iterations stop when the narrowband is exhausted. In Fig. 4.4, the advancement of the narrowband for the FIM and for the simple case of a point source located at the center of the computational grid is illustrated. For this particular case, the active nodes depend only on the adjacent upwind nodes which have been concurrently calculated at the previous step. Since the wavefront expands always in the same direction, the nodes reach convergence in one step only and they are immediately removed from the active list after one single update. This simple example highlights the fact that, if the wavefront expands in the same direction as the narrowband, then the "causality condition" is fulfilled and very few eikonal updates are needed.

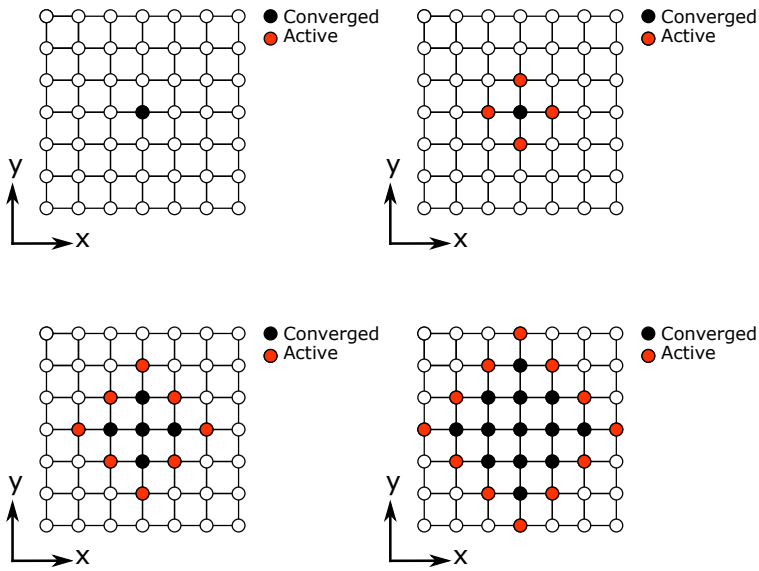

Figure 4.4. Advancement of the narrowband during the first steps of the FIM iterations for a simple case.

Algorithm 3: Fast Iterative Method

"NB" set of active nodes;

while $NB \neq \emptyset$ **do**

  foreach *node* $P \in NB$ *in parallel* **do**

    $p \leftarrow L(P)$;

    $q \leftarrow$ solution to Eq. (4.11);

    $L(P) \leftarrow q$;

    if $|p - q| < \epsilon$ **then**

      Remove P from NB;

      Check neighbor nodes:

      foreach P_{nb} *adjacent to* P **do**

        if $P_{nb} \notin NB$ **then**

          $p \leftarrow L(P_{nb})$;

          $q \leftarrow$ solution to Eq. (4.11);

          if $p > q$ **then**

            $L(P_{nb}) \leftarrow q$;

            Add P_{nb} to NB;

4.3 Implementation of the Fast Marching Method

4.3.1 Parallel Fast Iterative Method for GPU

In this Section, the GPU implementation of the FIM is presented. In particular, the NVIDIA® Kepler CUDA architecture[74] has been considered. The underlying idea is to split the computational domain in blocks, each comprising a predefined number of nodes. As an example, Fig. 4.5 shows a 2D 8×8 computational grid split into four 4×4 blocks. The nodes within a block are updated simultaneously, similarly to the "brute-force" approach of [62]. The blocks are instead treated as a single node of the FIM algorithm described in Section 4.2.4. Accordingly, the narrow-band lists active blocks, rather than active nodes, which are checked for convergence. The convergence of a block requires that all its nodes have themselves reached the convergence. This condition can be flagged by the boolean variables C^{block} and C_i^{node} describing the convergence of the block and of the i-th node, respectively. C^{block} is true only if every node has reached convergence, i.e. if all the C_i^{node} are true. C^{block} can be evaluated by performing a parallel reduction[75] on the values C_i^{node} for all the nodes. The steps of the GPU implementation of the FIM are summarized in Algorithm 4. The new partitioning introduced can be immediately matched to the SIMD execution model. Indeed, a CUDA function launched on a GPU, known as *kernel*, consists of several blocks of threads running in parallel

on different cores. Each block of the FIM coincides with a CUDA thread block, and each thread within the block manages the update of a single node. The new update algorithm accelerates the convergence because each time a CUDA kernel is launched, the nodes are update several times within the thread block, following the algorithm of [62]. The internal updates help increase the efficiency by keeping the GPU core busy and requiring less kernel executions, thus reducing the overhead cost associated to each kernel launch. Furthermore, they can benefit of the GPU Shared Memory[74], which have a dramatic effect on the performance[73]. To this end, the data relative to the block is copied once from the slow Global Memory, and the update iterations are performed in the Shared Memory. When the block reaches convergence, the data is copied back to the Global Memory.

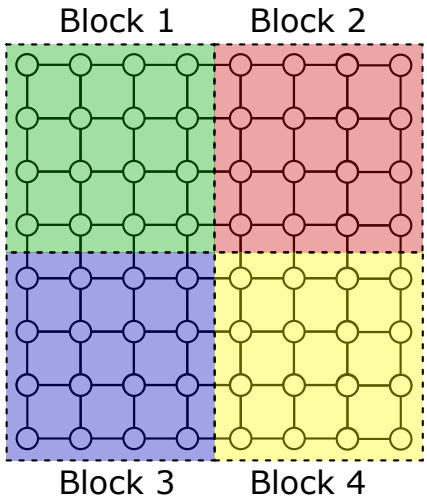

Figure 4.5. Partition of the computational grid into blocks.

Algorithm 4: Parallel FIM for GPU.

```
"NB" set of active blocks;
while NB ≠ ∅ do
    Step 1: Active Blocks Update
    foreach block B ∈ NB in parallel do
        Internal Block updates loop:
        for i = 0 to n_iter do
            foreach node P ∈ B in parallel do
                P ← solution to Eq. (4.11);
        C^block ← reduction {C_i^node};
    Step 2: Check neighbor blocks:
    foreach block B ∈ NB in parallel do
        if C^block = TRUE then
            foreach block B_nb adjacent to B do
                foreach node P ∈ B_nb in parallel do
                    P ← solution to Eq. (4.11);
                C^block ← reduction {C_i^node};
    Step 3: Active blocks list update
    clear(NB);
    foreach B do
        if C^block = TRUE then
            Add B to NB;
```

GPU Memory Access Optimization

Global Memory Transfers An important aspect, that has been addressed to exploit the full performance of the GPU, concern the optimization of the data transfer from the CPU to the GPU global memory and the accesses to the GPU shared memory. Global memory loads and stores by threads are grouped (coalesced) by the device into as few transactions as possible, provided that they involve contiguous addresses. As the data is typically stored as an 1D array with a certain traversing order, keeping its ordering and simply coping it to the GPU would prevent coalescent reads from the thread blocks. This case is illustrated in Fig. 4.6, which, as an example, shows the case of a 4×4 matrix split in four 2×2 blocks. The data belonging to a thread block is highlighted in green. This data is split into two regions in the GPU global memory, which requires split block accesses. The coalescence can be restored by rearranging the data in the global memory as shown in Fig. 4.7. In this case, the block can be accessed in the most efficient way available by a single memory access.

Shared Memory Access The shared memory space in the NVIDIA Kepler architecture is divided into a configurable number of memory modules referred to as *banks*. Any memory load or write spanning over distinct memory banks can be serviced simultaneously. However, if different threads request an access to the same bank, they are serialized. The conflicting memory requests are then split into as many separate conflict-free requests

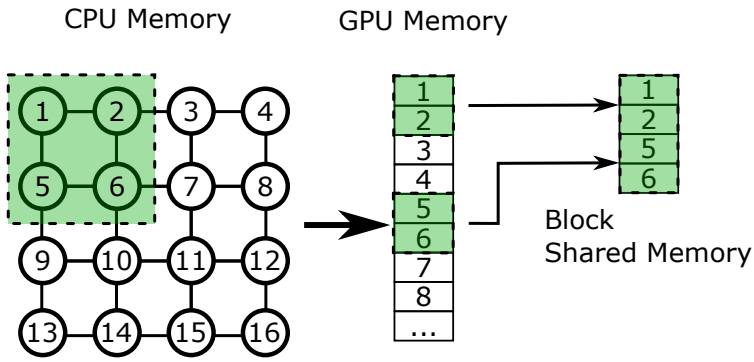

Figure 4.6. Non-coalesced Global memory access.

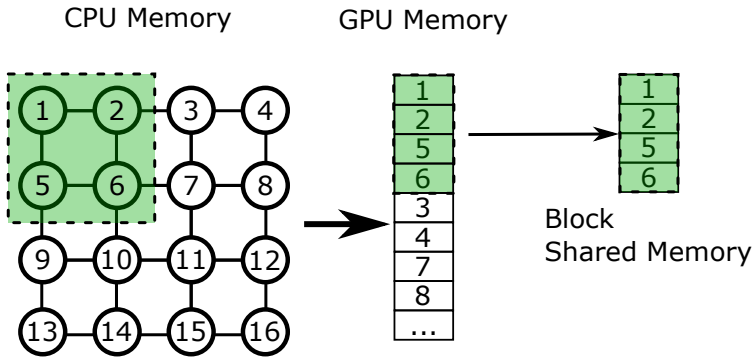

Figure 4.7. Coalesced Global memory access.

are necessary, effectively decreasing the bandwidth by a factor equal to the number of colliding requests. To avoid bank conflicts, the data must be carefully arranged based on how it will be accessed. To clarify this aspect, let us consider a 2D example, shown in Fig. 4.8. In this example, the size of the block is 16 (4×4). The shared memory is assumed made up by 16 banks. The block needs a halo region to access its surrounding neighbor nodes. By allocating a memory three times larger than the block size, the data can be arranged as shown in Fig. 4.8. The central nodes, whose neighbors belong to the same block, are stored in dedicated banks. The nodes on the border can share the same bank because they will not be accessed together during the update. As an example, Fig. 4.8 highlights the access pattern when left neighbors are accessed. As it can be seen, the 16 nodes belong each to a different bank, thus no bank conflict arises. The cases for the right, up, and down neighbors are similar. The bank assignment technique shown is easily extended to 3D cases.

4.3.2 Inverse Ray Tracing

The explicit solution to the eikonal equation enables the setting up of an inverse ray tracing scheme. Accordingly, the rays are traced backwards to the source, so that only those rays in a prescribed region where the field is of interest can be considered, saving computational resources. On the other hand, a direct ray tracing would require in general an unpredictable number of rays to reach the region of interest with a satisfying accuracy.

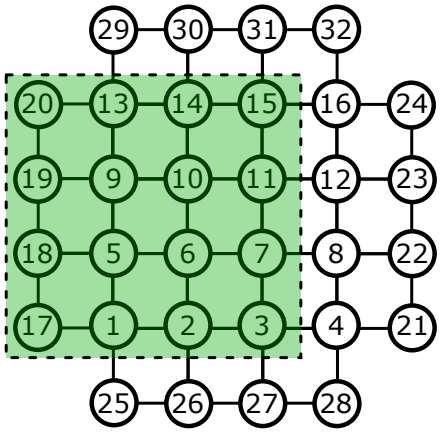

Banks	Node index		
1	1	21	29
2	2	30	
3	3	31	
4	4	17	32
5	5	22	
6	6		
7	7		
8	8	18	
9	9	23	
10	10		
11	11		
12	12	19	
13	13	24	25
14	14	26	
15	15	27	
16	16	20	28

Figure 4.8. Shared memory banks arrangement for a conflict free access .

By noticing that the rays are the lines of force of the vector field $\underline{\nabla} L$ and introducing a representation $(x(s), y(s), z(s))$ for the generic ray, s being the path length, then tracing a ray amounts at solving the following equation:

$$\frac{d}{ds}(x(s), y(s), z(s)) = \underline{\nabla} L(x(s), y(s), z(s)) \tag{4.21}$$

Eq. (4.21) represents a first order differential equation, which can be efficiently solved by a fourth-order Runge-Kutta method with a variable step size[63]. It should be noted that since Eq. (4.21) refers to a single ray, the computation for the complete congruence is readily parallelized. In the framework of a GPU implementation, a single ray can be traced by

a Compute Unified Device Architecture (CUDA) thread. Since the rays start from a different points and are traced through regions with (possibly) different refractive index, they can describe very different trajectories. Accordingly, solving Eq. (4.21) requires values of $\underline{\nabla} L$ from different regions of the computational domain. Even though this results in incoherent memory accesses, which does not match the SIMD model, it allows to keep the computation on the GPU, saving the substantial cost of transferring the data to the host memory.

4.3.3 Managing multiple interactions

The method illustrated in the previous sections allows evaluating the field scattered by a single surface. When dealing with scenes in which multiple objects are present, the calculation of their mutual interactions must be included.

To introduce the problem, let us consider, as a first example, a geometry composed of two objects as illustrated in Fig. 4.9. In this scenario, a source generates an incident field (depicted in yellow) which gives rise to the reflected and transmitted fields (depicted in red) representing the first order contributions to the total field. Since the contributions are independent, they can be determined applying the algorithm described so far to each object separately. Second order contributions (depicted in blue) can be taken into account by applying the algorithm again with the first order fields as the sources. Further interactions can be included in

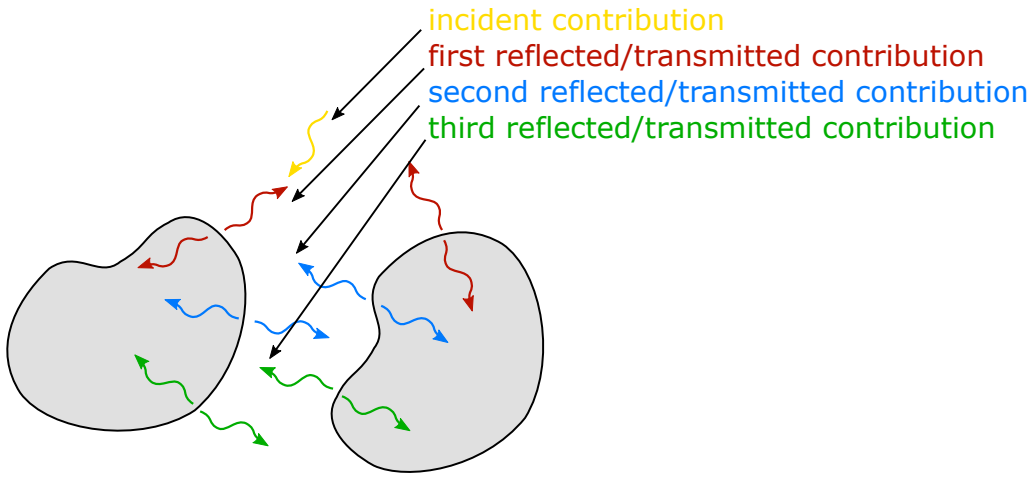

Figure 4.9. Scattering by two objects. The incident field is depicted in yellow, the first contributions to the reflected/trasmitted field in red. The second and third contributions are depicted in blue and green, respectively.

the same fashion, giving rise to an iterative procedure. Each step of the iteration requires the evaluation of the eikonal associated to the field and the corresponding ray tracing, so the overall procedure can be expensive in terms of computational time and memory needed. Therefore, to manage an arbitrary number of mutual interactions in a rational way, accelerating the computation and allowing its parallelization, we introduce a search tree data structure[76]. Each field contribution in the previous example can the thought as a node of the tree with its branches being the corresponding interactions. To illustrate the search tree in a general case, let us consider the set of mutual interactions in a geometry composed of N objects up to an order of interaction K. The primary source represented by the root node R gives rise to N first order contributions, one for each object, associated

to the nodes on the first level of the three. For this case, N branches leave from the root node R to the N nodes of the first level. Each one of these nodes represents the first contribution from the corresponding object when illuminated by the source. $(N-1)$ branches leave from a given node of the first level corresponding to the second order contributions. The overall number of nodes on the second level is then $N(N-1)$. Likewise, the third level consists of $N(N-1)2$ nodes corresponding to the third order contributions. Repeating the procedure for K levels of interactions, a total number of $N(N-1)K$ nodes is obtained. Each node has been implemented as a struct containing:

- the geometrical features of the scattering object;
- its refractive index distribution;
- the parent node;
- the eikonal reflected and refracted by the object;

The resulting tree, shown in Fig. 4.10, is an exhaustive representation of all the possible interactions up to the prescribed order. The evaluation of the total field based on the search tree of Fig. 4.10 consists of two steps. As with the algorithm presented for a single object, the evaluation of the total field based on the search tree of Fig. 4.10 consists of two steps, namely the eikonal calculation and the inverse ray tracing. In particular:

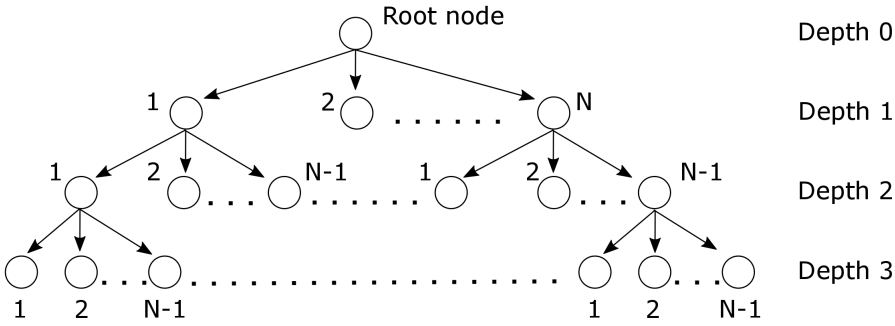

Figure 4.10. Interactions search tree.

1. In the first step, the eikonal associated to each contribution is obtained by performing the FIM for each node and by traversing the tree from the top to the bottom. Each node corresponds to the eikonal reflected by an object when illuminated by the field associated to its parent node;

2. In the second step, the inverse ray tracing is performed. Starting from the region where the field is of interest, for each node the rays are traced back to the surface of the corresponding object. The final positions of the rays then constitute new initial conditions to continue the tracing towards the parent node. The procedure is iterated traversing the tree backwards until the root node is reached.

After these two steps, all the field contributions can be summed to obtain the total field.

The described representation allows not only to automatically manage the interactions of multiple objects, but it also enables their parallel compu-

tation. In particular, the nodes on a given level represent independent contributions due to the same source. Therefore, during step 1, all the eikonal calculations on the same level can be performed concurrently. In the GPU implementation of the FIM, this is achieved by splitting the kernel launches into different CUDA streams (Fig. 4.11). Accordingly, the eikonal computations are scheduled by the GPU itself, so, even when the algorithm launches a large number of FIM kernels, their parallelization is managed automatically.

A similar observation is valid for step 2. Indeed, as for the ray tracing presented in Section 4.3.2, each congruence, and thus each branch of the tree, is independent of the others. The ray tracing can be then parallelized in the same way of the eikonal computation, by assigning each branch traversal to a different CUDA stream.

A numerical example using this tree data structure is presented in Section 5.1.3.

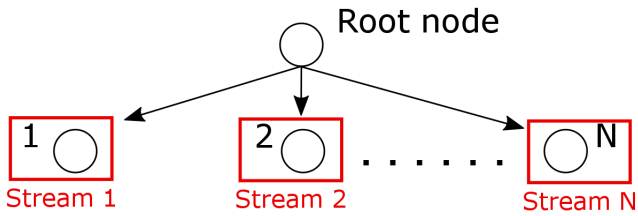

Figure 4.11. The eikonals associated with nodes on the same level are independent and can be computed in parallel. Accordingly they are assigned to different CUDA streams to be scheduled by the GPU.

Chapter 5

Numerical and Experimental Results

The present Chapter deals with the validation of the optimized the diagnosis method introduced in Chapter 3 and of the GO tool based on the FMM presented in Chapter 4. First, numerical tests have been performed to assess the validity of the approaches and to evaluate the performance of the implemented algorithms. To this end, reliable commercial software has been exploited. Furthermore, to complete the analysis, an experimental validation of the optimized diagnosis has been carried out. Accordingly, an outdoor far field test range has been set up thanks to the collaboration with Istituto Nazionale di Astrofisica (INAF). In particular. the measurements were conducted within the facility of the Observatory of Capodimonte,

Naples, Italy. Section 5.2.1 describes the instrumentation and the geometry of the AUT adopted in relation to the development of the measurement setup.

5.1 Numerical test cases for the Fast Marching Method

In this section, a number of numerical tests are presented for the FMM. The FIM algorithm introduced in Section 4.3.3, together with the inverse ray tracing and transport equation presented in Section 4.3.2 and Section 4.1.1, respectively, have been implemented in CUDA to allow their execution on GPU. The computational routines are called from a C++ program built with the MEX compiler[77], which provides a convenient interface with MATLAB to access and display the results.

The presented cases refer to canonical problems and are meant to show the performance of the proposed approach. To provide a reference solution to compare the results, the canonical cases have been simulated also in FEKO using the Method of Moments (MoM). All the simulations have been run on a workstation equipped by an eight core Intel Xeon E5-2650 clocked at 2 GHz and NVIDIA Kepler K20c cards. In Section 5.1.2, as a first example, the field scattered by a conducting sphere embedded in a homogeneous medium is illustrated to show the accuracy of the method. In addition, a direct ray tracing is shown as for a comparison to highlight the

convenience of the inverse ray tracing in selecting the minimum number of rays. The second case, presented in Section 5.1.3, consists of a conducting sphere coated by a dielectric material. In third case, presented in Section 5.1.4, the FMM has been applied to a continuous, non homogeneous medium represented by a Luneburg lens[78]. In the final example, presented in Section 5.1.5, the FMM has been applied to a case relevant to the diagnosis, consisting in the evaluation of the phase distribution of the AF of a parabolic reflector affected by a feed misalignment.

5.1.1 Benchmark Results

In this Section, some benchmark results are presented to highlight the computational efficiency of the parallel implementation of the FIM, detailed in Section 4.3.1, and of the tree data structure, described in Section 4.3.3. To test the FIM, a homogeneous medium has been considered with a computational grid comprising $N \times N \times N$ with N ranging from 32 to 512. Fig. 5.1 show the execution times for the sequential FMM and for the parallel FIM. Fig. 5.2 shows the corresponding speedup. As it can be appreciated, the FIM allows to dramatically accelerate the computation with a maximum speedup equal to 70. The show the performance of the tree, the interactions between a number of objects with an increasing maximum mutual interaction level have been considered. In particular, Fig. 5.3 show the speedup achieved for the calculation of the eikonal thanks to the parallelization allowed by the tree. Fig. 5.4, on the other hand,

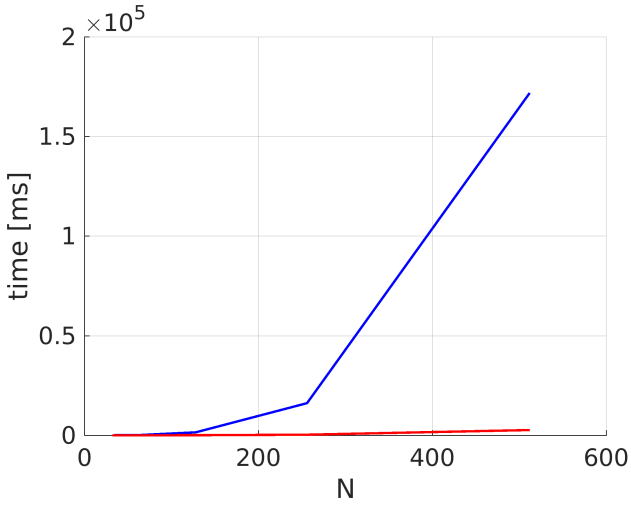

Figure 5.1. Execution times for a $N \times N \times N$ sized grid for the FMM (in blu) and for the FIM (in red).

shows the speedup achieved for the ray tracing step. As it can be seen, the speedup reaches a plateau after 4 mutual interactions, meaning that all the hardware resources of the GPU are fully occupied by the computation.

5.1.2 Scattering from a conducting sphere

In the first example, the scattering from a conducting sphere is shown and compared with a reference solution. The sphere is illuminated by an x-polarized plane wave of unit amplitude and frequency equal to 5 GHz (λ=6 cm), propagating along the negative direction of the z-axis. The sphere is centered at the origin of the reference system and has a radius of 10λ. A $32\lambda \times 32\lambda \times 32\lambda$ sized domain, with a discretization step of $\lambda/6$, is employed as the computational domain. The ray tracing for the calculation of the

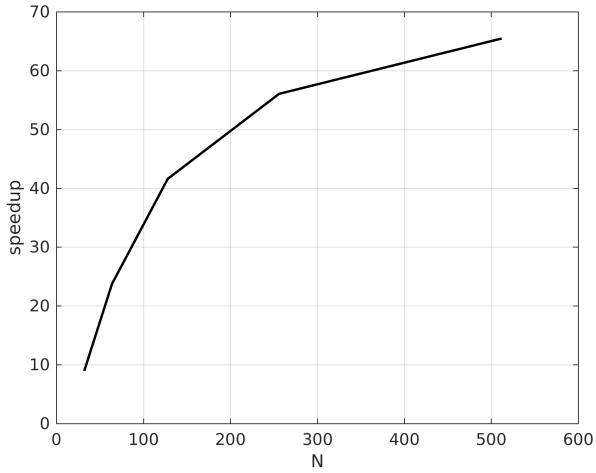

Figure 5.2. Speedup for a $N \times N \times N$ sized grid between the FMM and the FIM.

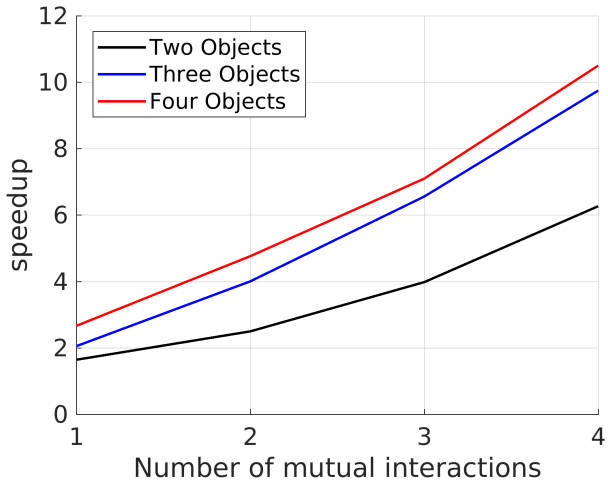

Figure 5.3. Speedup achieved by the tree data structure for the eikonal evaluations with an increasing number of mutual interations between two (black line), three (blu line) and four (red line) objects.

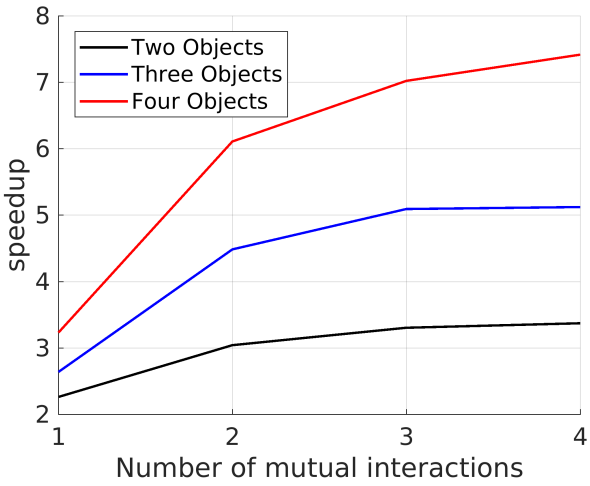

Figure 5.4. Speedup achieved by the tree data structure for the ray tracing step with an increasing number of mutual interations between two (black line), three (blu line) and four (red line) objects.

field amplitude has been performed in the $x = 0$ plane, and all the results are relative to this plane.

Fig. 5.5 shows the eikonal obtained for the reflected field with a superimposed contour plot to highlight the corresponding wavefronts. In Fig. 5.5, the red arrow shows the direction of the incident wavevector while the surface of the sphere is highlighted by the red circumference. The evaluated total field, shown in Fig. 5.6, can be compared to the reference obtained from FEKO, shown in Fig. 5.7. The solution obtained with the proposed algorithm shows a good agreement with the reference solution in the region in front of the sphere, as can be appreciated from Fig. 5.8, which shows a superposition of the two solutions for the total field on the segment $x = 0$,

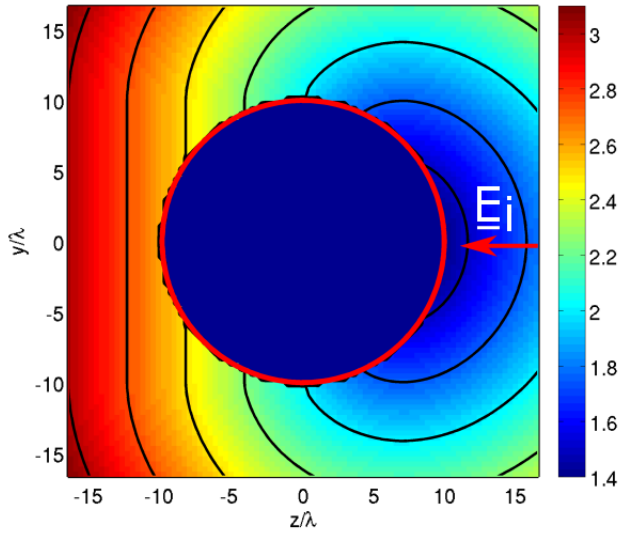

Figure 5.5. Scattering from a conducting sphere: Eikonal associated to the reflected field. The contour plot (black lines) shows the corresponding wavefronts. The red arrow represents the direction of the incident wavevector. The surface of the sphere is highlighted by the red circumference.

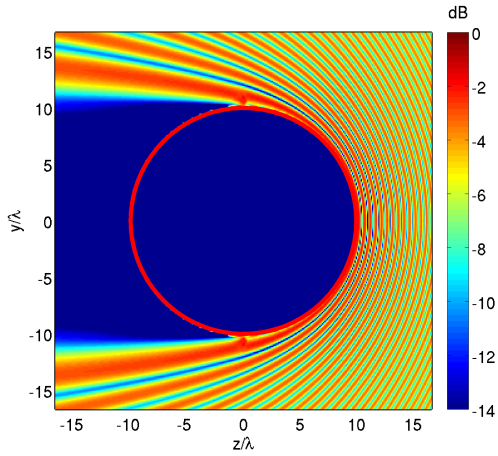

Figure 5.6. Scattering from a conducting sphere: Amplitude (in dB) of the total field obtained by the proposed algorithm.

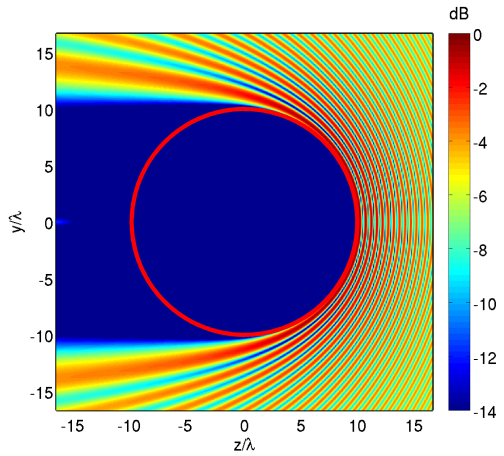

Figure 5.7. Scattering from a conducting sphere: Amplitude (in dB) of the total field obtained by FEKO.

$y = 0$ and $z \in (-10\lambda, 17\lambda)$.

To highlight the convenience of the inverse ray tracing, the comparison with the direct ray tracing is shown. Let us assume that the field is requested along the segment $x = 0$, $y = 18\lambda$ and $z \in (-10\lambda, 10\lambda)$ with a $\lambda/2$ spacing. The inverse scheme allows to discretize directly the region of interest with the prescribed spacing and to trace only the minimum number of required rays, as shown in Fig. 5.9, where the blue dots represent the points in which the field is requested. A total number of 40 rays has been traced for this case. Concerning now the direct ray tracing, the initial conditions for the plane wave and are assigned on equispaced points on the boundary of the computational domain. Fig. 5.10 shows the reflected rays for this case, in which a minimum number of 300 rays has been required to meet the

desired spacing. Note that, in this example, only the direct rays actually impinging the sphere are shown. For this test case, the number and the location of the rays could be assessed a priori due to the canonical shape of the object. In a general problem, however, for which the scene consists of different scatterers with non-canonical shapes, the number of rays to be traced could be difficult to predict in advance and it is expected to be much higher than the bare minimum. The example shows that the FMM and the inverse ray tracing allow an efficient approach to the evaluation of the scattered field. The convenience is even more apparent in cases where the ray divergence is severe, such as in "truly" three-dimensional problems, that is, when the field is requested in a three-dimensional region so that the rays are not confined on a plane, or when dealing with an inhomogeneous medium[79].

5.1.3 Scattering from a coated sphere

As a second example, the scattering from a conducting sphere coated by a dielectric shell is presented. The example shows the effectiveness of the tree data structure presented in Section 4.3.3 to correctly describe the interaction between the sphere and its coating. The sphere is illuminated by an x-polarized plane wave of unit amplitude and frequency equal to 1 GHz (λ=30 cm), propagating along the positive direction of the z-axis. The sphere, whose geometry is shown in Fig. 5.11, is centered at the origin of the reference system and has a radius r_1 equal to 3λ. The coating

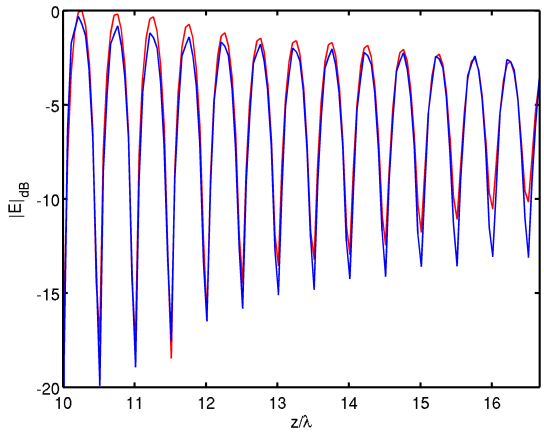

Figure 5.8. Scattering from a conducting sphere: Cuts of the amplitude (in dB) of the total field obtained by the proposed algorithm (blue line) and by FEKO (red line) along a portion of the $z = 0$ axis.

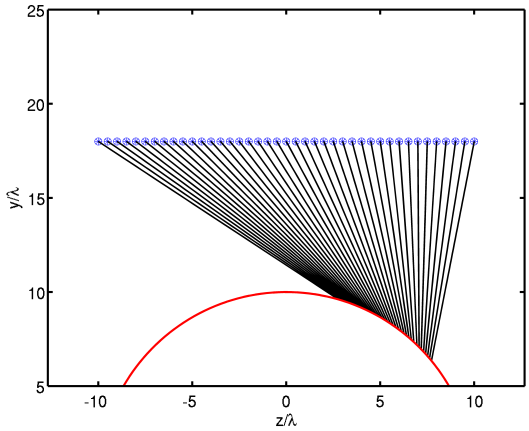

Figure 5.9. Scattering from a conducting sphere: Inversely traced rays.

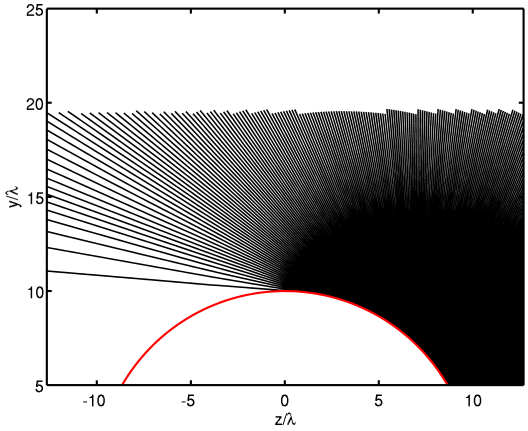

Figure 5.10. Scattering from a conducting sphere: Directly traced reflected rays.

dielectric has a radius r_2 equal to 5λ and a relative permittivity $\epsilon_r = 1.2$. A $16\lambda \times 16\lambda \times 16\lambda$ sized domain, with a discretization step of $\lambda/6$, is employed as the computational domain. The ray tracing for the calculation of the field amplitude has been performed in the $x = 0$ plane and all the results shown are relative to this plane. The evaluated total field, shown in Fig. 5.12, can be compared to that obtained by FEKO, shown in Fig. 5.13. In both Fig. 5.12 and Fig. 5.13, the surface of the outer sphere is highlighted by the red circumference. The solution obtained with the proposed algorithm shows a good agreement with the reference solution in the region in front of the sphere, as can be appreciated from Fig. 5.14, which shows a superposition of the two solutions for the total field on the segment $x = 0$, $y = 0$ and $z \in (-6.5\lambda, -3\lambda)$. In the region behind the sphere the proposed algorithm

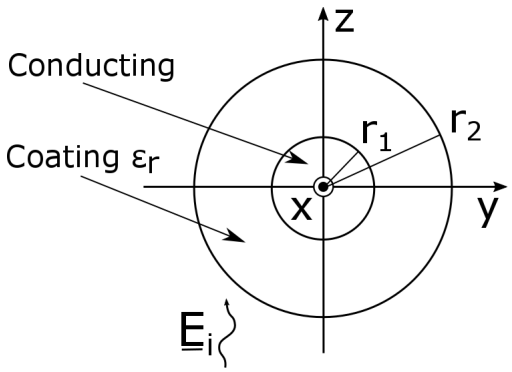

Figure 5.11. Geometry of the scattering from a coated sphere.

predicts a different field from the reference solution. Indeed, in this region the GO approximation breaks down because the rays intersect developing caustics.

5.1.4 Simulation of a Luneburg lens

As a third example, the propagation through a continuous non homogeneous medium is shown. In particular, a spherical Luneburg lens is considered[78]. The lens works at 1 GHz and is excited by a point-like source located at one of its foci, located at $(0, -3\lambda, 0)$. The lens radius is equal to $R = 1.5\lambda$, the computational domain has been $3\lambda \times 3\lambda$ sized and it has been discretized again with a $\lambda/6$ step. The refractive index distribution, shown in Fig. 5.15, is given by:

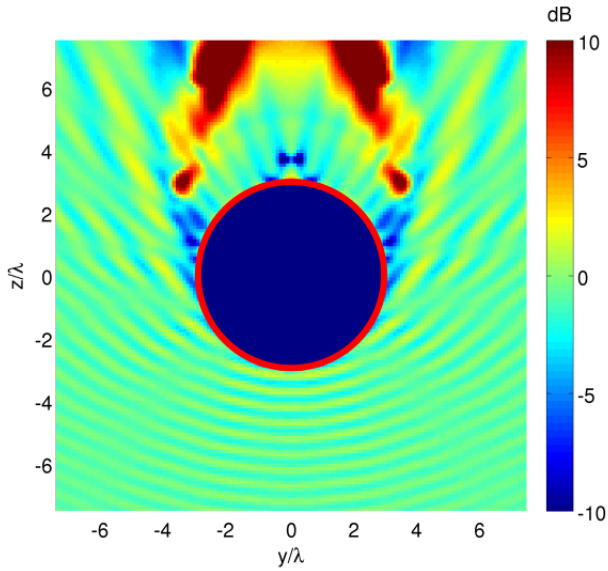

Figure 5.12. Scattering from a coated sphere: Amplitude (in dB) of the total field obtained by the proposed algorithm.

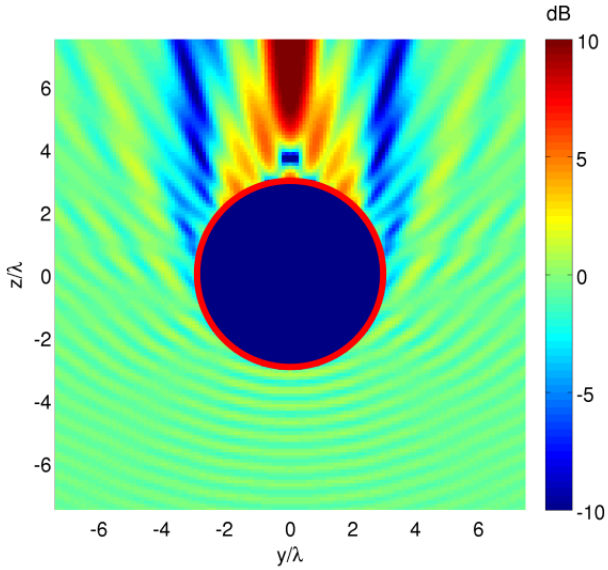

Figure 5.13. Scattering from a coated sphere: Amplitude (in dB) of the total field obtained by FEKO.

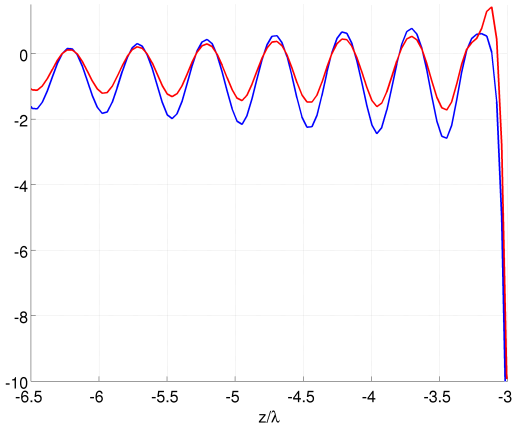

Figure 5.14. Scattering from a coated sphere: Cuts of the amplitude (in dB) of the total field obtained by the proposed algorithm (blue line) and by FEKO red line) along a segment on the z-axis.

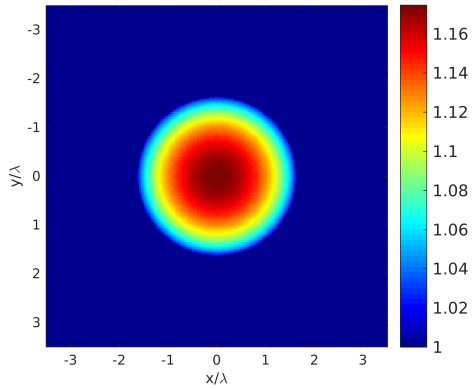

Figure 5.15. Case of Luneburg lens: Refractive index distribution for the Luneburg lens.

$$F(x,y,z) = \begin{cases} \sqrt{2 - \left(\frac{\sqrt{x^2+y^2+z^2}}{R}\right)^2} & \sqrt{x^2+y^2+z^2} < R \\ 1 & \text{otherwise} \end{cases} \tag{5.1}$$

To allow the simulation of the lens in FEKO, it has been discretized by several homogeneous spherical shells with progressive values of relative permittivity. It is worth mentioning that the maximum dimensions for this case were limited by the high computational cost required by the full-wave solution and not by a limitation of the proposed approach. The total field obtained with the proposed approach is shown in Fig. 5.16 and Fig. 5.17, in amplitude and phase, respectively. The total field obtained with FEKO is shown in Fig. 5.18 and Fig. 5.19, in amplitude and phase, respectively. Some of the traced rays are reported in Fig. 5.20. The rays are traced from

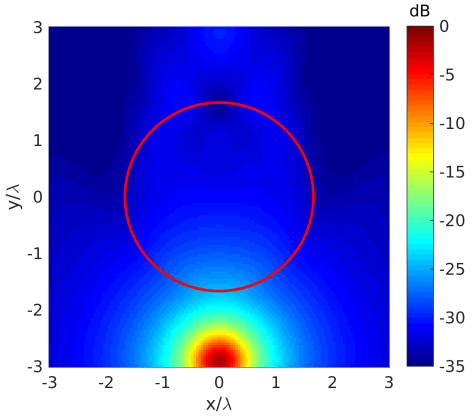

Figure 5.16. Case of Luneburg lens: Normalized amplitude in dB of the total field obtained by the proposed approach.

80 points lying on a square surrounding the lens, represented by blue dots in Fig. 5.20. As it can be seen, the inverse ray tracing allows to uniformly reach the points of the computational domain despite the bending caused by the presence of the lens.

5.1.5 Evaluation of the Aperture Field phase of a parabolic reflector

In this example, the evaluation of the phase distribution of the AF of a parabolic reflector using the FMM is considered. The reflector works at 10 GHz, has a diameter $D = 1\,\text{m}$ and a focal length $F = 0.5\,\text{m}$ and is affected by a large feed misalignment $\Delta x = 5\,\text{cm}$, $\Delta y = 0\,\text{cm}$, $\Delta z = -6\,\text{cm}$ (Fig. 5.21) to clearly show the effects on the aperture phase. Fig. 5.22 shows the eikonal function associated to the field reflected by the reflector

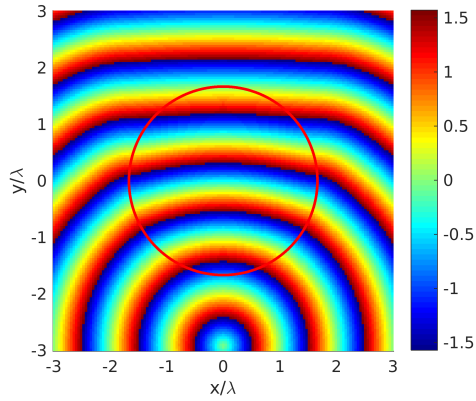

Figure 5.17. Case of Luneburg lens: Phase of the total field obtained by the proposed approach.

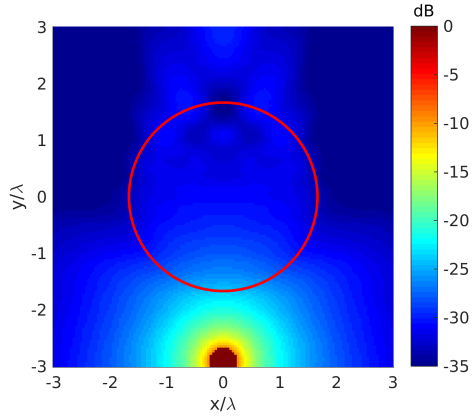

Figure 5.18. Case of Luneburg lens: Normalized amplitude in dB of the total field obtained by FEKO.

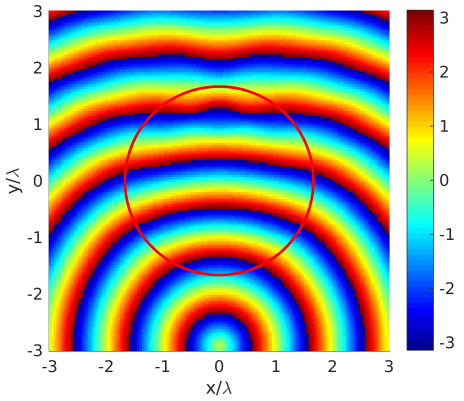

Figure 5.19. Case of Luneburg lens: Phase of the total field obtained by FEKO.

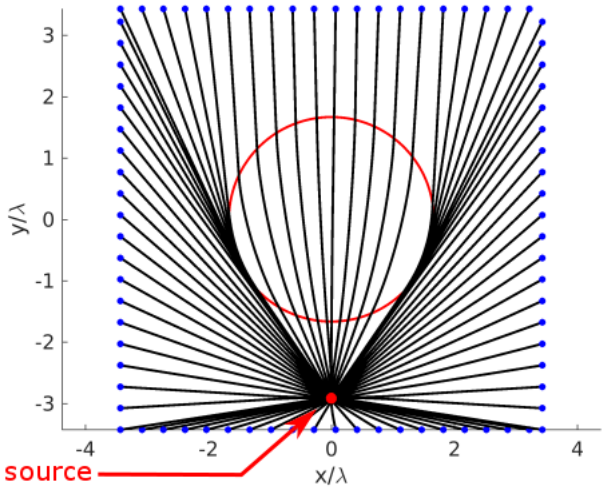

Figure 5.20. Case of Luneburg lens: Inversely traced rays. The blue dots represent the point in which the field is requested. The red dot represents the source position.

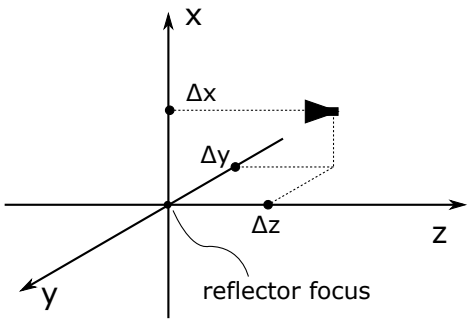

Figure 5.21. Illustrating the feed misalignment.

on the aperture plane. As a comparison, the eikonal has been evaluated also using a standard direct ray tracing to provide a reference, shown in Fig. 5.23. Fig. 5.24 and Fig. 5.25 show two cuts of the eikonal along the $y = 0$ plane and $x = 0$ plane, respectively.

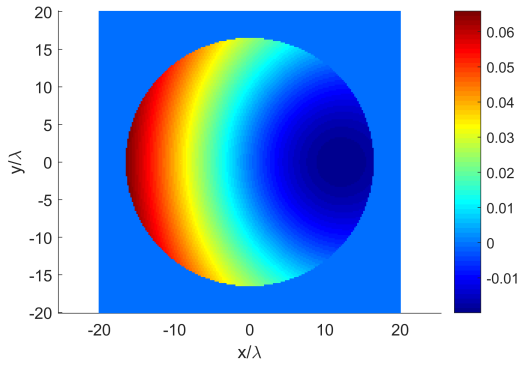

Figure 5.22. Case of misaligned reflector: Eikonal function obtained by the FMM.

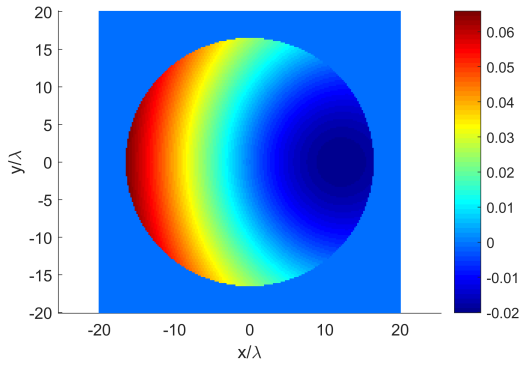

Figure 5.23. Case of misaligned reflector: Eikonal function obtained by the direct ray tracing.

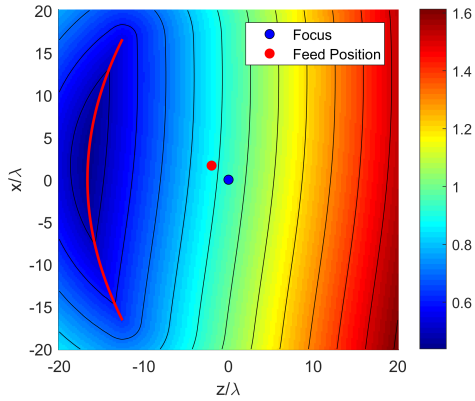

Figure 5.24. Case of misaligned reflector: Eikonal function in the $y = 0$ plane.

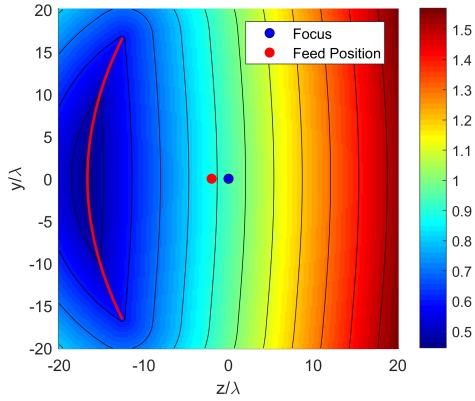

Figure 5.25. Case of misaligned reflector: Eikonal function in the $x = 0$ plane.

5.2 Optimized Diagnosis of a Reflector Antenna

5.2.1 Measurement Setup

In this Section, the measurement setup developed for the experimental validation of the diagnosis of a reflector antennas is presented. As described in Chapter 2, the diagnosis requires the acquisition of the FFP samples by moving the AUT relative to a fixed source, wherein the acquisition of both amplitude and phase is made possible thanks to the use of a second antenna employed as reference. The wavelength of the received signal together with the geometrical dimension of both the AUT and the source impose a minimum distance to satisfy the far field conditions (Eq. (2.19)). The working frequency chosen is equal to 10 GHz, corresponding to a wavelength equal to 3 cm. Given the dimensions of the antennas, reported in Table 5.1, the minimum distance allowed is equal to 16 m. A suitable location wherein realize the test range has been provided by the Observatory of Capodimonte in Naples, and is shown in Fig. 5.26. The facility provides not only a sufficient distance, but it also allows to position the source with some elevation with respect to the AUT, in order to point it upwards and mitigate interference from ground reflections. Both the AUT and the reference antenna have been placed on a platform, as shown in Fig. 5.27. Custom supports have been realized to properly lodge the antenna. The measurement has been remotely controlled from within the facility, as shown by the general layout of Fig. 5.28.

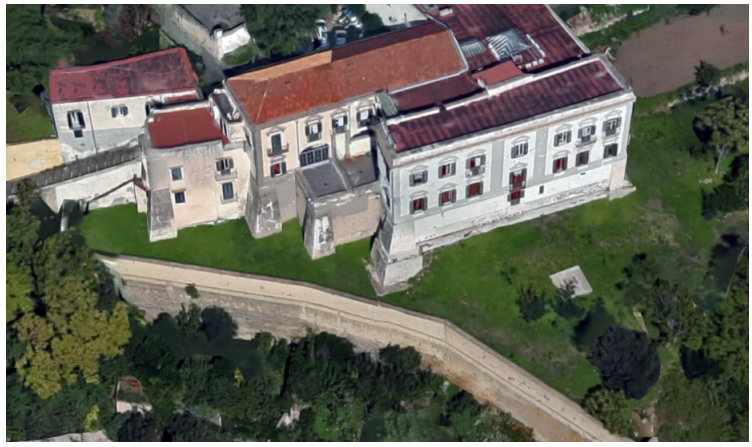

Figure 5.26. The facility at the Observatory of Capodimonte in Naples hosting the test range.

Figure 5.27. The platform hosting the AUT and reference antenna.

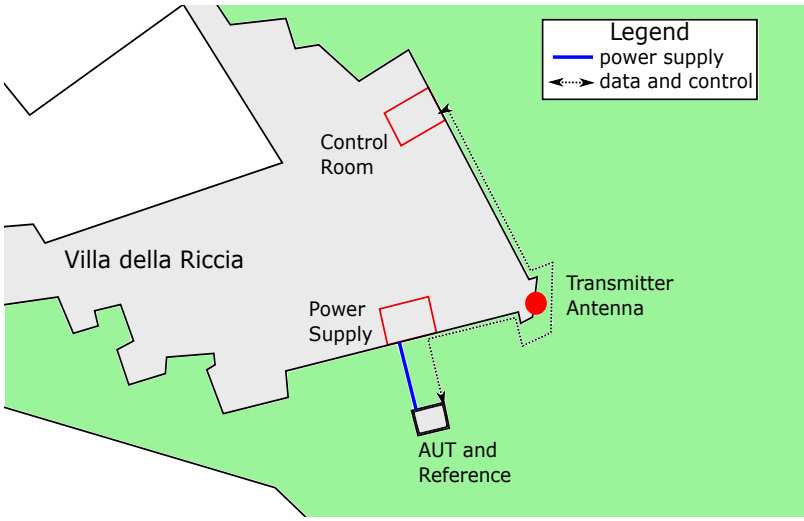

Figure 5.28. Test range layout.

Geometry of the AUT

Off the shelf parabolic reflector antennas have been chosen as both the AUT and the reference antenna (Fig. 5.29). Their geometric features are reported in Table 5.1:

Diameter	0.85 m
Focal length	0.5 m
Offset angle	21°
Focal ratio	0.66
elevation allowed by the mounting	0°-53°

Table 5.1. Geometric parameters of the AUT.

Figure 5.29. The AUT mounted in the test range.

Instrumentation

Vector Network Analyzer (VNA) The acquisition of the FFP is made possible by an Anritsu 37377C VNA. VNAs are commonly employed to measure S-parameters of high frequency electrical networks. Their basic architecture involves an internal microwave generator, providing the test signal, and a tuned receiver. The tuned receiver first down converts the microwave signal to an Intermediate Frequency (IF) using a mixer and then measures its amplitude using a detector. The phase is measured by comparing the signal with a reference. In a typical application, the reference is provided by the same internal generator feeding the AUT.

In a far field test range, however, the VNA cannot be easily connected to both the source and the AUT. A simpler measurement configuration is obtained by resorting to an external generator. In this case, a reference signal, different from the one produced by the instrument internal genera-

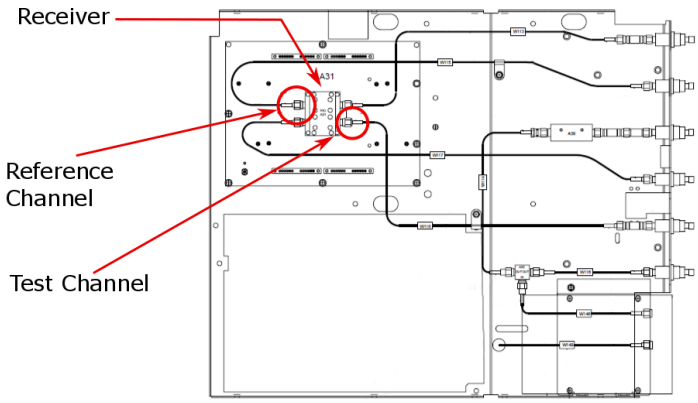

Figure 5.30. The AUT and reference antenna mounted in the test range.

tor, is necessary to provide the phase lock for the down conversion and the subsequent measurement. To this end, in the test realized range, an interferometric configuration has been adopted. Accordingly, the VNA is put in *Set-on Mode*[80], which completely by-passes the source phase lock circuitry and allows to operate over the full dynamic range of the instrument. The phase lock is achieved by feeding the test and reference signal to the receiver mixer. This operation has been made possible by a custom modification of the internal connection of the receiver. In particular, the reference channel port of the receiver, illustrated in Fig. 5.30, has been removed and substituted by an additional port, realized ad hoc to be connected to the reference antenna.

Antenna Positioner The movement of the AUT is provided by a Scientific-Atlanta Azimuth-over-Elevation Positioner (Fig. 5.31). The positioner con-

Figure 5.31. Scientific-Atlanta Azimuth-over-Elevation positioner.

trol hardware, placed in an indoor control room, is made up by:

- 2012A Positioner Controller
- 4180 Positioner Control Unit
- 1842 Digital Synchro Display
- 2013 Synchro Selector

The 2012A controller (Fig. 5.32) is equipped with a standard IEEE-488 (General Purpose Instrumentation Bus - GPIB) interface, allowing to be easily controlled from a PC. The 4180 Control Unit represents the motor driver, while the 2013 Synchro Selector allows to switch the control between the azimuth and elevation axis.

Figure 5.32. Scientific-Atlanta 2012A Positioner Controller.

Instruments remote control To manage and synchronize the acquisition from the VNA and the movement of positioner from the control room, a custom control network has been devised. In particular, thanks to National Instruments GPIB-to-Ethernet adapters, all the instruments can be connected to a router in Local Area Network (LAN) and accessed from a PC. Wireless access points allowed to reach both the antenna test range and the transmitter placed on the roof. Fig. 5.33 shows the complete block diagram of the measurement setup.

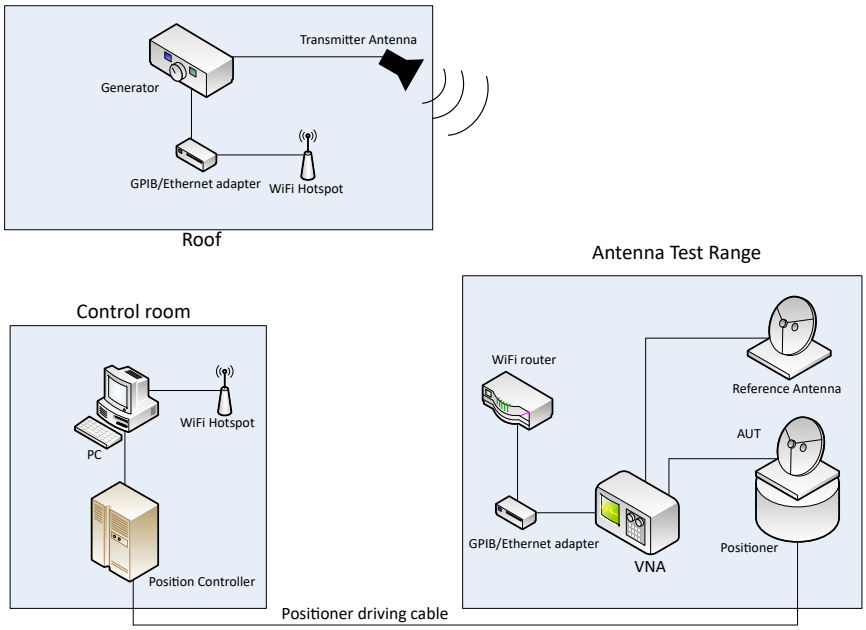

Figure 5.33. Block diagram of the measurement setup.

5.2.2 Operating Conditions

For convenience, the parameters relevant to the antenna configuration are summarized in Table 5.2:

Frequency	10 GHz
Wavelength	0.03 m
AUT Diameter	0.85 m
Focal length	0.5 m
Offset angle	21°

Table 5.2. Operating conditions.

The nominal AF E_{a0} has been obtained in FEKO using a full-wave method with a sample rate equal to $\lambda/2$ and it is shown in Fig. 5.34. The FFP has been measured in the portion of the u-v plane $[-0.25, 0.25] \times [-0.25, 0.25]$, corresponding to an angular window of 30°. To construct the set basis function using the PCA, the aberration function Φ has been first expanded in a Taylor series up to the second order:

$$\Phi(x, y) = p_1 x + p_2 y + p_3 x^2 + p_4 xy + p_5 y^2 \tag{5.2}$$

Then the manifold $\mathcal{M}$ has been sampled by considering different aberration functions obtained by varying each parameter in the interval $(-1, 1)$. The interval has been chosen to represent a maximum feed displacement of 3 cm.

The PCA introduced in Section 3.2.2 has been applied to obtain the optimal basis functions set. Accordingly, a total number of 19 basis functions has been found. Fig. 5.36 and Fig. 5.37 show the first six basis function in amplitude and phase, respectively.

To obtain the optimal number of samples, the iterative procedure described in Section 3.3 has been applied to show the saturation behavior of the functional Ψ. Fig. 5.35 reports the values of Ψ for different numbers of samples M which saturates around $M = 20$. Accordingly, a total number of 24 samples has been chosen. The corresponding optimized grid is shown in

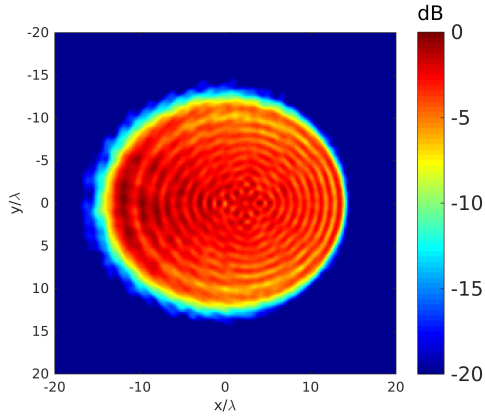

Figure 5.34. Amplitude in dB of the nominal Aperture Field.

Fig. 5.38. As a comparison, Fig. 5.39 shows a standard Cartesian sampling grid spaced according to the Nyquist sampling rate, and consisting of 441 samples.

5.2.3 Numerical Results

To show the accuracy and effectiveness of the diagnosis algorithm, some numerical tests are presented. To realistically simulate the field radiated by the AUT, the PO solver of FEKO has been used. Furthermore, the far field data has been corrupted by an additive Gaussian noise with a SNR of 35 dB. The diagnosis has been applied to the case of a lateral displacement of the feed. In particular, referring to Fig. 5.21, we indicate with Δx,Δy and Δz the displacements of the feed from the focus along the x-axis, y-axis and z-axis, respectively. The positions considered for the numerical tests are reported in Table 5.3.

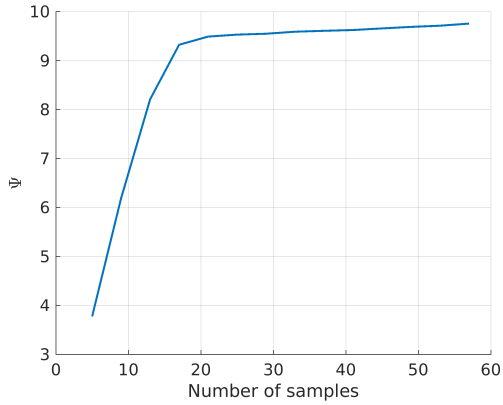

Figure 5.35. The optimal values of Ψ as a function on M.

	Δx [mm]	Δy [mm]	Δz [mm]
Case 1	7	0	0
Case 2	7	4	6

Table 5.3. Nominal positions for the feed displacement considered for the numerical tests.

Case 1

In this section, the results for Case 1 are shown. Fig. 5.40 and Fig. 5.41 show the amplitude of the co-polar component of the FFP simulated and reconstructed with the proposed approach, respectively. Fig. 5.42 and Fig. 5.43 display a superimposition of the simulated and reconstructed FFP on a cut along the u-axis and the v-axis, respectively, showing the effective representation of the FFP. Fig. 5.44 shows the simulated AUT phase distribution. Fig. 5.45 shows the phase of the recovered aberration

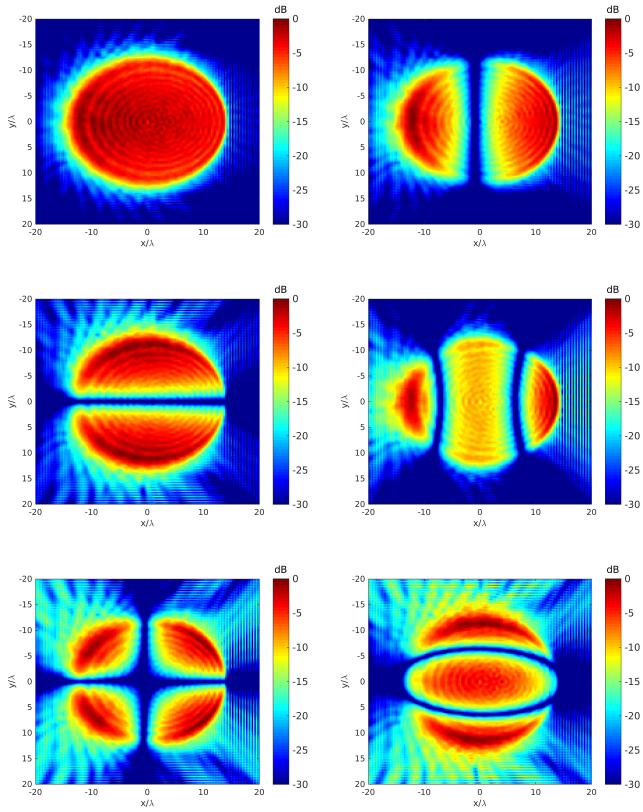

(e)

Figure 5.36. Amplitude in dB of the first six basis functions.

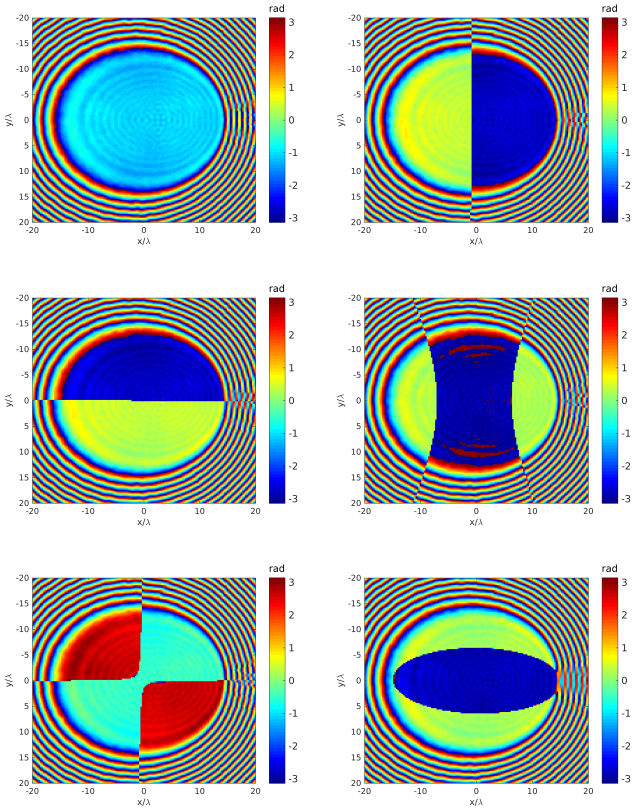

Figure 5.37. Phase of the first six basis functions.

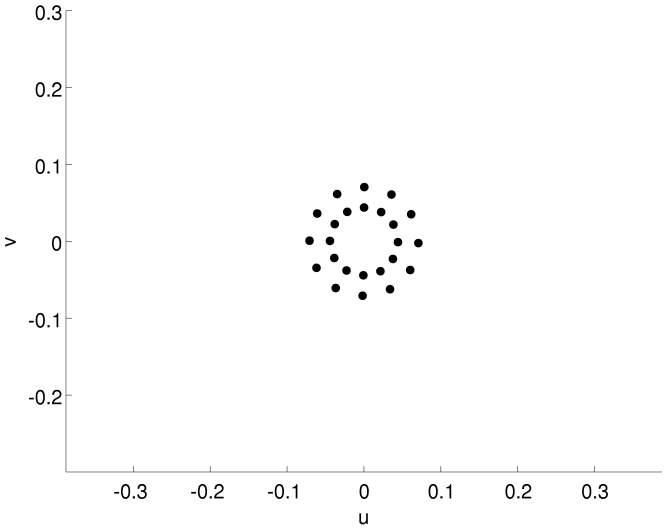

Figure 5.38. Location of the optimal sampling points.

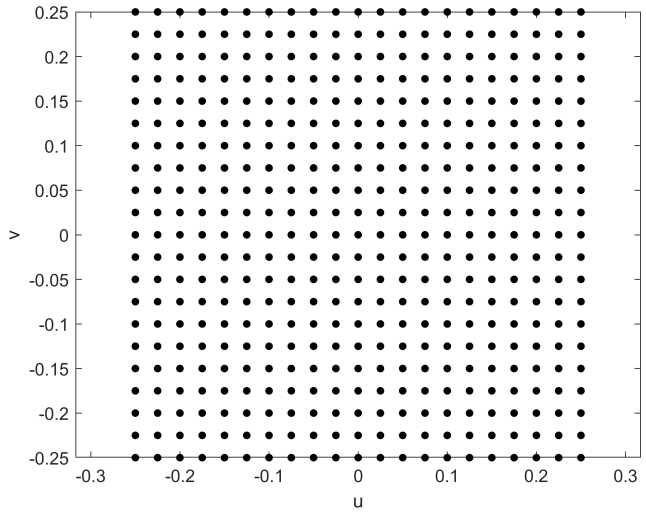

Figure 5.39. Location of the sampling point for a standard Cartesian grid.

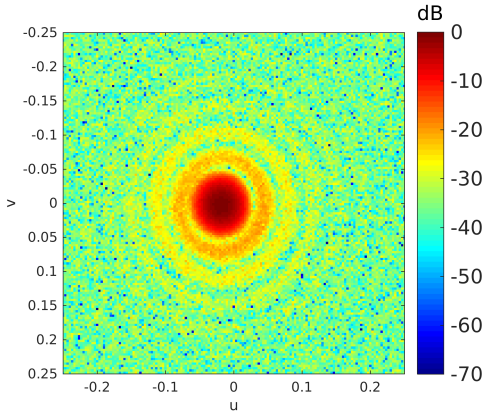

Figure 5.40. Normalized amplitude in dB of the simulated FFP for Case 1.

function. Fig. 5.46 and Fig. 5.47 display a superimposition of the simulated and reconstructed phase distribution on a cut along the x-axis and the y-axis, respectively. The displacement of the feed from the reflector focus corresponding to the retrieved aberration and its nominal position are presented in Table 5.4, showing an error of only 0.58 mm (0.02λ) in the diagnosis of the position.

	Δx [mm]	Δy [mm]	Δz [mm]
nominal	7	0	0
retrieved	6.91	-0.55	-0.16

Table 5.4. Retrieved position for Case 1.

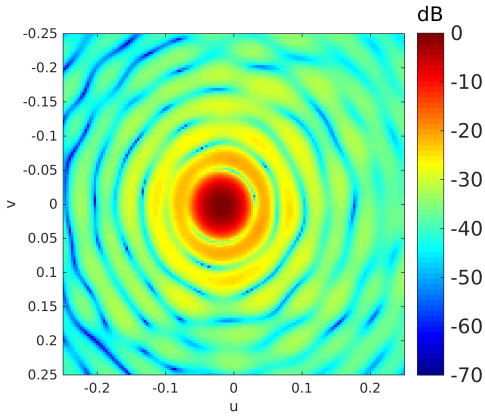

Figure 5.41. Normalized amplitude in dB of the reconstructed FFP for Case 1.

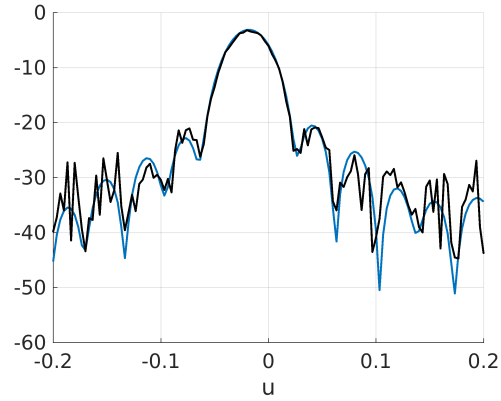

Figure 5.42. Cut along the u-axis of the normalized amplitude in dB of the simulated FFP (black line) and the FFP reconstructed with the proposed approach (blue line) for Case 1.

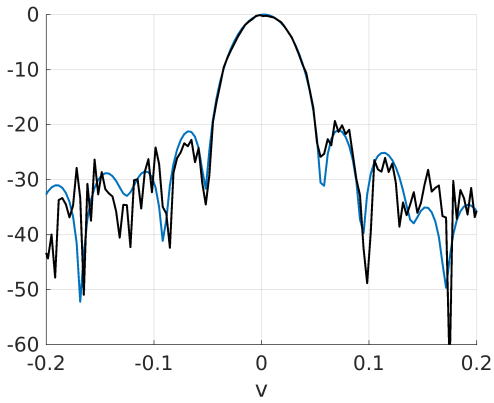

Figure 5.43. Cut along the v-axis of the normalized amplitude in dB of the simulated FFP (black line) and the FFP reconstructed with the proposed approach (blue line) for Case 1.

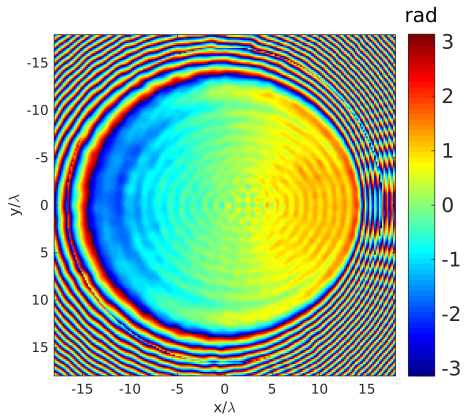

Figure 5.44. Phase of the aberration function simulated for Case 1.

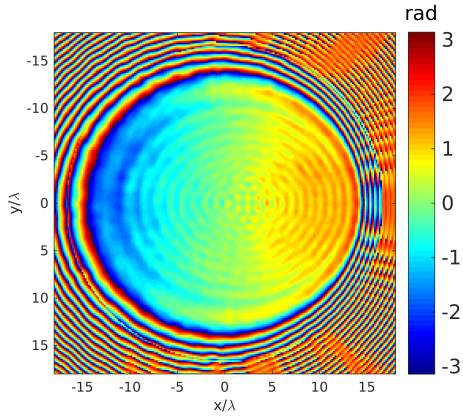

Figure 5.45. Phase of the aberration function reconstructed for Case 1.

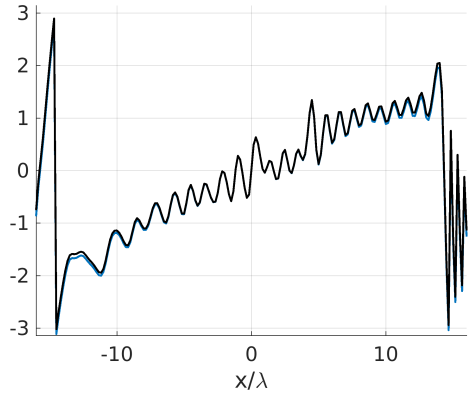

Figure 5.46. Cut along the x-axis of the simulated phase distribution (black line) and the reconstructed one (blue line) for Case 1.

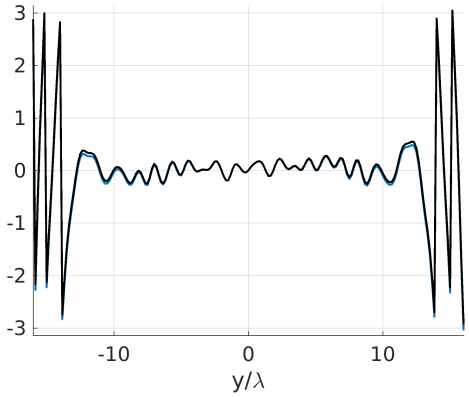

Figure 5.47. Cut along the y-axis of the simulated phase distribution (black line) and the reconstructed one (blue line) for Case 1.

Case 2

In this section, the results for Case 2 are shown. Fig. 5.48 and Fig. 5.49 show the amplitude of the co-polar component of the FFP simulated and reconstructed with the proposed approach, respectively. Fig. 5.50 and Fig. 5.51 display a superimposition of the simulated and reconstructed FFP on a cut along the u-axis and the v-axis, respectively, showing the effective representation of the FFP. Fig. 5.52 shows the simulated AUT phase distribution. Fig. 5.53 shows the phase of the recovered aberration function. Fig. 5.54 and Fig. 5.55 display a superimposition of the simulated and reconstructed phase distribution on a cut along the x-axis and the y-axis, respectively. The displacement of the feed from the reflector focus corresponding to the retrieved aberration and its nominal position are presented in Table 5.5, showing an error of only 0.2 mm ($6.5 \cdot 10^{-3}\lambda$) in

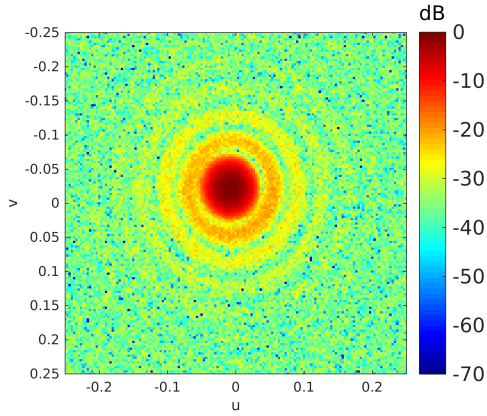

Figure 5.48. Normalized amplitude in dB of the simulated FFP for Case 2.

the diagnosis of the position.

	Δx [mm]	Δy [mm]	Δz [mm]
nominal	7	4	6
retrieved	6.96	3.99	5.81

Table 5.5. Retrieved position for Case 2.

5.2.4 Experimental Results

In this Section, the experimental results of the diagnosis method from data obtained in the far field test range described in Section 5.2.1 are presented. Again, referring to Fig. 5.21, Δx,Δy and Δz represents the displacements of the feed from the focus along the x-axis, y-axis and z-axis, respectively. In the following, three cases have been considered corresponding to different feed displacements, reported in Table 5.6.

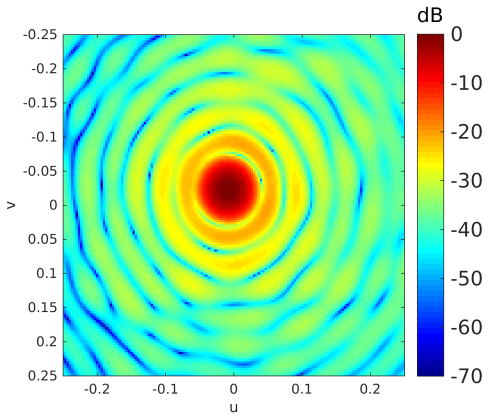

Figure 5.49. Normalized amplitude in dB of the reconstructed FFP for Case 2.

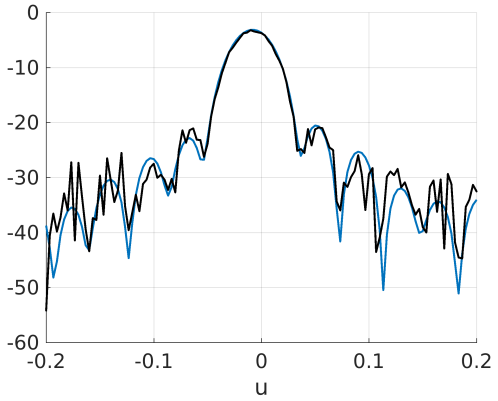

Figure 5.50. Cut along the u-axis of the normalized amplitude in dB of the simulated FFP (black line) and the FFP reconstructed with the proposed approach (blue line) for Case 2.

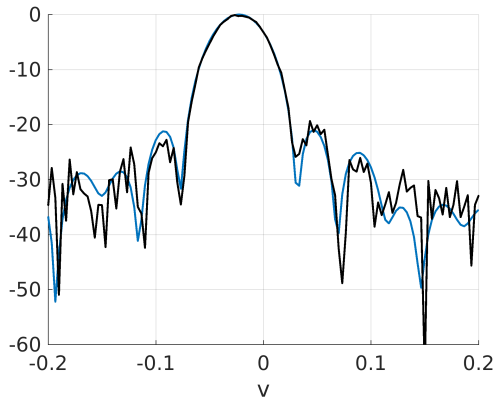

Figure 5.51. Cut along the v-axis of the normalized amplitude in dB of the simulated FFP (black line) and the FFP reconstructed with the proposed approach (blue line) for Case 2.

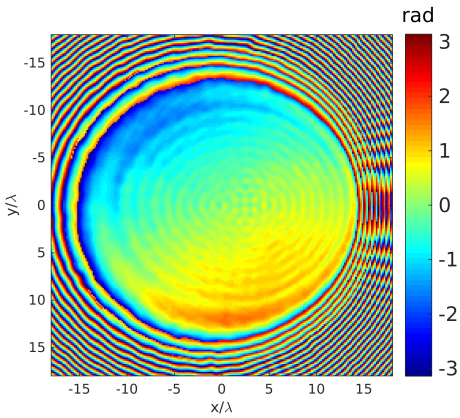

Figure 5.52. Phase of the aberration function simulated for Case 2.

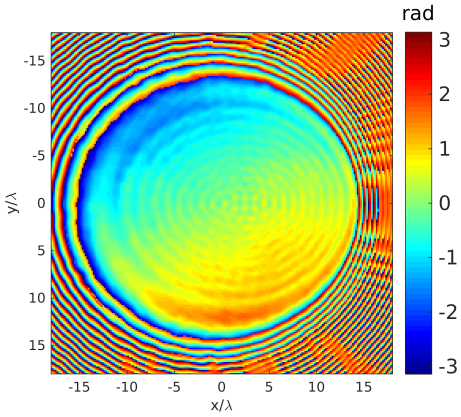

Figure 5.53. Phase of the aberration function reconstructed for Case 2.

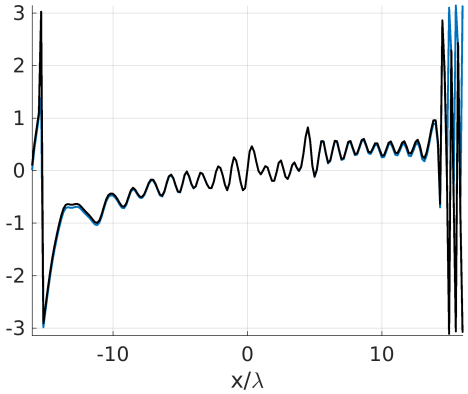

Figure 5.54. Cut along the x-axis of the simulated phase distribution (black line) and the reconstructed one (blue line) for Case 2.

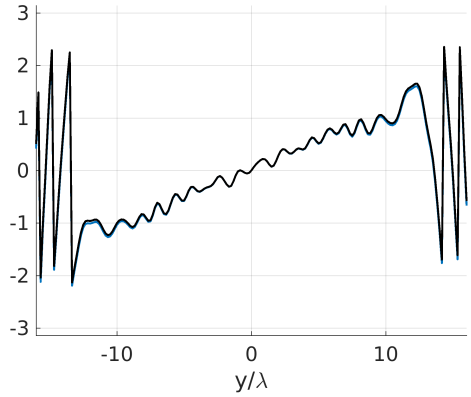

Figure 5.55. Cut along the y-axis of the simulated phase distribution (black line) and the reconstructed one (blue line) for Case 2.

	Δx [mm]	Δy [mm]	Δz [mm]
Case 1	0	0	8
Case 2	0	10	0
Case 3	5	0	0

Table 5.6. Nominal positions for the feed displacement considered for the experimental tests.

Case 1

In this section, the results for Case 1 are shown. Fig. 5.56 shows the phase of the aberration function obtained with the proposed approach on the optimized grid. To illustrate the accuracy of the inversion, the phase perturbation obtained on the standard Cartesian grid is shown as comparison in Fig. 5.57. The measured amplitude of the co-polar component of the

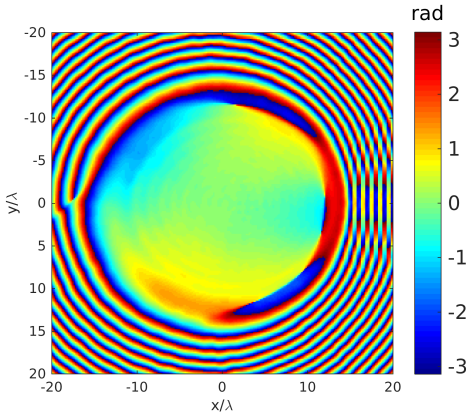

Figure 5.56. Phase of the aberration function retrieved on the optimized grid for Case 1.

FFP is shown in Fig. 5.58. Fig. 5.59 shows the FFP obtained with the proposed approach. Fig. 5.60 and Fig. 5.61 display a cut along the u-axis and v-axis, respectively, showing that the FFP can be effectively represented. The displacement of the feed from the reflector focus corresponding to the retrieved aberration and its nominal position are presented in Table 5.7, showing an error of only 1.9 mm (0.06λ) in the diagnosis of the position.

	Δx [mm]	Δy [mm]	Δz [mm]
nominal	0	0	8
retrieved	0.97	1.64	8.07

Table 5.7. Retrieved position for Case 1.

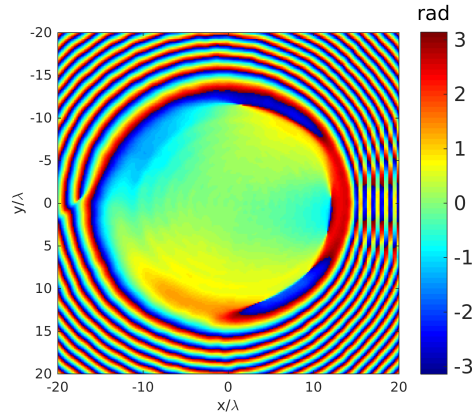

Figure 5.57. Phase of the aberration function retrieved on the standard grid for Case 1.

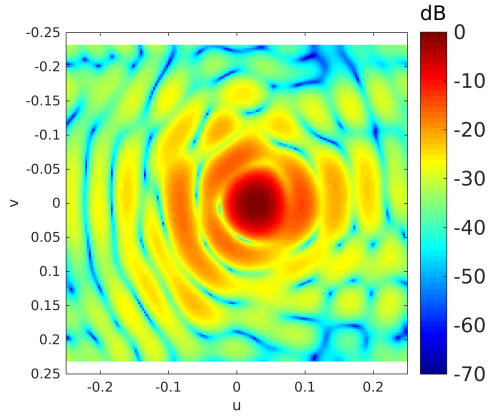

Figure 5.58. Normalized amplitude in dB of the measured FFP for Case 1.

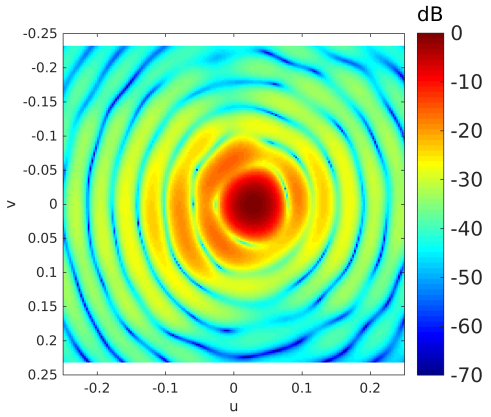

Figure 5.59. Normalized amplitude in dB of the reconstructed FFP for Case 1.

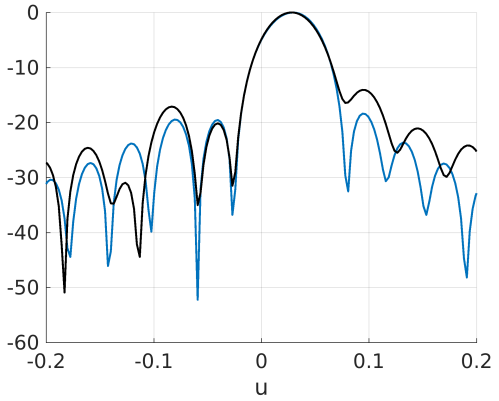

Figure 5.60. Cut along the u-axis of the normalized amplitude in dB of the measured FFP (black line) and the FFP reconstructed with the proposed approach (blue line) for Case 1.

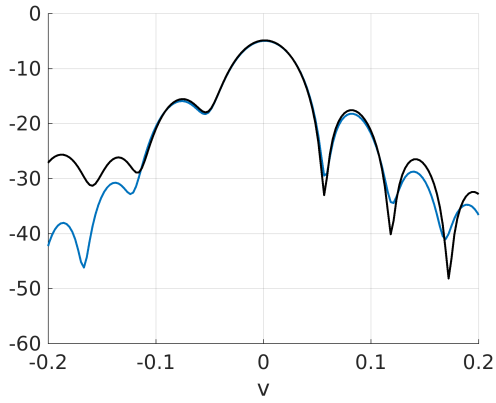

Figure 5.61. Cut along the v-axis of the normalized amplitude in dB of the measured FFP (black line) and the FFP reconstructed with the proposed approach (blue line) for Case 1.

Case 2

In this section, the results for Case 2 are shown. Fig. 5.62 shows the phase of the aberration function obtained with the proposed approach on the optimized grid. To illustrate the accuracy of the inversion, the phase perturbation obtained on the standard Cartesian grid is shown as comparison in Fig. 5.63. The measured amplitude of the co-polar component of the FFP is shown in Fig. 5.64. Fig. 5.65 shows the FFP obtained with the proposed approach. Fig. 5.66 and Fig. 5.67 display a cut along the u-axis and v-axis, respectively, showing that the FFP can be effectively represented. The displacement of the feed from the reflector focus corresponding to the retrieved aberration and its nominal position are presented in Table 5.8, showing an error of only 0.906 mm (0.03λ) in the diagnosis of the position.

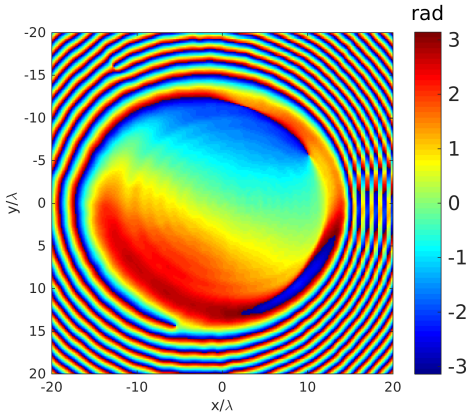

Figure 5.62. Phase of the aberration function retrieved on the optimized grid for Case 2.

	Δx [mm]	Δy [mm]	Δz [mm]
nominal	0	10	0
retrieved	0.41	10.11	0.8

Table 5.8. Retrieved position for Case 2.

Case 3

In this section, the results for Case 3 are shown. Fig. 5.68 shows the phase of the aberration function obtained with the proposed approach on the optimized grid. To illustrate the accuracy of the inversion, the phase perturbation obtained on the standard Cartesian grid is shown as comparison in Fig. 5.69. The measured amplitude of the co-polar component of the FFP is shown in Fig. 5.70. Fig. 5.71 shows the FFP obtained with the pro-

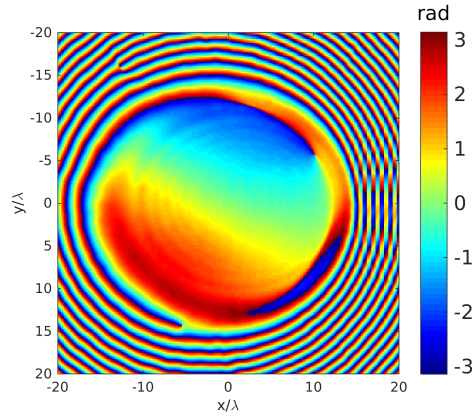

Figure 5.63. Phase of the aberration function retrieved on the standard grid for Case 2.

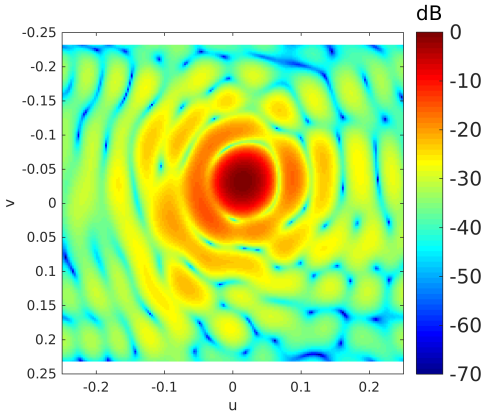

Figure 5.64. Normalized amplitude in dB of the measured FFP for Case 2.

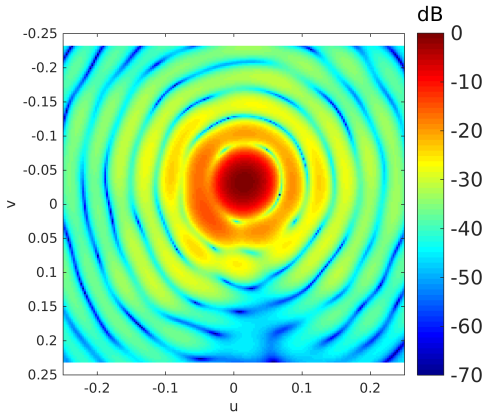

Figure 5.65. Normalized amplitude in dB of the reconstructed FFP for Case 2.

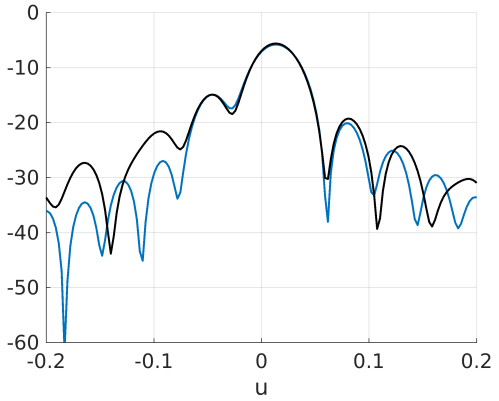

Figure 5.66. Cut along the u-axis of the normalized amplitude in dB of the measured FFP (black line) and the FFP reconstructed with the proposed approach (blue line) for Case 2.

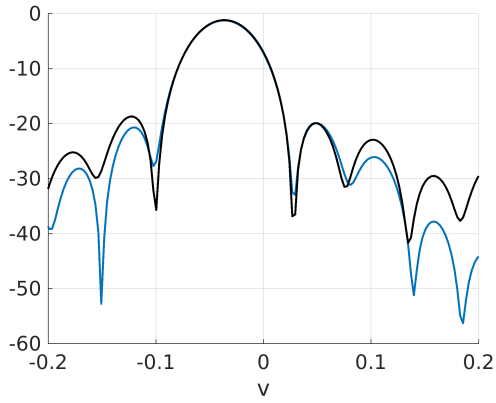

Figure 5.67. Cut along the v-axis of the normalized amplitude in dB of the measured FFP (black line) and the FFP reconstructed with the proposed approach (blue line) for Case 2.

posed approach. Fig. 5.72 and Fig. 5.73 display a cut along the u-axis and v-axis, respectively, showing that the FFP can be effectively represented. The displacement of the feed from the reflector focus corresponding to the retrieved aberration and its nominal position are presented in Table 5.9, showing an error of only 0.589 mm (0.02λ) in the diagnosis of the position.

	Δx [mm]	Δy [mm]	Δz [mm]
nominal	5	0	0
retrieved	5.32	0.12	0.48

Table 5.9. Retrieved position for Case 3.

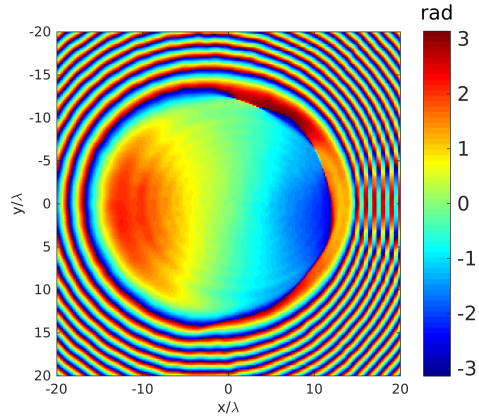

Figure 5.68. Phase of the aberration function retrieved on the optimized grid for Case 3.

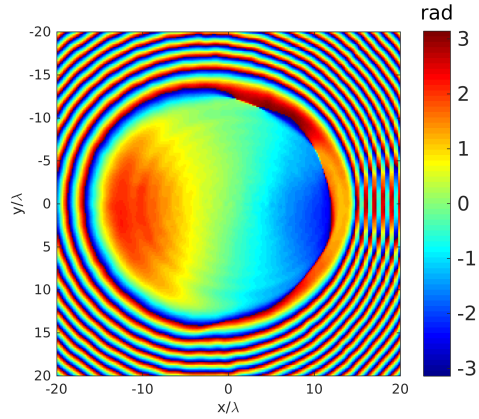

Figure 5.69. Phase of the aberration function retrieved on the standard grid for Case 3.

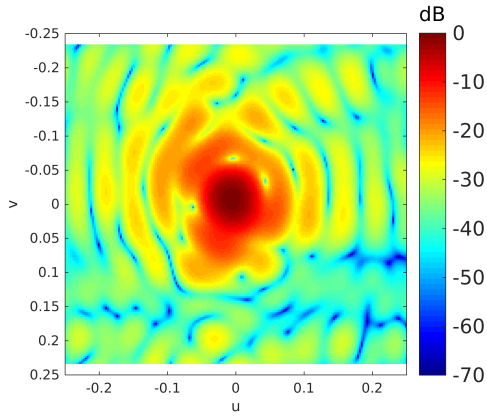

Figure 5.70. Normalized amplitude in dB of the measured FFP for Case 3.

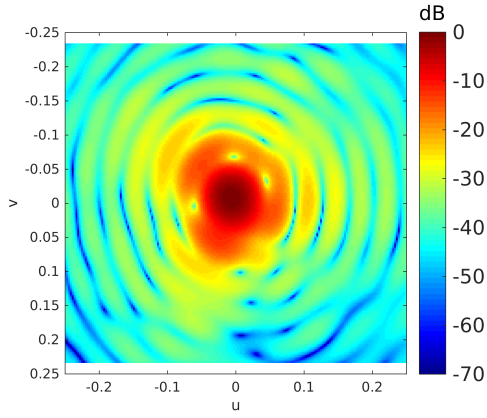

Figure 5.71. Normalized amplitude in dB of the reconstructed FFP for Case 3.

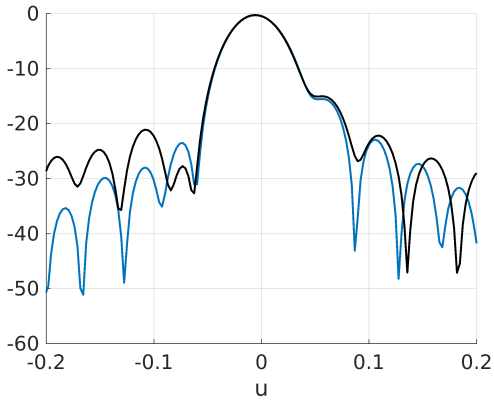

Figure 5.72. Cut along the u-axis of the normalized amplitude in dB of the measured FFP (black line) and the FFP reconstructed with the proposed approach (blue line) for Case 3.

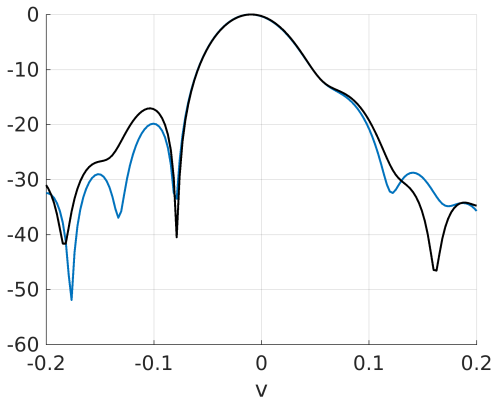

Figure 5.73. Cut along the v-axis of the normalized amplitude in dB of the measured FFP (black line) and the FFP reconstructed with the proposed approach (blue line) for Case 3.

Bibliography

[1] K. Jansky, "Electrical disturbances apparently of extraterrestrial origin", *Proceedings of the Institute of Radio Engineers*, vol. 21, no. 10, 1387–1398, 1933.

[2] R. E. Collin, *Antennas and radiowave propagation.* McGraw-Hill, 1985.

[3] J. D. Kraus, *Radio astronomy.* Cygnus-Quasar Books, 1986.

[4] G. C. Medellin, "Antenna noise temperature calculation", SKA Memo 95, Tech. Rep., 2007.

[5] W. Gordon, "Arecibo ionospheric observatory", *Science*, no. 146, 1964.

[6] P. Kildal, L. Baker, and T. Hagfors, "The arecibo upgrading: Dual-reflector feed system", *Proc. IEEE*, no. 82, 714–724, 1994.

[7] S. W. Ellingson, "Sensitivity of antenna arrays for long-wavelength radio astronomy", *IEEE Transactions on Antennas and Propagation*, vol. 59, no. 6, pp. 1855–1863, 2011.

[8] S. W. Ellingson, G. B. Taylor, J. Craig, J. Hartman, J. Dowell, C. N. Wolfe, *et al.*, "The lwa1 radio telescope", *IEEE Transactions on Antennas and Propagation*, no. 61, pp. 2540–2549, 2013.

[9] W. N Christiansen and J. A. Högbom, *Radiotelescopes*. CUP Archive, 1987.

[10] M. Born and E. Wolf, *Principles of optics*. Pergamon Press, 1970.

[11] P. Napier, A. R. Thompson, and R. D. Ekers, "The very large array: Design and performance of a modern synthesis radio telescope", *Proceedings of the IEEE*, 1983.

[12] M. P. van Haarlem, M. W. Wise, A. W. Gunst, G. Heald, J. P. McKean, J. W. T. Hessels, *et al.*, "Lofar: The low-frequency array", *Astron Astrophys*, no. 56:A2, 2013.

[13] P. Hall, "The square kilometre array: An international engineering perspective", in *The Square Kilometre Array: An Engineering Perspective*, Springer, 2005, pp. 5–16.

[14] J. Ruze, "The effect of aperture errors on the antenna radiation pattern", *Il Nuovo Cimento*, pp. 364–380, 1952.

[15] ——, "Antenna tolerance theory - a review", *Proc. IEEE.*, vol. 54, 633–640, 1966.

[16] L. Seidel, *Astr. Nachr.* 43, 289, 305, 321. 1856.

[17] J. Ruze, "Lateral-feed displacement", *IEEE Transactions on Antennas and Propagation*, vol. 13, no. 5, pp. 660–665, 1965.

[18] A. Greve, "Metrology of the effelsberg 100 meter radio reflector", *Zeitschrift Vermessungswes*, no. 106, pp. 308–315, 1981.

[19] P. F. Scott and M. Ryle, "A rapid method for measuring the figure of a radio telescope reflector", *Royal Astronon. SOC.Monthly notices*, vol. 178, pp. 539–545, 1977.

[20] A. Greve, "Reflector surface measurement of the iram 30-m radio telescope", *International journal of infrared and millimeter waves*, vol. 7, no. 1, pp. 121–135, 1986.

[21] A. Greve, D. Morris, L. E. B. Johansson, N. D. Whyborn, and A. Gluiber, "Precision of radio reflector surfaces adjusted from theodolite-tape measurements", *IEE Proceedings-Microwaves, Antennas and Propagation*, vol. 14, no. 1, pp. 23–29, 1994.

[22] J. G. Mangum, J. W. Baars, A. Greve, R. Lucas, R. C. Snel, P. Wallace, and M. Holdaway, "Evaluation of the alma prototype antennas", *Publications of the Astronomical Society of the Pacific*, vol. 118, no. 847, pp. 1257–1301, 2006.

[23] R. Subrahmanyan, "Photogrammetric measurement of the gravity deformation in a cassegrain antenna", *IEEE Transactions on Antennas and Propagation*, vol. 53, no. 8, 2005.

[24] Y. Rahmat-Samii and V. Galindo-Israel, "Shaped reflector antenna analysis using the jacobi-bessel series", *IEEE Transactions on Antennas and Propagation*, vol. 28, 1980.

[25] Y. Rahmat-Samii, "Surface diagnosis of large reflector antennas using microwave holographic metrology: An iterative approach", *Radio Science*, vol. 19, no. 5, pp. 1205–1217, 1984.

[26] J. Baars, B. Hooghoudt, P. Mezger, and M. de Jonge, "The iram 30-m millimeter radio telescope on pico veleta, spain", *Astron. Astrophys.*, no. 175, pp. 319–326, 1987.

[27] D. Morris, J. Baars, H. Hein, H. Steppe, C. Thum, and R. Wohleben, "Radio-holographic reflector measurement of the 30-m millimeter radio telescope at 22 ghz with a cosmic signal source", *Astron. Astrophys.*, no. 203, pp. 399–406, 1988.

[28] M. Godwin, E. Schoessow, and B. Grahl, "Improvement of the effelsberg 100 meter telescope based on holographic reflector surface measurement", *Astron. Astrophys.*, no. 167, pp. 390–394, 1986.

[29] J. Baars, R. Martin, J. Mangum, J. McMullin, and W. Peters, "The heinrich hertz telescope and the submillimeter telescope observatory", *Publ. Astron. Soc. Pacific*, no. 111, pp. 627–646, 1999.

[30] A. Capozzoli and G. D'Elia, "Global optimization and antennas synthesis and diagnosis, part one", *Progress In Electromagnetics Research, PIER 56*, pp. 195–232, 2006.

[31] ——, "Global optimization and antennas synthesis and diagnosis, part two", *Progress In Electromagnetics Research, PIER 56*, 233–261, 2006.

[32] B. Nikolic, R. M. Prestage, D. S. Balser, C. J. Chandler, and R. E. Hills, "Out-of-focus holography at the green bank telescope", *Astronomy and Astrophysics 465*, no. 2, pp. 685–693, 2007.

[33] G. Mazzarella, G. Montisci, and G. Serra, "A microwave holographic procedure for large symmetric reflector antennas using a fresnel-zone field data processing", *International Journal of Antennas and Propagation*, 2012.

[34] P. Bolli, G. Mazzarella, G. Montisci, and G. Serra, "An alternative solution for the reflector surface retrieval problem", *Progress In Electromagnetics Research, 82*, 2008.

[35] A. Ludwig, "The definition of cross-polarization", *IEEE Transactions on Antennas and Propagation*, vol. 21, pp. 116–119, 1973.

[36] Y. Rahmat-Samii, "Microwave holography of large reflector antennas - simulation algorithms", *IEEE Transactions on antennas and Propagation*, vol. 33, no. 11, pp. 1194–1203, 1985.

[37] A. Papoulis, "A new algorithm in spectral analysis and band-limited extrapolation", *IEEE Transactions on Circuits and systems*, vol. 22, no. 9, pp. 735–742, 1975.

[38] D. J. Rochblatt, “A microwave holography methodology for diagnostics and performance improvement for large reflector antennas”, 1992.

[39] D. J. Rochblatt and B. L. Seidel, “Microwave antenna holography”, *IEEE Transactions on Microwave Theory and Techniques*, vol. 40, no. 6, 1387–1398, 1992.

[40] O. M. Bucci, G. D’Elia, and G. Romito, “Reflector distortions diagnosis from far-field amplitude pattern”, *IEEE Transactions on Antennas and Propagation*, vol. 43, no. 11, pp. 1217–1225, 1995.

[41] A. Capozzoli, C. Curcio, G. D’Elia, A. Liseno, S. Savarese, and P. Schipani, “Optimized diagnosis of reflectors misalignements in radioastronomical applications”, in *9th European Conference on Antennas and Propagation (EuCAP)*, IEEE, 2015, pp. 1–5.

[42] D. Slepian and H. Pollak, “Prolate spheroidal wave functions, fourier analysis and uncertainty-i”, *Bell Labs Technical Journal*, vol. 40, no. 1, pp. 43–63, 1961.

[43] B. A. J Mercer, “Xvi. functions of positive and negative type, and their connection the theory of integral equations”, *Phil. Trans. R. Soc. Lond. A*, vol. 209, no. 441-458, pp. 415–446, 1909.

[44] F. Riesz and B. Sz, *Functional Analysis*. Ungar, New York, 1955.

[45] H. J. Landau and H. Pollak, "Prolate spheroidal wave functions, fourier analysis and uncertainty-ii", *Bell Labs Technical Journal*, vol. 40, no. 1, pp. 65–84, 1961.

[46] ——, "Prolate spheroidal wave functions, fourier analysis and uncertainty-iii: The dimension of the space of essentially time and band-limited signals", *Bell Labs Technical Journal*, vol. 41, no. 4, pp. 1295–133, 1962.

[47] D. Slepian, "Prolate spheroidal wave functions, fourier analysis and uncertainty-iv: Extensions to many dimensions; generalized prolate spheroidal functions", *Bell Labs Technical Journal*, vol. 43, no. 6, pp. 3009–3057, 1964.

[48] F. Gori and G. Guattari, "Shannon number and degrees of freedom of an image", *Optics Communications*, vol. 7, no. 2, pp. 163–165, 1973.

[49] A. N. Kolmogorov and S. V. Fomin, *Introductory real analysis*. Courier Corporation, 2012.

[50] I. T. Jolliffe, "Principal component analysis and factor analysis", in *Principal component analysis*, Springer, 1986, pp. 115–128.

[51] A. Capozzoli, A. Liseno, C. Curcio, S. Savarese, and P. Schipani, "Efficient diagnosis of radiotélescopes misalignments", in *AMTA 2016 Proceedings*, IEEE, 2016, pp. 1–5.

[52] A. Capozzoli, C. Curcio, and A. Liseno, "Nufft-accelerated plane-polar (also phaseless) near-field/far-field transformation", *Progress In Electromagnetics Research*, vol. 27, pp. 59–73, 2012.

[53] A. Capozzoli, C. Curcio, A. Liseno, S. Savarese, and P. Schipani, "Singular values behaviour optimization in the diagnosis of feed misalignments in radioastronomical reflectors", in *Advances in Optical and Mechanical Technologies for Telescopes and Instrumentation II*, International Society for Optics and Photonics, vol. 9912, 2016, 99124P.

[54] A. Capozzoli, C. Curcio, A. Liseno, and P. Vinetti, "Field sampling and field reconstruction: A new perspective", *Radio Science*, vol. 45, no. 6, 2010.

[55] P. C. Gao, Y. B. Tao, and H. L., "Parallel shooting and bouncing ray method on gpu clusters for analysis of electromagnetic scattering", *Progress In Electromagnetics Research*, vol. 137, pp. 87–99, 2013.

[56] T. Andersen and A. Enmark, *Integrated modeling of Telescopes*. Springer Science & Business Media, 2011, vol. 377.

[57] A. D. Wheelon, *Electromagnetic scintillation. vol. i: Geometrical optics*, 2001.

[58] R. Hinder, "Observations of atmospheric turbulence with a radio telescope at 5 ghz", *Nature*, vol. 225, no. 5233, p. 614, 1970.

[59] J.-D. Benamou, "An eulerian numerical method for geometric optics", in *ESAIM: Proceedings*, EDP Sciences, vol. 11, 2002, pp. 13–40.

[60] A. Capozzoli, C. Curcio, A. Liseno, and S. Savarese, "Two-dimensional fast marching for geometrical optics", *Optics Express*, vol. 22, no. 22, pp. 26 680–26 695, 2014.

[61] J. A. Sethian, "Fast marching methods", *SIAM review*, vol. 41, no. 2, pp. 199–235, 1999.

[62] E. Rouy and A. Tourin, "A viscosity solutions approach to shape-from-shading", *SIAM Journal on Numerical Analysis*, vol. 29, no. 3, pp. 867–884, 1992.

[63] D. Stalling and H. Hege, "Fast and resolution independent line integral convolution", in *Proceedings of the 22nd annual conference on Computer graphics and interactive techniques*, ACM, 1995, pp. 249–256.

[64] I. Wald and V. Havran, "On building fast kd-trees for ray tracing, and on doing that in o (n log n)", in *Interactive Ray Tracing 2006, IEEE Symposium on*, IEEE, 2006, pp. 61–69.

[65] T. Aila and S. Laine, "Understanding the efficiency of ray traversal on gpus", in *Proceedings of the conference on high performance graphics 2009*, ACM, 2009, pp. 145–149.

[66] M. Stich, H. Friedrich, and A. Dietrich, "Spatial splits in bounding volume hierarchies", in *Proceedings of the Conference on High Performance Graphics 2009*, ACM, 2009, pp. 7–13.

[67] L. C. Evans, "Partial differential equations (providence, ri: American mathematical society)", 1998.

[68] M. G. Crandall and P.-. L., "Viscosity solutions of hamilton-jacobi equations", *Transactions of the American Mathematical Society*, vol. 277, no. 1, pp. 1–42, 1983.

[69] R. Sedgewick, *Algorithms*. Pearson Education India, 1988.

[70] D. L. Chopp, "Some improvements of the fast marching method", *SIAM Journal on Scientific Computing*, vol. 23, no. 1, pp. 230–244, 2001.

[71] R. Kimmel and J. A. Sethian, "Fast marching methods on triangulated domains", in *Proceedings of the National Academy of Science*, vol. 95, 1998, pp. 8341–8435.

[72] H. Zhao, "A fast sweeping method for eikonal equations", *Mathematics of computation*, vol. 74, no. 250, pp. 603–627, 2005.

[73] A. Capozzoli, C. Curcio, A. Liseno, and S. Savarese, "A comparison of fast marching, fast sweeping and fast iterative methods for the solution of the eikonal equation", in *Telecommunications Forum (TELFOR), 2013 21st*, IEEE, 2013, pp. 685–688.

[74] J. Sanders and E. Kandrot, *CUDA by example: an introduction to general-purpose GPU programming*. Addison-Wesley Professional, 2010.

[75] J. Nickolls, I. Buck, M. Garland, and K. Skadron, "Scalable parallel programming with cuda", in *ACM SIGGRAPH 2008 classes*, ACM, 2008, p. 16.

[76] A. Capozzoli, C. Curcio, A. Liseno, and S. Savarese, "Accelerating fast marching for geometrical optics", in *International Applied Computational Electromagnetics Society Symposium-Italy (ACES)*, IEEE, 2017, pp. 1–2.

[77] J. Laska, *Writing c functions in matlab (mex-files)*, 2004.

[78] H. Mosallaei and Y. Rahmat-Samii, "Nonuniform luneburg and two-shell lens antennas: Radiation characteristics and design optimization", *IEEE Transactions on Antennas and Propagation*, vol. 49, no. 1, pp. 60–69, 2001.

[79] A. Capozzoli, C. Curcio, A. Liseno, and S. Savarese, "Go solutions with fast marching", in *10th European Conference on Antennas and Propagation (EuCAP)*, IEEE, 2016, pp. 1–5.

[80] *Series 37xxxc vector network analyzer operation manual*, Anritsu, 490 Jarvis Drive, Morgan Hill, CA 95037-2809, 2004.